Univ.Prof. Dr.rer.nat. Ulrich Schubert   Univ.Prof. Dr.rer.nat. Herwig Peterlik

TECHNISCHE UNIVERSITÄT WIEN

DISSERTATION

Ligand exchange reactions of transition metal oxo clusters and their application for the synthesis of inorganic-organic hybrid materials

Ausgeführt zum Zwecke der Erlangung des akademischen Grades eines Doktors der technischen Wissenschaften unter der Leitung von

O.Univ.Prof. Dr.rer.nat. Ulrich Schubert
E165
Institut für Materialchemie

Eingereicht an der Technischen Universität Wien
Fakultät für Technische Chemie

von

Johannes Kreutzer
0230447
Payergasse 3/1/18
1160 Wien

Wien am 3.6.2015

Eidesstattliche Erklärung

I hereby certify that I am the sole author of this thesis and that my thesis does not infringe upon anyone's copyright nor violate any proprietary rights and that any ideas, techniques, quotations, or any other material from the work of other people included in my thesis, published or otherwise, are fully acknowledged in accordance with the standard referencing practices.

Hiermit erkläre ich an Eides statt, dass ich die vorliegende Arbeit selbstständig und ohne fremde Hilfe verfasst, andere als die angegebenen Quellen und Hilfsmittel nicht benutzt und die aus anderen Quellen entnommenen Stellen als solche gekennzeichnet habe.

Wien, am 23. Juni 2015

Acknowledgment

Abstract

Ligand exchange reactions of transition metal oxo clusters and the impact of modification of the ligand sphere of the clusters on properties of the hybrid materials was investigated.

Ligand binding energies of different ligands were calculated by means of DFT calculations. Different basis sets and functionals were evaluated with respect to a sufficiently accurate description of the geometry and the vibrational modes of the cluster $Zr_4O_2(OMc)_{12}$ (OMc = methacrylate). Ligand binding energies of the methacrylate ligands with respect to different positions on the cluster and to electronic effects of different substituents on the ligands were also investigated.
The methacrylate ligands of $Zr_4O_2(OMc)_{12}$ were completely exchanged with pivalic acid to verify that exchange reactions with carboxylic acids on $Zr_4O_2(OMc)_{12}$ proceed under retention of the cluster core. Ligand exchange with different sterically demanding ligands was probed and the steric influence on the equilibrium reaction investigated. Scrambling reactions between clusters with the same cluster core but different ligands were investigated by two-dimensional NMR spectroscopy and are a second preparative route to mixed-ligand clusters. The question of site-selective ligand exchange was investigated by exchange of chelating carboxylate ligands with acetylacetonate. However, the stability of the cluster core seems to be of uttermost importance in this reaction. Besides successful site-selective ligand exchange, rearrangement of clusters and degradation was also observed.

The impact of ligand exchange reactions on properties of hybrid materials was investigated. Thereby different amounts of the methacrylate ligands of $Zr_4O_2(OMc)_{12}$ was exchanged with pivalate ligands. Polymerization led to hybrid materials with different crosslinking densities. Mechanical and thermal properties of these hybrid materials were investigated. Furthermore, bifunctional clusters were synthesized by ligand exchange reactions and incorporated in a polymer network by STED lithography. After the lithographic process, it was shown that the second functionality remains active for chemical reactions.

Zusammenfassung

Diese Arbeit beschäftigt sich mit Ligandenaustauschreaktionan an Übergangsmetall Oxo Clustern und der Möglichkeit mittels Ligandenaustausch die Eigenschaften von Hybridmaterialien zu verändern.

Mittels DFT Rechnungen wurden Ligandenbindungsenergien berechnet und miteinander verglichen. Im ersten Schritt wurden dabei verschiedene Funktionale und Basissätze hinsichtlich ihrer Genauigkeit in dieser Problemstellung evaluiert. Im Anschluss daran wurden Ligandenbindungsenergien bezüglich der Position der Liganden im Cluster und bezüglich elektronischer Effekte untersucht.

Im präparativen Teil wurden drei verschiedene Arten an Ligandenaustasuchreaktionen untersucht. Es wurde gezeigt, dass der vollständige Austausch der Methacrylat-Liganden von $Zr_4O_2(OMc)_{12}$ gegen Pivalat Liganden unter Beibehaltung des Clusterkernes möglich ist. In weiterer Folge wurden sterische Effekte der eintretenden Liganden auf die Gleichgewichtsreaktion untersucht. Scrambling-Reaktionen zwischen Clustern mit dem gleichen Kern aber mit unterschiedlichen Liganden wurden durchgeführt und es wurde mittels NMR Spektroskopie gezeigt, dass sie unter Erhalt der ursprünglichen Clusterstruktur ablaufen. Ortsspezifischer Ligandenaustausch konnte in Austauschreaktionen mit Acetylaceton gezeigt werden. Hierbei kommt es aber vor allem auf die Stabilität der Cluster an, da auch in manchen Fällen Umordnungen und Zersetzung der Cluster beobachtet wurde. Die Auswirkung von Ligandenaustsuch-Reaktionen auf die Eigenschaften von Hybridmaterialien wurde untersucht. Dabei wurden die Methacrylat-Liganden des Clusters $Zr_4O_2(OMc)_{12}$ stufenweise gegen Pivalat-Liganden ausgetauscht. Durch Polymerisation konnten Hybridmaterialien mit verschiedenen Quervernetzungsdichten hergestellt werden. Die thermischen und mechanischen Eigenschaften der Proben wurden untersucht und verglichen. Weiters wurden durch Ligandenaustauschreaktionen bifunktionelle Cluster hergestellt. Es konnte gezeigt werden, daß die zweite Funktionalität nach der Polymerisation für weitere chemische Reaktionen erhalten bleibt.

Abbreviations

δ	Chemical shift
η	Hard sphere volume fraction
μ	Absorption coefficient
Ac	Acetate
acac	Acetylacetonate
acac-H	Acetylacetone
AFM	Atomic force microscopy
AOM	Acusto optic modulator
APD	Avalanche photo diode
ATR-IR	Attenuated total reflection infrared spectroscopy
BPA	Ethoxylated bisphenol A diacrylate
BSSE	Basis set superposition error
CC	Coupled cluster
CI	Configuration interaction
CP	Counterpoise
cw	Continuous wave
DBC	Double bond conversion
DETC	7-Diethylamino-3-thenoylcoumarin
DFT	Density functional theory
DLW	Direct laser writing
DMTA	Dynamic mechanical thermoanalysis
DSC	Differential scanning calorimetry
DUV	Deep ultraviolet
D_x	Calculated density
E'	Storage modulus
E"	Loss modulus

EB	Electron beam
ECP	Effective core potential
ESI-MS	Electron spray mass spectroscopy
EUV	Extreme ultraviolet
EXSY	Exchange spectroscopy
FIR	Far infrared
FT-IR	Fourier transform infrared spectroscopy
GGA	Generalized gradient approximation
GTO	Gaussian type orbitals
HDPE	High density polyethylene
HEMA	2-Hydroxyethyl methacrylate
HF	Hartree Fock
HMBC	Heteronuclear multiple bond correlation
HOAc	Acetic acid
HOFormate	Formic acid
HOIsob	Isobutyric acid
HOPiv	Pivalic acid
HOProp	Propionic acid
HOPrSH	3-Mercaptopropionic acid
iPP	Isotactic polypropylene
LDA	Local density approximation
LSM	Laser scanning microscopy
M_Γ	Molecular mass
MAE	Mean average error
MAS	Magic angle spinning
McOH	Methacrylic acid
MIR	Mid infrared
MOF	Metal organic framework
NBB	Nanosized building block
NIR	Near infrared
NMR	Nuclear magnetic resonance spectroscopy
NOE	Nuclear overhauser enhancement
NOESY	Nuclear overhauser enhancement spectroscopy
OAc	Acetate

OAcr	Acrylate
OBu	Butoxide
OEt	Ethoxide
OFormate	Formate
OIsob	Isobutyrate
O^{i}Bu	Isobutoxide
O^{i}Pr	Isopropoxide
OMc	Methacrylate
OMe	Methoxide
ONep	Neopentoxide
OPiv	Pivalate
OPr	Propoxide
OProp	Propionate
OPrSH	3-Mercaptopropionate
O^{t}Bu	*tert*-Butoxide
p	Porod scaling exponent
PCL	Poly(ϵ-caprolactone)
PETA	Pentaerythritol triacrylate
PFS	Point spread function
PH	Pinhole
pHEMA	Poly(3-hydroxyethyl methacrylate)
PI	Polyimide
PMMA	Poly(methylmethacrylate)
POM	Polyoxometalate
POSS	Polyhedral oligomeric silsesquioxane
PP	2π Spiral phase
PPS	Poly(phenylenesulfide)
PTT	Poly(trimethylene terephthalate)
q	Scattering vector
R$_{g}$	Radius of gyration
R$_{HS}$	Hard sphere radius
RMS	Root means square error
ROMP	Ring opening metathesis polymerization
R$_{w}$	Alkoxo group-to-water ratio

SAM	Self-assembled monolayer
SAXS	Small angle X-ray scattering
SEM	Scanning electron microscopy
STED	Stimulated emission depletion
T_d	Thermal degradation temperature
Tan δ	Phase lag
TEM	Transmission electron microscopy
TEOS	Tetraethylorthosilicate
T_g	Glass transition temperature
TGA	Thermogravimetric analysis
Ti4Zr4	$Ti_4Zr_4O_6(OBu)_4(OMc)_{16}$
Ti2Zr4	$Ti_2Zr_4O_4(OMc)_{16}$
Ti2Zr4_2	$Ti_2Zr_4O_4(OBu)_2(OMc)_{16}$
T_{pol}	Onset of polymerization
UEG	Uniform electron gas
VAC	Vinylacetate
WFT	Wave function theory
XPS	X-ray photoelectron spectroscopy
XRD	X-ray diffractometry
Z	Formula units
ZPE	Zero point energy
Zr12Pr	$[Zr_6O_4(OH)_4(OProp)_{12}]_2$
Zr12Pr_acac	$[Zr_6O_4(OH)_4(OProp)_{11}(acac)]_2$
Zr12VAC	$[Zr_6O_4(OH)_4(VAC)_{12}]_2$
Zr12VAC_acac	$[Zr_6O_4(OH)_4(VAC)_{11}(acac)]_2$
Zr4	Symmetric form of $Zr_4O_2(OMc)_{12}$
Zr4_as	Asymmetric form of $Zr_4O_2(OMc)_{12}$
Zr4_SH1	$Zr_4O_2(OMc)_{10}(OPrSH)_2$
Zr4_SH2	$Zr_4O_2(OMc)_9(OPrSH)_3$
ZrPiv	$Zr_4O_2(OPiv)_{12}$

Contents

Chapter 1

Introduction

Introduction

Advancements in the synthesis and characterization of hybrid materials promoted the development of new materials with highly specialized and tailored properties during the past decades. Hybrid materials are commonly seen as composite materials where both typically inorganic and organic moieties are mixed intimately on a molecular level. The controlled combination of organic and inorganic phases on a micro scale allows to tailor and improve materials properties in the resulting hybrid material. These improvements (e.g. mechanical strength or increased thermal stability) are often caused by synergistic effects between the inorganic and organic components.

Although the concept of hybrid materials is a very old one and can be found often in nature (e.g. tooth and bone tissue, mollusc shell) a controlled synthesis of hybrid materials depends on synthetic approaches which are characterized by mild reaction conditions and by keeping the integrity of the precursors intact. One mild chemistry approach, called "sol - gel" chemistry, is based on hydrolysis and condensation reactions of metal alkoxides and was found to be a versatile method to produce different types of metal oxides under low temperature conditions. The foundation of sol - gel chemistry goes back to the mid - 1880s where Ebelman and Graham studied the hydrolysis of tetraethyl orthosilicate (TEOS) under acidic conditions. [1] In the mid - 1900s the term *chimie douce* was used to describe a different mild chemistry synthesis route to metastable metal oxides which is characterized by low temperature solid - solid transformations, predominantly intercalation, hydrolysis and ion exchange reactions. [2] [3][4] Jacques Livage finally applied the term *chemie douce* to a sol - gel based approach towards hybrid materials with the aim to obtain - in a broader sense - inorganic - organic hybrid materials under retention of the geometry of the precursors. [5]
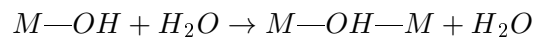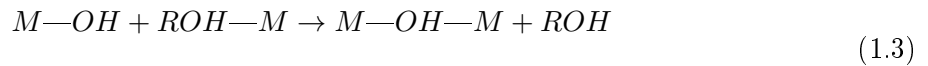
1.1 Sol‑Gel Chemistry

Sol‑gel chemistry is a bottom‑up approach to obtain amorphous‑"glass-like"‑metal oxide materials. [6] Precursors for sol‑gel processing are commonly inorganic salts or metal and semimetal alkoxides, which are typically hydrolysed in solution. In a first step smaller metal oxo particles are formed which give a colloidal suspension (sol). Further condensation reactions allow these particles to interconnect and to form a three‑dimensional network which surrounds the solvent (gel). Hydrolysis and condensation proceed simultaneously but can be divided in three important reaction steps (see equation 1.1‑1.3)

Hydrolysis

$$M\text{—}OR + H_2O \rightarrow M\text{—}OH + ROH \tag{1.1}$$

Condensation

$$M\text{—}OH + M\text{—}OR \rightarrow M\text{—}O\text{—}M + ROH$$
$$M\text{—}OH + M\text{—}OH \rightarrow M\text{—}O\text{—}M + H_2O \tag{1.2}$$

$$M\text{—}OH + ROH\text{—}M \rightarrow M\text{—}OH\text{—}M + ROH$$
$$M\text{—}OH + H_2O \rightarrow M\text{—}OH\text{—}M + H_2O \tag{1.3}$$
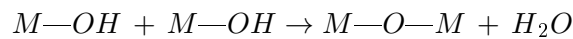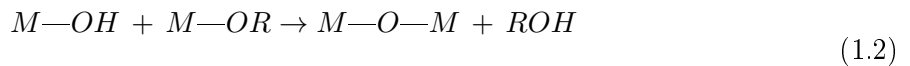
Akoxo groups of the metal alkoxides are cleaved from the metal upon hydrolysis and hydroxy groups are formed (eq. 1.1). Further condensation of these M-OH species under cleavage of alcohol (eq. 1.2) or water (eq. 1.3) results in the formation of metal‑oxygen‑metal bonds. In a first step, only few metal atoms are connected through oxo bridges with each other and form the sol particles. Unreacted alkoxo groups of the metal oxo particles in the sol can undergo further hydrolysis and condensation reactions and form the network of the gel. The solvent thereby remains in the system and is surrounded by the metal oxo network. Hydrolysis and condensation are competing reactions in the sol‑gel process but can be controlled by the alkoxo group to water ratio R_w.

The sol‑gel process is a kinetically controlled process, thus all reaction parameters influence the reaction and its outcome. Therefore the challenge of the sol‑gel process lies in the exact control of the reaction parameters to obtain reproducible results.

Sol-gel reactions are influenced by the kind of precursors used, the kind of alkoxo groups bonded to the metal, the alkoxo group to water ratio R_w, the kind of solvent, the temperature, pH and the concentration of the components in the reaction mixture. The influence of all these reaction parameters is discussed exhaustively in ref [7] and only a short discussion of the most important parameters for this work will be given below.

Kind of precursor

The reactivity of metal alkoxides towards nucleophilic attack depends mainly on the electronegativity of the metal atom and its ability to increase its coordination number. Alkoxysilanes ($Si(OR)_4$) for example have a much less polarized Si-O bond compared to transition metal alkoxides. This decreases the reactivity of alkoxysilanes in the sol-gel process towards hydrolysis and catalysts such as acids or bases are usually used. [8] Transition metal alkoxides on the other hand show a high reactivity towards nucleophilic attack and react readily with ambient moisture. Upon sol-gel processing, chemical additives in form of chelating ligands are often used as moderator to decrease the reactivity of transition metal-based precursors.

Ability to expand the coordination number

The silicon atoms in silicon alkoxides have a coordination number of four. Transition metals on the other hand show coordination numbers which exceed their charge. The Zr atom in $Zr(OR)_4$ for example, often shows coordination numbers of 6 or 7 but has only a charge of +IV. This results in formation of oligomers of the metal alkoxide and influences the hydrolysis and condensation reactions in the sol-gel process. $Ti(OEt)_4$ has a tetrameric structure in the crystalline state where the Ti atom expands its coordination sphere through bridging alkoxo ligands. [9] This changes when $Ti(OEt)_4$ is dissolved. In benzene solution for example, $Ti(OEt)_4$ has a trimeric structure as was evidenced by cryoscopy. [10] In contrast, $Ti(O^iPr)_4$ with sterically more demanding ligands, exists in monomeric form in benzene. [10] $Ti(O^tBu)_4$, bearing sterically even more demanding ligands, shows a coordination number of four and exists exclusively in monomeric form. [11] Thus sterically demanding alkoxo groups decrease the degree of oligomerization of the metal alkoxide and influence the reactivity during the sol-gel process. Furthermore the tendency to form oligomers also increases with the size of the metal. Zr and Hf alkoxides show in general higher average degrees of oligomerization than the corresponding Ti alkoxides. Metal alkoxides with unsaturated coordination sites are more prone to nucleophilic attack than species which

show a fully saturated coordination sphere. Hydrolysis reactions therefore occur much faster for monomeric species than for oligomeric metal alkoxides.

Solvent influence

The degree of oligomerization and the reaction rate of the hydrolysis can also be influenced by the solvent. Apolar solvents such as cyclohexane favor the formation of oligomers and concomitantly a slow hydrolysis rate. In protic solvents (e.g. an metal alkoxide in its parent alcohol) or coordinating solvents (e.g. THF, pyridine) the metal atom can expand its coordination number through coordination of the solvent molecules. The degree of oligomerization is therefore decreased and the hydrolysis rate increases.
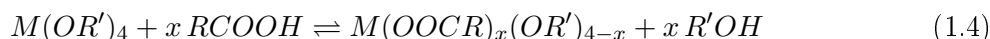
Modifiers

Transition metal alkoxides undergo fast hydrolysis and condensation reactions due to the highly polarized metal-oxygen bond. Nevertheless, hydrolysis and condensation reactions can be slowed down by adding modifiers. Commonly mono- or bidentate ligands which strongly bind to the metal and replace one or more of the alkoxo groups are used as modifying agents. This has several effects on the metal alkoxide structure and the reaction rate: The stronger bonding of the modifying group lowers the reactivity of the remaining metal alkoxide groups. Taking the case that mono-anionic bidentate ligands (e.g. acetylacetonates (acac) or carboxylates) are used, alkoxo groups will be replaced by the new ligand under retention of the charge balance. At the same time one additional coordination site of the metal will be occupied. This slows down the reactivity of the metal alkoxide. Acetylacetone (acac-H) is a widely used modifier and acac ligands replace readily up to two alkoxo groups of $Ti(OR)_4$. Further exchange of alkoxo groups with acac was not observed. Reaction of $Zr(OR)_4$ with 4 eq. of acac-H on the other hand leads to the formation of $Zr(acac)_4$ where all alkoxo ligands are replaced by the bidentate acac ligands. This is explained by the possibility of Zr(IV) to expand its coordination number to 8, which is not likely for Ti. The stoichiometry of the acac ligand shows an influence on the degree of condensation of the hydrolysis products. Slow hydrolysis of $Ti(OR)_2(acac)_2$ results in the formation of dimeric $[TiO(acac)_2]_2$. [12] The oxo cluster $Ti_4O_2(O^iPr)_{10}(acac)_2$ was obtained after hydrolysis of a $2:1$ mixture of $Ti(O^iPr)_4$ and acac-H [13] while hydrolysis of a $10:1$ mixture of $Ti(OBu)_4$ and acac-H resulted in the formation of $Ti_{18}O_{22}(OBu)_{26}(acac)_2$. [13] Similar results were obtained for hydrolysis reactions of modified Zr alkoxides. [14] [15] [16] Stoichiometric

hydrolysis of metal alkoxides often leads to the formation of crystalline hydrolysis‑condensation products whose structure can be determined by single crystal X‑ray diffractometry.

1.2 Carboxylate-Substituted Oxo Clusters

Modifying transition metal alkoxides with acac-H and subsequent hydrolysis of the modified alkoxide leads to acac-substituted transition metal oxo species as discussed above. Water which is added during the hydrolysis process serves as source for the oxo groups. In case carboxylic acids are used in excess as modifying agents, oxo clusters of the form $M_aO_b(OOCR)_x(OR')_y$ are formed without an additional water source. Two mechanisms for the hydrolysis and condensation reactions of transition metal alkoxides and carboxylic acids are reported in literature. The first mechanism proposes an esterification step (eq. 1.5) which produces *in situ* water. The thus generated water is consumed in the condensation reaction which leads to the metal oxo cluster (eq. 1.6). [17] [18] [19] [20] For example, reaction of $Ti(OBu)_4$ with a two-fold excess of acetic acid yields the cluster $Ti_6O_4(OAc)_8(OBu)_8$. [17].

Substitution

$$M(OR')_4 + x\,RCOOH \rightleftharpoons M(OOCR)_x(OR')_{4-x} + x\,R'OH \tag{1.4}$$

Esterification

$$RCOOH + R'OH \rightarrow RCOOR' + H_2O \tag{1.5}$$

Hydrolysis and condensation

$$M(OOCR)_x(OR')_{4-x} + H_2O \rightarrow M_aO_b(OOCR)_x(OR')_y + R'OH \tag{1.6}$$
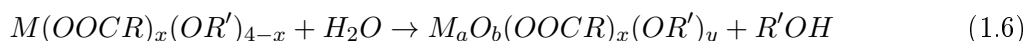
The formation of oxo clusters through *in situ* formation of water is favored when the acid is applied in excess. Nevertheless oxo clusters are formed in cases where the metal alkoxide to acid ratio is 1:1. Assuming that all acid of the 1:1 reaction mixture would be consumed in the substitution reaction (eq. 1.4) the second step, the ester formation (eq. 1.5), and subsequently the condensation reaction (eq. 1.6) with formation of the oxo cluster would not occur. This apparent contradiction can be explained in different ways: [21]

(I) Substitution according to eq. 1.4 might be an equilibrium, and esterification according to eq. 1.5 largely irreversible. The acid in equilibrium might react with the cleaved alcohol thus shifting the equilibrium towards the formation of oxo species.

(II) In a non-hydrolytic reaction metal-oxo bridges are formed under elimination of ester or ether. Ester cleavage was observed before for the cluster $Ti_6O_4(OOCCH_3)_8(OEt)_8$ which rearranges to the more condensed cluster $Ti_6O_6(OOCCH_3)_6(OEt)_6$ upon aging. [22] Similarly the cluster $Ti_4O_2(OOCH)_2(O^iPr)_{10}$ degrades upon aging under formation of $HCOO^iPr$. The tranesterification rate is increased at higher temperatures. [20]

Fehlner et al. observed the formation of $Ti_4(\mu_3\text{-}O)[\mu\text{-}(CO)_9Co_3(\mu_3\text{-}CCOO)]_4(OR)_4$ after reacting $Ti(OR)_4$ ($R = CH(CH_3)_2$, $(CH_2)_3CH_3$) and $(CO)_9Co_3(\mu_3\text{-}CCOOH)$ in the ratio $1:2$. Ester formation was not observed, but instead the formation of the ether $[(CH_3)_2CH]_2O$ and the free alcohol $(CH_3)_2CHOH$. [23] Hence both non-hydrolytic reaction mechanisms, the transesterification (eq. 1.7) and ether elimination (eq. 1.8) can occur.

$$Ti\text{—}OOCR + Ti\text{—}OR' \rightarrow Ti\text{—}O\text{—}Ti + RCOOR' \tag{1.7}$$

$$2\,Ti\text{—}OR \rightarrow Ti\text{—}O\text{—}Ti + ROR \tag{1.8}$$
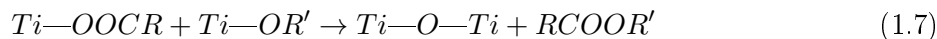
The reactions described above lead to a defined growth of carboxylate-substituted oxo clusters which are often obtained as crystalline products from the reaction mixture. [24] [21] Thereby the size of the cluster, the degree of condensation, the shape and the chemical functionalities on the cluster surface can be controlled by experimental parameters such as:

- Acid to metal alkoxide ratio

- Type of alkoxo groups

- Type of carboxylic acid

- Reaction conditions

Metal alkoxide to acid ratio: Reaction of $Zr(OBu)_4$ with 1.6 eq. of methacrylic acid led to the formation of $Zr_6O_2(OMc)_{10}(OBu)_{10}$. [25] The same reaction with 4 or 7 eq. of methacrylic acid led to the formation of the clusters $Zr_6O_4(OH)_4(OMc)_{12}$ and $Zr_4O_2(OMc)_{12}$. [26] The latter two clusters can also be obtained by reaction of 4 eq. of methacrylic acid with $Zr(OPr)_4$ giving $Zr_6O_4(OH)_4(OMc)_{12}$ as the product and 15 eq. of methacrylic acid with $Zr(OPr)_4$ giving $Zr_4O_2(OMc)_{12}$ as product. [26] A higher proportion of acid generally promotes the *in situ* generation of water, and clusters with a higher degree of condensation are obtained. In cases where the proportion of the acid is low, not all of the alkoxo groups of the metal alkoxide can

be substituted and a less condensed cluster core with a mixed ligand sphere of alkoxo and carboxy ligands is obtained (e.g. $Zr_6O_2(OMc)_{10}(OBu)_{10}$ and $Zr_6O_4(OH)_4(OMc)_{12}$). When the concentration of the acid is high enough, the substitution reaction of alkoxo ligands is favoured and less condensed cores with a high number of carboxylate ligands is obtained (e.g. in the case of $Zr_4O_2(OMc)_{12}$). [25] The higher degree of condensation upon increasing the proportion of acid in the reaction mixture is also evidenced by the formation of the Ti clusters $Ti_4O_2(OFormate)_2(O^iPr)_{10}$ (OFormate = formate) and $Ti_6O_6(OFormate)_6(OR)_6$. While the first one was formed by a $1:1$ reaction of $Ti(O^iPr)_4$ and formic acid, the latter is formed with a stoichiometry of metal alkoxide to formic acid of $1:2$. [20]

Type of carboxylic acid: The type of carboxylic acid has an influence on the formation of the cluster. This stems mainly from steric and / or electronic effects. Reaction of methacrylic acid with $Zr(OPr)_4$ in the ratio $1:4$ led to the formation of the cluster $Zr_6O_4(OH)_4(OMc)_{12}$ as described above. Reaction with the same metal alkoxide to acid ratio but with 2-bromoisobutyric acid led to the cluster $Zr_5O_4(BrC(CH_3)_2COO)_{10}(OPr)_2$. [27]

Type of metal alkoxide: The type of the alkoxo groups of the metal alkoxide affects the degree of oligomerization as discussed before. Hence the hydrolysis rate differs for two alkoxides which differ in steric demand of the alkoxo group OR. Reactions under the same experimental conditions of two metal alkoxides differing in their OR groups result in the formation of different clusters. This was shown by the reaction of $Ti(OPr)_4$ and $Ti(O^iPr)_4$ with 2 eq. of acrylic acid. The cluster $Ti_6O_4(OAcr)_8(OPr)_8$ (OAcr = acrylate) was formed by reacting $Ti(OPr)_4$ with acrylic acid, while the same reaction with $Ti(O^iPr)_4$ as the metal alkoxide precursor led to the formation of $Ti_4O_2(OAcr)_6(O^iPr)_6$. [28]

Other experimental conditions: Solvent influence can be observed, which might stem from a different degree of oligomerization of the metal alkoxide in different coordinating or non-coordinating solvents. Furthermore an increased reaction temperature favors the esterification reaction and increases the amount of *in situ* generated water.

It is hard, if not impossible, to predict the shape, degree of condensation or size of the cluster on the basis of the reaction conditions. Nevertheless, the reactions are characterized by high yields and high reproducibility when all the reaction parameters are precisely controlled.

Clusters of different shape and size, comprising different metal or mixed metal systems and bearing different functional and non- functional ligands were synthesized in the past. Thereby

some cluster core features can often be found independent on the ligands which cap the core. A summary of frequent Zr oxo cluster core types is shown in Fig 1.1
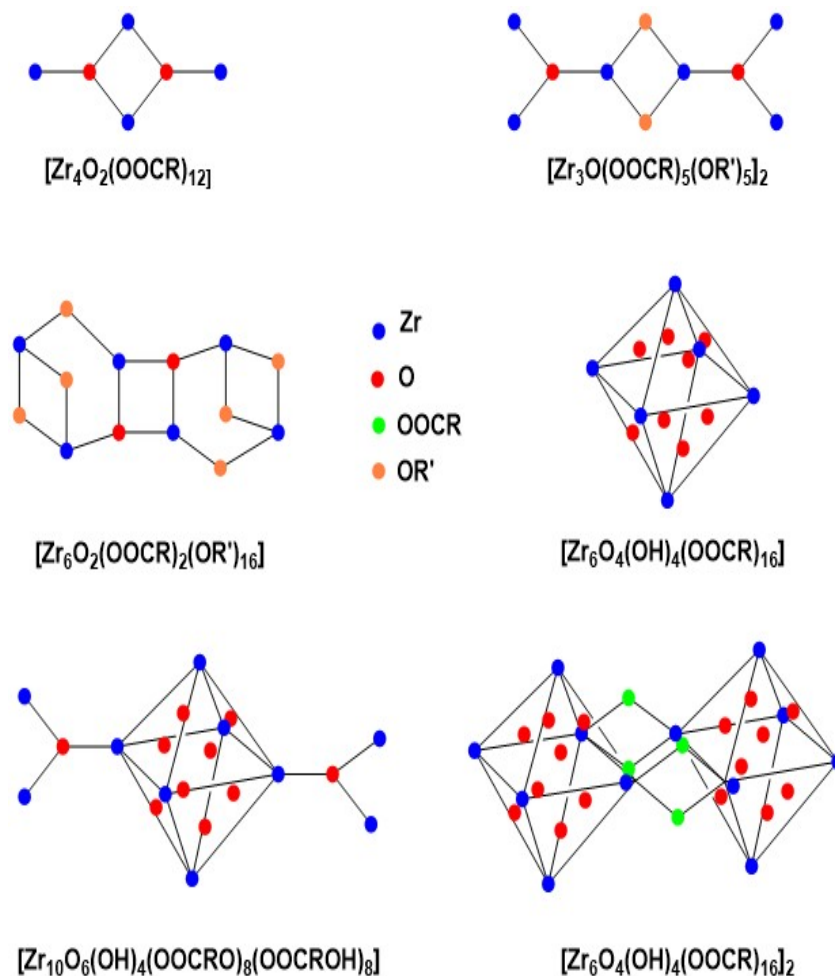
Figure 1.1: Typical Zr oxo cluster core types

The cluster $Zr_4O_2(OMc)_{12}$ (OMc = methacrylate), for example, was formed by reaction of $Zr(OBu)_4$ with 7 eq. of methacrylic acid. [26] Reaction of $Zr(OBu)_4$ with 4 eq. methacrylic acid resulted in the more condensed structure of $Zr_6(OH)_4O_4(OMc)_{12}$. [26] Decreasing the amount of acid to 1.6 eq. resulted in the formation of the cluster $Zr_6O_2(OMc)_{10}(OBu)_{10}$. [25] Reacting 7 eq. of methacrylic acid with $Zr(OBu)_4$ in the presence of 1 eq. of (3-methacryloxypropyl)-trimethoxysilane resulted in the formation of the isostructural cluster $Zr_6O_2(OMc)_{14}(OMe)_4(OBu)_2$. Thereby the methoxy groups are provided by the silane. [25] These examples of Zr clusters differ in the size and shape of the cluster cores. $Zr_4O_2(OMc)_{12}$ has an open centrosymmetric structure, where all four Zr atoms are coplanar. In $Zr_6O_4(OH)_4(OMc)_{12}$ the six Zr atoms are arranged in a more condensed octahedron. All the faces of the octahedra are capped either by μ - O or μ - OH

groups. The isostructural clusters $Zr_6O_2(OMc)_{14}(OMe)_4(OBu)_2$ and $Zr_6O_2(OMc)_{10}(OBu)_{10}$ are composed of two Zr_3O subunits which are connected through bridging butoxo or methoxo ligands. The core of the cluster $Zr_6O_4(OH)_4(OOCR)_{12}$ cluster seems to be a structural prototype. The clusters $Zr_6O_4(OH)_4(OOCPh)_{12}$ [29], $Zr_6O_4(OH)_4(OOCCMe=CH_2)_{12}$ [29], $Zr_6O_4(OH)_4(OOCBu^t)_{12}$ [30], $Zr_6O_4(OH)_4(OOCC(CH_3)_2Et)_{12}$ [30] and $Zr_6(OH)_8(OMe)_4(OOCCHPh_2)_{12}$ [31], with the same $Zr_6O_4(OH)_4$ core were prepared by reaction of $Zr(OPr)_4$ with the respective carboxylic acids.

Reaction of bifunctional carboxylic acids such as 1-hydroxy-β-naphthoic acid or salicylic acid with Zr alkoxides are interesting in a sense that both the carboxy and the hydroxy group can potentially coordinate to the metal atom. Reaction of $Zr(OPr)_4$ with a ten-fold excess of 1-hydroxy-β-naphthoic acid resulted in the cluster $Zr_6O_2(OOC-C_{10}H_6O)_2(OPr)_{16}(PrOH)_2$. This cluster shows a low degree of condensation with two terminally coordinated carboxylate ligands. The hydroxy groups are deprotonated and coordinate to the Zr atoms. Reaction of $Zr(OPr)_4$ with a ten-fold excess of salicylic acid resulted in the formation of the cluster $Zr_{10}O_6(OH)_4(OO-C_6H_4O)_8(OOC-C_6H_4OH)_8$. In four of the eight carboxylate ligands the hydroxy groups remain protonated and do not coordinate to the metal centers, while the remaining four carboxylate ligands show also coordination of the hydroxy groups. The structure of the cluster core resembles that of the $Zr_6O_4(OH)_4$ core. Six of the Zr atoms are arranged in an octahedral fashion and capped by four μ-OH ligands. The remaining planes of the octahedron are capped by the hydroxy groups of the salicylic acid ligand. On the terminal side each two Zr atoms are condensed to the octahedral core. These two Zr atoms are capped by four salicylic acid ligands which coordinate only through the carboxylate function. [32]

The $Zr_6O_4(OH)_4$ core structure appears also in a dimeric form ($[Zr_6O_4(OH)_4(OOCR)_{12}]_2$) which was first reported for the acrylate substituted cluster $[Zr_6O_4(OH)_4(OOCCH=CH_2)_{12}]_2$ by reacting $Zr(OPr)_4$ with a 6.5-fold excess of acrylic acid. [29] The dimer consists of two $Zr_6O_4(OH)_4$ units which are connected through four bridging carboxylate ligands. This structure can be obtained with a variety of organic ligands, such as acetate ($[Zr_6O_4(OH)_4(OOCMe)_{12}]_2$) [33], propionate ($[Zr_6O_4(OH)_4(OOCCH_2Me)_{12}]_2$) [33], vinylacetate ($[Zr_6O_4(OH)_4(OOCCH_2CH=CH_2)_{12}]_2$) [33], dimethacrylate ($[Zr_6O_4(OH)_4(OOCCH=CMe_2)_{12}]_2$) [33], and with a mixed ligand system by applying a mixture of carboxylic acids (propionate/methacrylate $[Zr_6O_4(OH)_4(OOCCH_2Me)_3(OMc)_9]_2$ or acetate/methacrylate $[Zr_6O_4(OH)_4(OOCMe)_8(OMc)_4]_2$). [33] NMR studies revealed that the dimeric structure can not be converted in the monomeric $Zr_6O_4(OH)_4(OOCR)_{12}$ cluster in solu-

tion. Furthermore ligand exchange on clusters with the dimeric structure showed that all except the bridging ligands connecting the two dimers can be exchanged.[33] Thus, the monomeric and dimeric structure of clusters of the type $Zr_6O_4(OH)_4$ are individual species, and the monomeric and dimeric forms are not connected through an equilibrium. Both the monomeric and dimeric form exist also for the Hf analogues (e.g. $[Hf_6O_4(OH)_4(OOCR)_{12}]_2$ [33] [34], $Hf_6O_4(OH)_4(OOCMe)_{12}$ [35] [36] and $Hf_4O_2(OMc)_{12}$ [36]).

Controlled hydrolysis of a mixture of metal alkoxides with carboxylic acids leads to the formation of mixed-metal clusters. Reaction of $Ti(OBu)_4$ or $Ti(OEt)_4$, $Zr(OBu)_4$ and methacrylic acid in the ratio $1:1:8.5$ resulted in the formation of the cluster $Ti_4Zr_4O_6(OMc)_{16}(OBu)_4$. [24] Replacing $Zr(OBu)_4$ with $Hf(OBu)_4$ resulted in the formation of the Hf analogue, where each Zr atom is replaced by a Hf atom. [35] Increasing the amount of $Zr(OBu)_4$ from $1:1$ to $1:2$ resulted in the formation of the cluster $Ti_2Zr_4O_4(OBu)_2(OMc)_{14}$. [24] These two clusters were obtained in almost quantitative yield. Further increase of the $Ti(OBu)_4:Zr(OBu)_4$ ratio to $1:3$ results in the formation of a mixture of clusters. A third type of cluster, namely $Ti_4Zr_2O_4(OMc)_{10}(OBu)_6$, was formed when $Ti(OBu)_4$ and $Zr(OPr)_4$ were reacted with methacrylic acid in the ratio $1:1:8.2$. [24]

Other mixed-metal clusters were obtained from reacting mixtures of $Ti(OPr)_4$ and $Y(OCH_2CH_2OCH_3)_4$ and a seven-fold excess of methacrylic acid. The cluster $Ti_4Y_2O_4(OMc)_{14}(OCH_2CH_2OH)_2$ was obtained when the Ti:Y ratio exceeded 3.5. A ring structure with the formula $Ti_4Y_2O_4(OMc)_{12}(OCH_2CH_2OMe)_2(McOH)_2$ was obtained with a Ti:Y ratio of 2. [37]

Besides the Zr oxo cluster and the mixed-metal oxo clusters described above a vast number of Ti oxo clusters was reported. They are either formed by hydrolysis of $Ti(OR)_4$ precursors with stoichiometric addition of water or by reacting the Ti alkoxide precursors with carboxylic acids, similar to the synthesis described for Zr oxo clusters before. Hydrolysis of Ti alkoxides by addition of stoichiometric amounts of water results in the formation of Ti oxo alkoxo clusters. Hydrolysis in the presence of carboxylic acid results in the formation of clusters, where the carboxylate ligands coordinate to the cluster surface. As for the Zr oxo clusters, typical core structures are found and are shown in Fig 1.2. In the following a short summary of the Ti oxo carboxylate clusters will be given.

The cluster $Ti_2O(OOCCCl_3)_4(O^iPr)_2(HO^iPr)_2$ is the smallest Ti oxo carboxylate compound reported and was obtained by reacting $Ti(O^iPr)_4$ with 2 eq. of trichloroacetic acid. [39] Two Ti
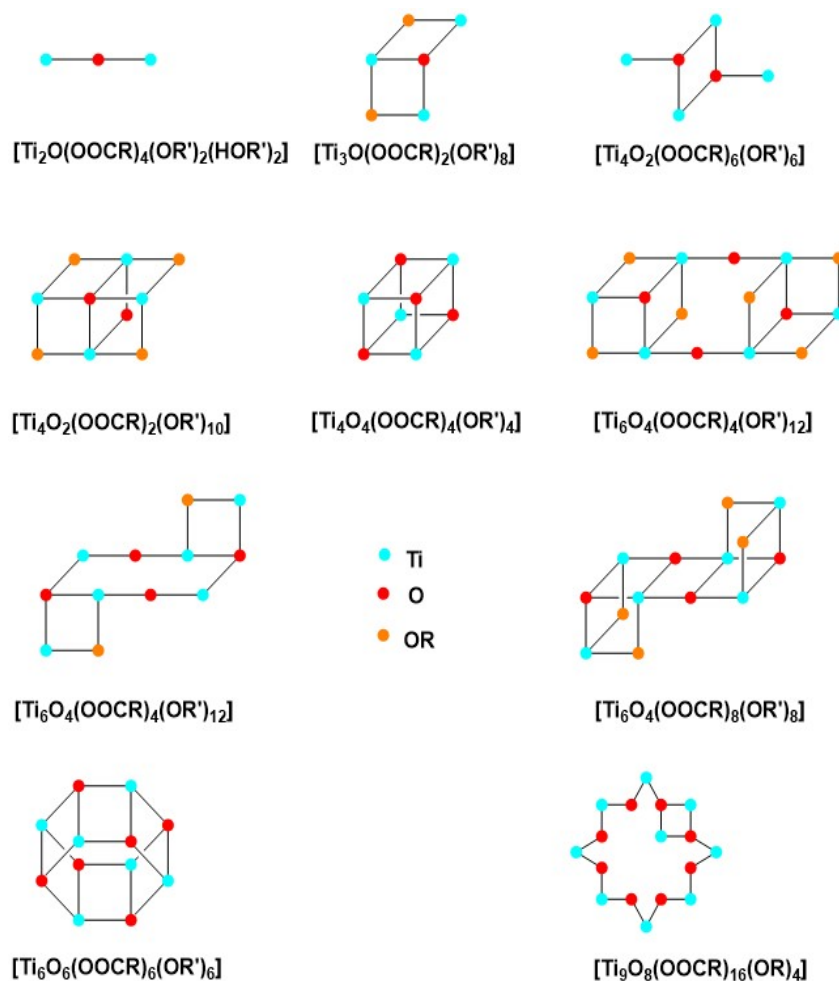
Figure 1.2: Main core structures of Ti oxo carboxylate clusters[38]

atoms are connected through a μ-oxo group and additionally two bridging carboxylate ligands connect the Ti octahedra. Terminal carboxylate and alkoxo ligands complete the coordination sphere of the Ti atom. The trimeric cluster $Ti_3O(OOCR)_2(OR')_8$ (R' = OCH_2CMe_3) was reported for a variety of different carboxylate ligands, such as formiate, acetate and ^{t}butylacetate (R = H, Me, CH_2CMe_3)[40] or benzoate (R = OOCPh)[41]. In a first step the precursor $[Ti(ONep)_4]_2$ (ONep = neopentoxide) was derived from reaction of $Ti(O^iPr)_4$ and neopentyl alcohol. Reaction with 1 eq. of formic acid or acetic acid or with 2 eq. of pivalic acid acid resulted in the formation of the trimeric clusters. The formation of the benzoate analogue, however, follows a different synthetic approach. Starting from preformed Ti oxo alkoxo clusters $Ti_3O(O^iPr)_{10}$ or $Ti_3O(O^iPr)_9(OMe)$[42] the cluster $Ti_3O(O^iPr)_8(OOCPh)_2$ was obtained by reaction with 1.5 eq. of benzoic acid. This reaction corresponds to a ligand exchange reaction where two bridging monodentate alkoxo ligands are replaced by bidentate carboxylates. In all structures two of the Ti atoms are six-fold coordinated while the third Ti atom shows a coordination number of five.

This is not unexpected for Ti clusters where the Ti atoms often show a coordination number of 5 or 6. Ti atoms with a coordination number of 4 can be found in rare cases.

Three different tetrameric Ti oxo structures were reported. The structures of $Ti_4O_2(OOCR)_6(O^iPr)_6$ (R = CH=CH$_2$ and C(CH$_3$)=CH$_2$) [28] are derived from reaction of $Ti(O^iPr)_4$ with 2 eq. of methacrylic or acrylic acid. This cluster core resembles that of the $Zr_4O_2(OMc)_{12}$ cluster. Ti atoms provide fewer coordination sites compared to Zr atoms. This has an influence on the degree of substitution of (monodentate) alkoxo ligands with (bidentate) carboxylate ligands. [28] All carboxylates in the $Ti_4O_2(OOCR)_6(OR')_6$ cluster are bridging. This is commonly found for Ti oxo carboxylate clusters, whereas Zr oxo carboxylate clusters often show at the same time bridging and chelating carboxylates in the structure.

The second tetrameric structure occurs in the form $Ti_4O_2(OOCR)_2(O^iPr)_{10}$ (R = H or ^iPr). [20] [43] It is composed of two face-sharing [Ti$_4$O$_4$] units which have each one non-shared Ti atom removed. All Ti atoms are six-fold coordinated and connected through bridging alkoxo groups. Additionally a rare μ_4-oxo bridge was found. Both clusters were prepared by different synthetic pathways. The formiate cluster was obtained by reaction of $Ti(O^iPr)_4$ with 1 eq. of formic acid [20], while the isopropyl carboxylate cluster was prepared from reaction of $Ti(O^iPr)_4$ in presence of CO_2 under non inert conditions. The water content of the CO_2 acted as water source in the formation of the cluster, while CO_2 was inserted in the isopropoxy ligands. [43]

The third type of tetrameric structure comprises the general formula $Ti_4O_4(OOCR)_4(OR')_4$ (R = (μ-(CO)$_9$Co$_3$(μ_3-CCOO), R' = $^iPr_2$, (CH$_2$)$_3$CH$_3$, C$_6$H$_5$ or 2,6-(CH$_3$)$_2$-C$_6$H$_3$). [44] [23] These clusters were prepared by reaction of the metal alkoxides (M(OR)$_4$ (R = ^iPr [44] [23], (CH$_2$)$_3$CH$_3$ [23], C$_6$H$_5$ [23] and 2,6-(CH$_3$)$_2$C$_6$H$_3$ [23]) and the cluster acid (CO)$_9$Co$_3$(μ-CCOOH). The structure of the cluster is a cube where the vertices are capped alternatingly by Ti and oxygen atoms.

Four types of hexanuclear cluster cores are commonly found. The cluster with the formula $Ti_6O_4(OOCR)_4(OR')_{12}$ exists in two types. The first type (R = Me and R' = ^iPr [45] or R = CCo$_3$(CO)$_9$ and R' = ^iPr [44] [23]) consists of two cubes. Three Ti atoms per cube are connected through one μ oxo bridge and through three bridging alkoxo ligands. The remaining eighth vertex of the cube stays unoccupied by ligands. The two cubes are connected with each other through two μ-oxo groups. The second type (R = CCo$_3$(CO)$_9$ and R' = Et [44] [23] consists of two [Ti$_3$O$_4$] fragments which are composed of two μ-oxo groups and one bridging alkoholate ligand. Each of the μ-oxo groups serves as linking point to the second [Ti$_3$O$_4$] fragment. The

cluster structure of $Ti_6O_4(OOCR)_8(OR')_8$ ($R = CH_3$ [18] and $R = BrC(CH_3)_2$ [27] and $R' = {}^iPr$; $R = CH_3$ [46] and $R = OMc$ [28] and $R' = Et$ or $R = OAcr$ and $R' = Pr$ [28]) consists also of two Ti_3 subunits which are connected through two μ_3-oxo bridges and four carboxylate ligands. The three Ti atoms in each unit are connected through one μ_3 oxo group, and bridging carboxylate and alkoxo ligands.

The core structure of the cluster type $Ti_6O_6(OOCR)_6(OR')_6$ is a hexaprismatic arrangement where the vertices are occupied alternatingly by Ti or μ_3-O atoms. This gives two $[Ti_3O_3]$ units which are connected through the μ-oxo bridge of the units and through six bridging carboxylate ligands. Each Ti atom is additionally capped by a terminal alkoxo ligand. Clusters of this structure type are reported with a vast number of different OOCR or OR' ligands, e.g. $R = Me$ or PhOPh and $R' = Et$, [22]; $R = Me$ [22] [47], $CHCl_2$ [39], H [20], Bz [48] and ^tBu [49] and $R' = {}^iPr$ or $R = {}^iPr$ and $R' = Nep$, [40].

To increase the moisture stability, alkoxo groups were replaced by trimethylsilyloxy groups. This was done by using $Ti(OSiMe_3)_4$ as precursor for the reaction with carboxylic acid and resulted in the formation of several clusters of the stoichiometry $Ti_6O_6(OOCR)_6(OSiMe_3)_6$ ($R = {}^tBu$, $CH_2{}^tBu$, $C(CH_3)_2Et$). [50]

The heptameric structure $Ti_9O_8(OMc)_{16}(OR)_4$ consists of a ring where the Ti octahedra are corner-sharing. Two octahedra share the same edge. The carboxylate and alkoxo ligands are bridging around the wheel. [51] Other Ti oxo clusters comprising more then 7 Ti atoms are known, but such structures do not occur often. The largest Ti cluster which was crystallized is $Ti_{28}O_{40}(OOCMe)_{12}(O^tBu)_{20}$ [52].

1.3 Ligand Exchange Reactions of Transition Metal Oxo Clusters

Preparation protocols based on the hydrolysis and condensation reactions of metal alkoxides in presence of carboxylic acids lead commonly to products with a mixed alkoxo/carboxylate ligand sphere or to products with only one type of carboxylate ligands. Attempts have been made to synthesize clusters with different functionalized or non-functionalized ligands bonded to the same cluster core. This allows to introduce a second functionality, or to decrease and control the number of functional ligands. One way to control the composition of the ligand sphere is an *in-situ* approach, where a mixture of carboxylic acids is reacted with the metal alkoxide. Examples are the clusters $[Zr_6O_4(OH)_4(OOCCH_2Me)_3(OOCC(Me)=CH_2)_9]_2$ and $[Zr_6O_4(OH)_4(OOCMe)_8(OOCC(Me)=CH_2)_4]_2$ which were prepared by reaction of $Zr(OBu)_4$ with mixtures of methacrylic acid/propionic acid or methacrylic acid/acetic acid respectively [33], and the cluster $Zr_6O_4(OH)_4(OMc)_8(isobutyrate)_4$ which was obtained from reaction of isobutyric acid and methacrylic acid with $Zr(OBu)_4$. [53]

Nevertheless, the *in situ* approach often does not allow to predetermine which cluster type will be formed. A more directed approach is the ligand exchange on preformed clusters. Ligand exchange reactions with nucleophilic incoming ligands have been performed in the past, allowing a more defined control on the ligand sphere. Since ligand exchange reactions are equilibrium reactions, the proportion of the exchanged ligands depends on the amount of incoming ligands in the reaction solution and steric or electronic effects of incoming and leaving ligands. Despite reports of successful ligand exchange reactions of transition metal oxo clusters, [53] [54] [55] [56] [57] [58] degradation of the cluster core was also observed. Thus ligand exchange reactions need an exact balance of the charge and the coordination ability of the incoming ligand. [41] [59]

Several coordination modes of the ligands are reported in literature. Depending on the ligand, terminal coordinating or bridging alkoxo and chelating or bridging carboxylate ligands were found. Fig. 1.3 shows a survey of the most commonly found coordination modes for alkoxo and carboxylate ligands.

The possibility of cluster degradation upon ligand exchange is minimized when the incoming ligand has the same charge as the leaving group and can coordinate in the same way. However, the intactness of the cluster core must be verified experimentally in every case after the ligand exchange reactions. This can be done by different characterization techniques, such as
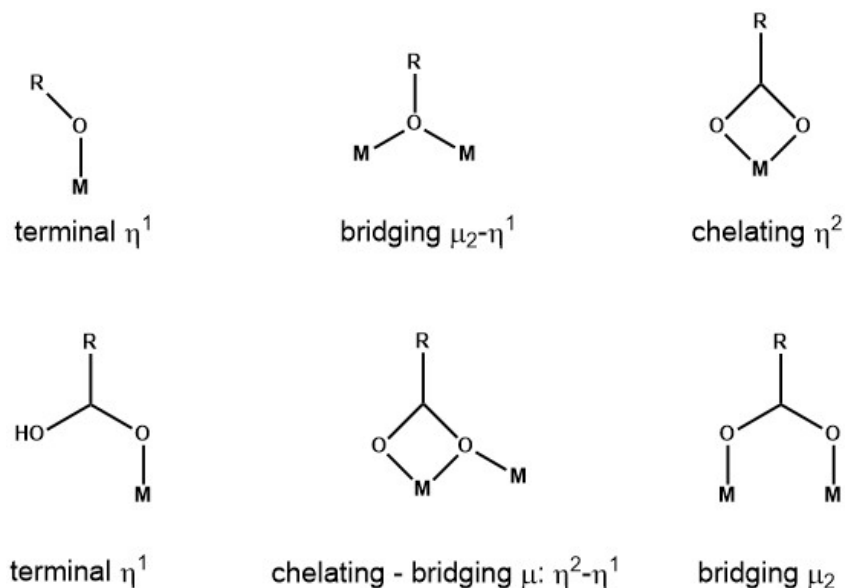
Figure 1.3: Typical coordination modes of alkoxo and carboxylate ligands according to [60] and [61] .

two dimensional NMR spectroscopy, when necessary at low temperatures, single crystal X-ray diffraction or FTIR spectroscopy.

Ligands on the cluster surface are subject to dynamic exchange processes in solution. Two kinds of dynamic exchange can be distinguished, which is the exchange of cluster-bonded carboxylate groups with free carboxylic acid and a dynamic behavior of cluster-bonded carboxylates. The exchange process is facilitated by free carboxylic acid, which is often weakly bonded to the cluster core through hydrogen bonding. The free acid is hard to remove during purification steps and can therefore participate in exchange processes when the cluster is dissolved. The latter exchange process may proceed through concomitant change of the coordination mode between bridging and chelating carboxylate ligands and was verified by two-dimensional NMR spectroscopy and DFT calculations.[62] This was also confirmed by an interesting structural study, which verified that the cluster $Zr_4O_2(OMc)_{12}$ exists in two isomers. In the symmetric crystal structure ten methacrylate ligands are bridging, while the two terminal methacrylate ligands are chelating. This leads to a symmetric structure with a molecular symmetry of C_{2h}.[63] In the asymmetric structure one of the bridging methacrylate ligands shows a bridging/chelating coordination mode.[26] This breaks the molecular symmetry which is then C_1. The solution NMR spectra however are identical and show one set of signals for the methacrylate ligands at room temperature. Upon cooling to -80 °C a splitting in four sets of signals is seen, in accordance with the C_{2h} symmetry.[62] This dynamic behaviour of the ligands makes an easy interpretation

of NMR spectra impossible and often prevents an exact determination of the composition of the ligand sphere in mixed‑ligand clusters by NMR spectroscopy.

1.4 Hybrid Materials

One research focus in the field of materials chemistry was set by the development of hybrid materials, in which typically an inorganic and organic component are combined on a molecular level. New materials were developed which showed improved mechanical, thermal, electrical and magnetical characteristics and whose outstanding properties can be traced back to synergistic effects between the organic and inorganic entities. The choice of the inorganic or organic component, the proportion of each component in the hybrid material and the structure of the hybrid materials allows a tailoring of properties ranging from purely organic to purely inorganic materials. The big advantage of hybrid materials lies in the possibility (a) to overcome structural limits of conventional materials, (b) to allow a fine-tuning of the materials properties through variation of composition, interface interaction and microstructure, (c) of a possible multifunctional design approach for materials and (d) of virtually infinite compositional variability. [64]

Two classes of hybrid materials are generally distinguished. In Class I hybrid materials the two phases interact only weakly with each other, thus the inorganic moieties are entrapped in the organic matrix or vice versa (see Fig. 1.4). Examples are materials where the inorganic moiety is entrapped in an organic polymer (blends) or two interpenetrating networks of purely organic and inorganic compounds, which are not covalently bonded to each other. The kinds of interaction between the two phases are typically van der Waals forces, hydrogen bonding or electrostatic interactions. Class II hybrid materials on the other side refer to materials where the two compounds strongly interact with each other. This includes strong covalent or ionic bonding between the two moieties. This type of interaction, for example, can be found where functionalized inorganic clusters or nanoparticles (e.g. polyhedral oligomeric silsesquioxanes (POSS), polyoxometalates (POM) or oxo clusters) are connected to a polymer backbone by covalent linkage. Depending on the number of polymerizable groups on the particle surface different types of polymer structures can be obtained. In cases where only one polymerizable group is attached to the particle, polymers with pending inorganic moieties are obtained upon polymerization. When two or more polymerizable groups are attached, crosslinked polymers are obtained. Core-shell structures can be obtained when the ligands bear functionalities capable of initiating a polymerization reaction (see Fig. 1.4). Another example are dual network structures of organic and inorganic components, which are covalently bonded to each other. For example, an inorganic network can be formed by the sol-gel process. A polymerizable group stays thereby connected to the inorganic network. In a second step a polymerization reaction is initiated which leads to formation of an organic poly-

mer. In this step the polymerizable groups of the inorganic network can react with the organic monomers and thereby covalently link the two networks to each other.
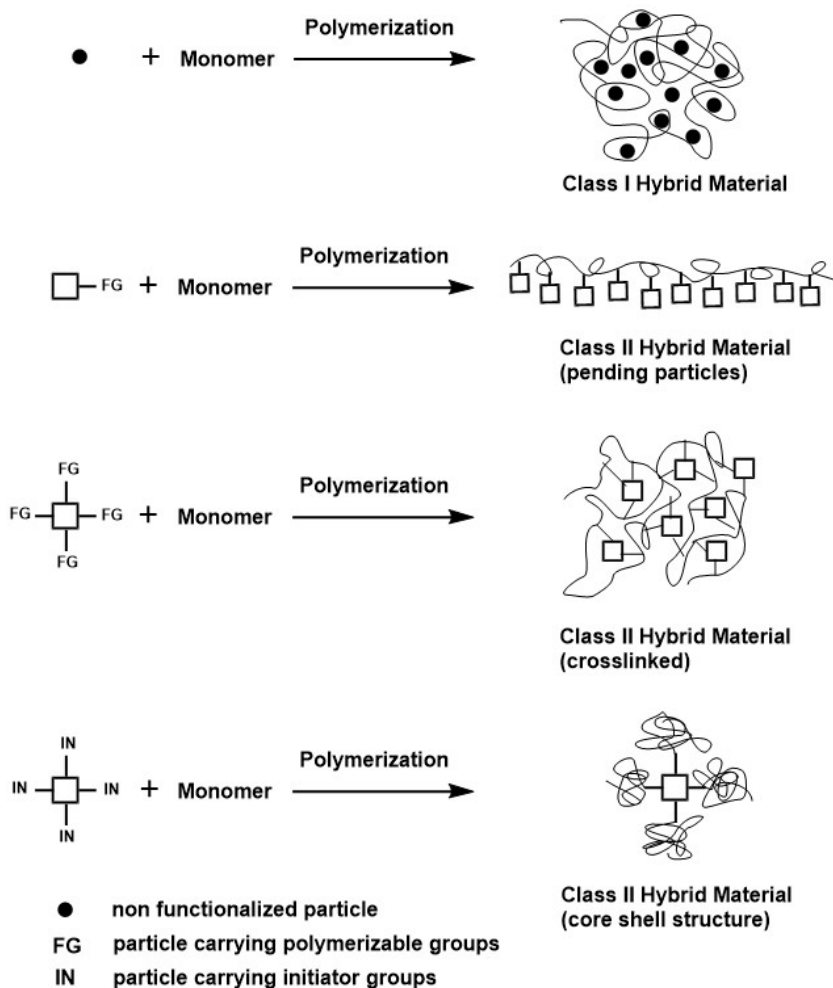
Figure 1.4: Different types of Class I and Class II hybrid materials.

Contrary to Class I hybrid materials, covalent linkage of the components overcomes the problem of phase separation or leaching. While the entrapped entity in Class I hybrid materials can migrate and segregate, and synergistic effects may get lost over time, Class II hybrid materials show enhanced mechanical and thermal properties over a long time period. A comprehensive discussion of hybrid materials in general would be beyond the scope of this work and the following discussion will be focused on transition metal oxo cluster-based hybrid materials only. Nevertheless, the reader might be referred to numerous review articles which cover comprehensively the research progress and application of hybrid materials in the last decade.[65] [66] [38] [67] [68] [69] [70] [71] [64]

Tailoring of hybrid material properties is often facilitated by a synthetic approach based on assembling of nanosized building blocks (NBBs) and has been used in the past for the development

of new materials. In this approach NBBs are nanometer sized, preformed entities of uniform size and shape, which can be incorporated in organic polymers by standard polymerization reactions. This bottom-up approach allows accurate control over morphology and structure of the hybrid material. Furthermore the compatibility of the NBB with the organic phase can be controlled through surface modification. Transition metal oxo clusters capped with polymerizable functional groups meet these criteria and are used as inorganic component in hybrid materials. The advantages of transition metal oxo clusters for the preparation of hybrid materials are their (a) structurally well defined shape and size, (b) defined composition, (c) the possibility to perform surface modification reactions and (d) the possibility to transfer intrinsic cluster properties to the final hybrid material. [72] [73] The cluster plays a dual role in the hybrid material: Clusters are usually capped with a great number of (uniform) polymerizable ligands. Cluster derived hybrid materials are therefore often strongly crosslinked. This influences typical polymer properties such as glass transition temperature (T_g), depolymerization temperature and mechanical strength. At the same time the clusters acts as inorganic fillers in an organic matrix. Inorganic fillers commonly show enhancement of thermal properties such as increased decomposition temperature. Thus two effects, the crosslinking effect and the filler effect, determine the thermal and mechanical properties of the final hybrid material. In practice this is reflected by changing the materials properties through the amount of cluster incorporated and the type (size, shape, number of polymerizable ligands on the cluster surface) of clusters used. In addition the cluster can carry, beside polymerizable groups, additional functional groups which can be incorporated in the hybrid material and which are active after polymerization for further chemical reactions.

It was shown that UV polymerization of acrylate monomers in the presence of the cluster $Zr_4O_2(OMc)_{12}$ resulted in polymers with increased storage and loss moduli and increased T_g. [74] The same result was obtained by polymerizing the cluster $Zr_4O_2(OMc)_{12}$ in the presence of styrene through a stepwise thermally initiated free radical polymerization. [75] Even small amounts of the cluster are sufficient to improve mechanical properties through cosslinking. This was shown by copolymerizing the cluster $Ti_6O_4(OEt)_8(OMc)_8$ (0.3 wt%) in the presence of methylmethacrylate. The obtained hybrid material showed an increased T_g compared to the undoped polymer. [76] The cluster $Zr_4O_2(OMc)_{12}$ was UV cured in presence of an acrylic resin and showed increased T_g values at a cluster loading of 15 wt% At the same time thermal stability was enhanced and the surface hardness of the polymer was improved. [77]

The improvement of thermal properties can be traced back to the crosslinking of the polymer network, which prevents thermal depolymerization, as well as to the presence of an inorganic

filler. This was shown by co-polymerization of the clusters $Zr_6O_4(OH)_4(OMc)_{12}$, $Zr_4O_2(OMc)_{12}$, $Ti_6O_4(OEt)_8(OMc)_8$ or $Ti_4O_2(O^iPr)_6(OAcr)_6$ with methylmethacrylate in the range of 0.5-2 wt% cluster. All hybrid materials showed increased thermal degradation temperatures which stem from inhibited thermal depolymerization. Increasing the cluster loading increases the crosslinking density of the polymer. At the same time an increase of cluster content also increases the amount of inorganic filler in the polymer and leads to a more pronounced filler effect. The two effects can therefore not be decoupled at this stage. [78] Crosslinking of monomer resins with 0.5 mol% $Zr_6O_4(OH)_4(OMc)_{12}$ resulted in an increase of the decomposition temperature by 100 °C for methylmethacrylate and 50 °C for styrene-based polymers as evidenced by thermogravimetric analysis (TGA). [79]

Besides increased thermal stability and increased mechanical properties (T_g, storage and loss moduli) it was shown that crazing of the polymer is influenced by the cluster loading. Polystyrene samples with cluster loadings of 0.43, 0.70 and 0.87 mol% showed decrease in crazing upon increasing the cluster content in the polymer. Crazing was completely suppressed in case of 0.87 mol%. [80] Micro-indentation measurements revealed increased hardness and an increase of the craze initiating stress in $Zr_6O_4(OH)_4(OMc)_{12}$ reinforced polystyrene samples. A reduction of pile-up and a stronger recovery was found in scratch tests for the same samples. [81]

Effective crosslinking of the polymer through incorporation of clusters can be shown by swelling experiments. While linear, essentially non-crosslinked polymers tend to dissolve in theta solvents (solvents where polymer coils act like ideal chains), crosslinked polymers show swelling behaviour. The amount of solvent uptake increases with decreasing crosslinking density. Cluster-reinforced polymers swell to a certain extent when placed in theta solvents. The amount of solvent uptake depends on the cluster content and points to a stronger crosslinking at higher cluster loading. [78] [74] [75] [82]

Besides the amount of cluster, the type (size, shape) of the cluster shows an effect on the materials properties. The exact reason for the influence of the cluster type on polymerization is unknown. [83] Impedance spectra were recorded of cluster-doped PMMA samples and showed that the capacitance of the hybrid material decreased with increasing cluster loading. Doping of methylmethacrylate with 2 mol% $Zr_4O_2(OMc)_{12}$ showed an increase of the conductivity by $0.9 \cdot 10^{-7}$ S cm^{-1}. [78] Films of $Zr_4O_2(OMc)_{12}$-doped PMMA were characterized by dielectric spectroscopy. The films showed a dielectric constant of 1.93 at room temperature and 1kHz. This renders application of these hybrid materials as dielectric materials feasible. [84] [85] Intrinsic cluster-related properties were transferred to the polymer as was shown by polymerization of

ethyl acrylate in the presence of the superparamagnetic cluster $Mn_{12}O_{12}(OAcr)_{16}$. The resulting polymer also showed superparamagnetic behaviour. [86]

Different polymerization techniques were applied to incorporate clusters in an organic matrix. The choice of the polymerization technique is thereby predefined by the functionality of the polymerizable ligands of the clusters and the compatibility with the organic monomer. Most often thermally or UV initiated free radical polymerization were used. Especially the acrylate and methacrylate functionalized clusters dissolve readily in acrylic, methacrylic or styrene monomers and can be polymerized upon addition of thermal or photoinitiators. [74] [77] [76] [83] [87] Polymerization can be done in bulk (by dissolving the cluster in the organic monomer) or in solution polymerization, where both cluster and monomer are dissolved in a suitable solvent. Films were prepared by dropping or casting the resin on a substrate and UV curing [77] or coating of alumina sheets by spin coating and subsequent UV curing. [88] Clusters bearing 2-bromo-2-methylpropionate ligands such as $Zr_5O_4(OOC(CH_3)_2CBr)_{10}(OPr)_2$, $Ti_6O_4(OOC(CH_3)_2CBr)_8(O^iPr)_8$ or $V_3O_3(OOC(CH_3)_2CBr)_6$ were subjected to atom transfer radical polymerization (ATRP). [27] Thereby the cluster acts as initiator, and polymerization starts from the bromo‑substituted ligand, leading to hybrid core‑shell type nanoparticles. Clusters of the type $Zr_4O_4(OH)_4(exo$-OOC-Norb)$_{12}$, $Zr_4O_4(OH)_4(endo$-OOC-Norb)$_{12}$ and $Ti_6O_4(OPr)_8(endo,exo$-OOC-Norb)$_8$ were incorporated in polymers by ring‑opening metathesis polymerization (ROMP). [89] [83] The clusters $[Zr_6O_4(OH)_4(OOCCH_2CH_2SH)_{12}]_2$ and $[Hf_6O_4(OH)_4(OOCCH_2CH_2SH)_{12}]_2$ were polymerized through thiol‑ene polymerization and it was shown that the clusters are covalently incorporated in the polymer. [34] Microcellular polystyrene foams were obtained by emulsion polymerization of the cluster $Ti_4(O^iPr)_4(OCH_2CH=CHCH_2O)_4$. [90]

An interesting approach to obtain silica matrices with homogeneously dispersed metal oxide particles is the polymerisation of metal oxo clusters in presence of a polymerizable siloxane. [91] First, a sol was produced by hydrolysing (methacryloxymethyl)triethoxy‑silane. The cluster was dissolved in a suitable solvent and mixed with the sol which was then subjected to free radical polymerization. In this way the clusters $Zr_4O_2(OMc)_{12}$ and $Hf_4O_2(OMc)_{12}$ were embedded in the siloxane network and binary oxides were obtained after polymerization. [92] [93]

A different approach to incorporate NBBs in organic matrices takes advantage of ligand exchange reactions. It has been reported that some Ti oxo alkoxo clusters are stable towards transalcoholysis reactions or towards exchange of the alkoxo groups with low molecular weight alcohols. [94] [95] [96] Initially unfunctionalized clusters (e.g. $Ti_{12}O_{16}(O^iPr)$ or $Ti_{16}O_{16}(OEt)_{32}$)

can be incorporated in organic matrices by alkoxo exchange with polymerizable alcohols and subsequent polymerization [97] or can be crosslinked by *in situ* ligand exchange in the presence of polyols or hydroxy functionalized dendrimers. [98] [99] [100]

Besides ligand exchange reactions on preformed clusters, modification reactions are a possible way for covalent linkage to an organic phase through click chemistry. Although hybrid materials were not fabricated by this approach, it was shown that the alkyne functions of the clusters $Ti_6O_4(OPr)_8(OOC(CH_2)_2C\equiv CH)_8$ and $[Zr_6O_4(OH)_4(OOC(CH_2)_2C\equiv CH)_{12}]_2$ are available for alkyne-azide reactions. [101] This would make possible to "click" clusters on preformed polymers bearing azide functionalities on their polymer backbone.

It was shown in numerous cases that clusters stay intact upon polymerization. This was evidenced by different characterization techniques, such as extended X-ray absorption spectroscopy (EXAFS,) [34] [92] ^{17}O NMR spectroscopy [97] [99] and ^{13}C MAS NMR spectroscopy. [85] X-ray photoelectron spectroscopy (XPS), small angle X-ray scattering (SAXS) and transmission electron microscopy (TEM) were used in some cases to show that the clusters can be homogeneously incorporated in the organic matrix and do not suffer from aggregation. [75] [77] [74] [85] [77] [89] [86] [87]

Chapter 2

Aim of the work

Aim of the work

In this work different ligand exchange reactions were investigated with the aim to find protocols which lead to clusters with an exact predetermined stoichiometry of the ligand sphere but under retention of the original cluster core.

This task brings up several questions, such as: Are there differences between the ligand binding energies with respect to their position on the cluster and with respect to steric and electronic effects of the ligands? Is it possible to exchange all carboxylate ligands under retention of the cluster core? Do steric and electronic effects have an influence on the equilibrium reaction? Do clusters undergo scrambling reactions? How does a modified ligand shell influence properties of the hybrid material?

DFT calculations are one approach to investigate ligand binding energies. A method for performing the calculations can be selected after careful evaluation of different basis sets and DFT functionals. Once a suitable method is selected, ligand binding energies on different positions on the cluster and ligand binding energies of different types of ligands can be calculated.

For some clusters reported in the literature, ligand exchange was shown to proceed under retention of the cluster core, however degradation of the cluster was also reported. Therefore, this question must be answered for each system independently.

Retention of the cluster core can be verified by single crystal XRD or, in cases where crystal structures are difficult to access, by two-dimensional NMR spectroscopy. Reports on steric effects of the ligand exchange reaction are scarce. Once it was shown that ligand exchange on a particular cluster proceeds with retention of the cluster core, steric effects can easily be investigated by exchange reactions with different sterically demanding ligands and by analysing the stoichiometry of the ligand sphere after the exchange reaction. Scrambling reactions between clusters with the same cluster core but different ligands are easy-to-perform reactions and are characterized by high yields. Furthermore, no purification steps are needed. Therefore they are an attractive method to prepare mixed ligand clusters. However, scrambling reactions of

transition metal oxo clusters were not investigated before. Considering scrambling reactions it is important to show that the cluster core is retained during the reaction and that both types of ligands are coordinated to the same cluster core. Both questions can be answered by detailed investigation with two-dimensional NMR spectroscopy.

There is a special interest in site-selective ligand exchange. One possible approach is to exploit differences in the ligand binding energies at different positions on the cluster which are big enough so that more weakly bonded ligand exchange first. A second approach is the selective exchange of only chelating or bridging ligands. While differences in the ligand binding energies can be investigated by means of DFT calculations, NMR spectroscopy and single crystal XRD can give information about site-selective ligand exchange in experiment.

Once a way is found to exactly predetermine the number of polymerizable and non-polymerizable ligands on the cluster surface after exchange experiments, clusters with different crosslinking ability can be obtained. Hybrid materials with altered materials properties, compared to the pristine polymer, can be obtained upon polymerization. This change of materials properties stems from the crosslinking density of the polymer (crosslinking effect) but also from the presence of the inorganic moiety in the organic polymer (filler effect). Separation of crosslinking and filler effects can be done by employing clusters of the same type but with a different number of polymerizable ligands. Thus the question is, how materials properties are influenced when going from a fully functionalized cluster to a fully non-functionalized cluster.

Ligand exchange does not only allow to adjust the number of functional and non-functional ligands on the cluster surface, but also to introduce a second functionality. This second functionality potentially remains active for further chemical reactions after polymerization, provided that it does not participate in the polymerization reaction. This concept was investigated with a mixed mercapto/methacrylate cluster. The question in this experiment was whether it is possible to introduce a nucleophilic functionality in the cluster and whether the functionality remains active after the polymerization step.

Chapter 3

Theoretical Considerations of Ligand Exchange Reactions

Theoretical Considerations of Ligand Exchange Reactions

3.1 Introduction

A variety of transition metal oxo clusters were reported during the last decades and their use as NBB in materials synthesis was shown on numerous examples. Ligand exchange reactions allowed to control the composition of the ligand sphere and showed influence on the hybrid materials' properties. However, a detailed report on mechanistic aspects of ligand exchange processes, on the ligand binding energy or on differences on ligand binding energies for different ligand systems is lacking. This topic can be treated by investigation of the electronic structure by means of theoretical calculations.

From the viewpoint of computational chemistry, transition metal oxo clusters are rather large species. Thus, highly accurate models, such as coupled cluster (CC) or configuration interaction (CI) calculations are not easily accessible due to the large computational costs. Density functional theory (DFT) on the other hand is known to accurately predict the geometry, the vibrational modes or binding energies at a lower computational cost. This advantage is specially true for transition metal-related problems where electron correlation must be accounted for.

Electron correlation can be divided in two parts: dynamic electron correlation and non-dynamic or near degeneracy electron correlation. Dynamic correlation stems from the fact that electrons avoid each other to reduce repulsion. This electron correlation is a short range phenomenon and is present in every system which contains at least two electrons. Medium or long range correlation effects are more system specific and need to be accounted for in highly accurate calculations. In the case of transition metal chemistry nearly degenerated electronic states are often found in the ground state and the electron distribution over the molecule can be rather large. This fact makes it difficult to treat transition metal related problems with wave function-based (WFT) methods. DFT, however, remains a simple concept and produces fairly accurate results.

Modern computational chemistry programs have a large library of density functionals. These functionals differ in their way how the exchange‑correlation term is treated, and the accuracy of the results depends - not only, but also - on the complexity of the underlying theory. At the same time the computational costs increase with increasing complexity. It is important to mention that, although the DFT framework is in theory exact, the exact description of the exchange‑correlation term is not known. Different DFT functional types were therefore developed in the past, which differ in their way how the exchange‑correlation term is approximated.

The oldest approximation of DFT functionals is based on the Dirac-Slater approximation to the exchange energy of the uniform electron gas (UEG). This approximation was reformulated in terms of Kohn-Sham theory and is called local density approximation (LDA). LDA functionals depend solely on the spin densities and are an effective but imprecise approximation for the exchange term. The next generation of functionals adds a dependence on the gradients of the spin densities. This functionals are called generalized gradient (first derivative of the density) approximation (GGA) functionals and are computationally more expensive than the LDA functionals. Both the LDA and GGA functional include self-exchange and self-correlation effects, i.e. the situation where an electron interacts with itself, which is incorrect. In practice, underestimated HOMO‑LUMO gaps and underestimated bond lengths are commonly observed. Self-exchange, however, can be partially eliminated by including a Hartree Fock (HF) exchange term while self-correlation can be eliminated by including kinetic energy density dependent term. Functionals which include a certain amount of HF exchange are called hybrid functionals and are the work horse in main group chemistry. Functionals which include the second derivative of the density are called meta-GGA functionals and overcome the shortage of the self-correlation.

A further simplification applied in this work addresses the basis set size. While full electron calculations are state‑of‑the‑art for small molecules and elements up to the third period, heavy elements are often treated by describing the inner core electrons with one single function, while the valence electrons, which are most relevant in chemistry, are described by a full electron basis set. This simplification, which is referred to as effective core potential (ECP), is justified since inner closed shell electrons do not participate in bonding. On the other hand, treating a larger number of electrons by one function is an effective way to reduce computational cost.

Reports on the electronic structure of diamagnetic, ligand‑capped transition metal oxo clusters, especially of Ti, Zr and Hf oxo clusters, are scarce. The ligand dynamics on the surface of the cluster $Zr_6O_4(OMc)_{12}$ was previously described in a molecular dynamics study.[62]. The change in the band gap of the cluster $Ti_{17}O_{24}(O^iPr)_{20}$ upon ligand exchange with chromophores was

reported. [52] Calculations on polyoxometalates were performed to obtain information on the rate and mechanism of exchange reactions. [102] [103] Furthermore, calculation of the stability of metal organic frameworks (MOF) upon change of the linker molecules were reported recently.[104] However, these calculations employed DFT in the framework of plane wave approaches. Gaussian type orbitals (GTO) based DFT calculations on clusters were only reported for smaller systems, such as ligand exchange on Zn alkoxo clusters [105] or catalytic reactions on the surface of gas phase MO_2 clusters. [106] [107] [108]

In the following, a detailed assessment on the performance of different DFT functionals on the accurate description of the geometry and vibrational modes of the cluster $Zr_4O_2(OMc)_{12}$ will be given. The ligand binding energies on different positions of the cluster and electronic effects of the ligand substituent on the binding energy will be discussed, as well as the change in ligand binding energies for different ligand types.

3.2 Computational Details

All calculations were performed using the Gaussian09 [109] software package. The molecular structure of $Zr_4O_2(OMc)_{12}$ (CCDC 137083) served as initial structure in all geometry optimizations. Thus, it was not attempted to find the global minimum of the structure; a realistic system, which is confirmed by experimental results, was modelled instead. No symmetry or geometry restrictions were applied in the geometry optimizations. Harmonic vibrations (unscaled) of all species were calculated at the same level as the corresponding geometry. Stationary points were characterized as minimum structures with all frequencies real. To assess the performance of DFT methods with respect to an accurate description of geometrical and vibrational parameters, several types of functionals were considered, representing different types of exchange - correlation treatments. It was shown before that pure generalized gradient approximated functionals (GGA) and hybrid functionals tend to overestimate bond lengths, while local density approximated functionals (LDA) typically produce closer or slightly underestimated bond lengths.[110] [111] [112] Each type of functional is included in this study. LDA is represented by the local - exchange - only functional $X\alpha$ [113] [114] [115] (α=0.7) and the local exchange correlation functional SVWN5. [113] [114] [115] [116] GGA functionals are represented by the OLYP [117] [118] [119] [120] and PBE [121] [122] functionals. The PBE functional was used for calculations on transition metal oxo clusters before. [62] The range of hybrid functionals is covered by the very successful PBE0 form [121] [122] [123] (25 % HF exchange), the one - parameter hybrid functional mPW1PW91 [124] (25 % HF exchange) and the well-known three - parameter hybrid functional B3LYP [125] (20 % HF exchange). TPSS [126] was chosen to represent the family of kinetic-energy density-dependent functionals (meta - GGA) and showed good performance for ligand binding energies in transition metal complexes and clusters before. [127] The CAM - B3LYP functional [128] (20–65 % HF exchange) which behaves as a typical hybrid functional at short ranges but which adds up to 65 % HF exchange at long ranges, was chosen to represent the family of long range corrected functionals.

Different Gaussian type orbital basis sets (GTO) were used throughout the calculations. The LANL2DZ [129] [130] basis set of double–ζ quality with the corresponding relativistically corrected effective core potential (ECP) [131] was used for the Zr atoms. The lighter elements (*viz.* H, C, O, F) were treated with the D95V double–ζ quality basis set. [132] The polarized Def2SVP [133] basis set and the corresponding ECP [134] was used similarly to describe the Zr atoms in combination with the D95V basis set for the light elements. In addition the triple–ζ quality SDD [135] [136] [137] basis set in combination with the more flexible Stuttgart - Dresden

ECP for the Zr atoms and the D95V and the triple–ζ quality full-electron TZVP basis set from Ahlrichs [138] with polarization functions for the light elements was used. In the remainder of the work the basis sets will be denoted according to the form SDD|TZVP which means SDD ECP with corresponding basis set for Zr and TZVP for the light atoms. To test basis set size-dependent effects on the structure optimization and the calculation of vibrational modes, the LANL2TZ [131] triple–ζ basis set with the corresponding ECP [139] for Zr as well as the triple–ζ basis set with polarization function Def2TZVP [133] and the corresponding ECP[134] for Zr was combined with the full electron triple–ζ TZVP basis set for the light elements. The ligand binding energy was calculated as the difference between the total energy of the optimized cluster and the total energies of the optimized cluster without the respective ligand and the free ligand. Basis set superposition error (BSSE) effects were accounted for by the counterpoise method (CP) [140] [141], as implemented in Gaussian09. All reported energies are relative energies and BSSE and zero-point energy (ZPE) corrected, unless otherwise noted. Relativistic effects were accounted for by using relativistically corrected ECPs.

3.3 Results and Discussion

The structure of the cluster $Zr_4O_2(OMc)_{12}$ was determined by single crystal XRD before. It consists of four Zr(IV) atoms arranged in a plane, in which three atoms each are connected through μ_3-oxo bridges and build a $[Zr_3O]$ triangle (Fig. 3.1(a)). The two opposed Zr atoms Zr1 and Zr1' are substituted by one chelating methacrylate ligand each while the remaining ten methacrylate ligands are bridging. Five of the bridging ligands connect the Zr atoms of each $[Zr_3O]$ triangle. The cluster $Zr_4O_2(OMc)_{12}$ exists as two isomers which differ in the coordination mode of one bridging ligand. The crystallographic symmetry of the symmetric cluster **Zr4** (Fig. 3.1 (a)) is C_i. In the asymmetric structure (**Zr4_as** Fig. 3.1 (b)) one ligand bridging Zr1 and Zr2 (or Zr1' and Zr2' respectively) takes a chelating-bridging (μ_2, η^2) coordination mode and the symmetry of the structure is reduced to C_1. Experimental results showed previously, that the change of the coordination mode of one ligand is due to packing effects and that the clusters **Zr4** and **Zr4_as** interconvert through a dynamic behavior of the ligands in solution. [62] This dynamic behavior includes an interchange of bridging and chelating ligands. All calculations were performed on the symmetric structure **Zr4**. It is important to note that geometry optimizations usually take many steps to converge since the multidimensional potential energy surface is very shallow. Nevertheless, all geometry optimizations converged to similar structures although symmetry restrictions were not applied during the optimization process. The obtained minimum structures are all akin to the symmetric starting geometry of **Zr4** and retain the C_i symmetry during the optimization process.
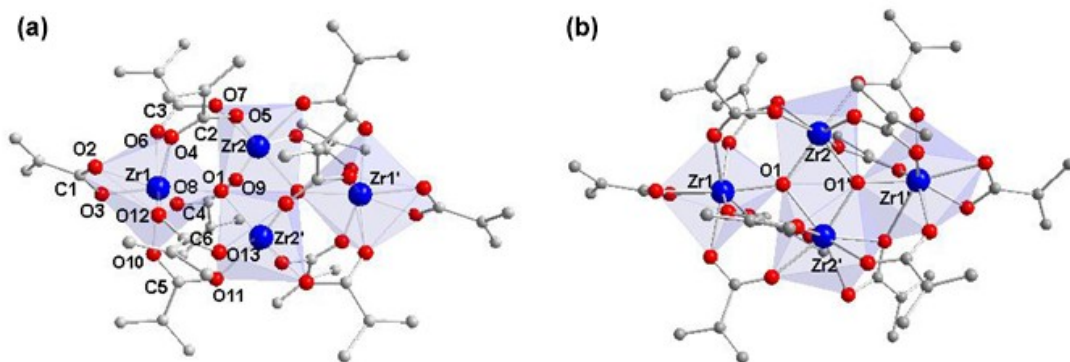

Figure 3.1: Molecular structure of **Zr4** and **Zr4_as**.

An assessment of different DFT methods to accurately reproduce the experimental geometry will first be discussed. It is based on the mean average error (MAE) of the most important bond lengths which includes the bonds between the Zr atoms and the μ_3-O ligands in the cluster core

(Zr-μO), the bond lengths between Zr1 and the oxygen atoms of the chelating ligand (Zr-O$_c$) and the bond lengths between the Zr atoms and the oxygen atoms of the bridging ligands (Zr-O$_b$) with respect to the experimental structure. In addition the root mean square deviation (RMS) with respect to the experimental structure of all these bond lengths is used in the assessment.

Basis set effect on cluster geometries: Several basis sets were used in this study, differing in their basis set size and in their flexibility. The ECPs Def2SVP, LANL2DZ and SDD were combined with the double–ζ D95V basis set for light elements and were compared with a series employing the bigger Def2TZVP, LANL2TZ and SDD ECPs in combination with the triple–ζ basis set TZVP. For all bond types (Zr-μO, the Zr‑O bonds of the chelating carboxylates Zr-O$_c$ and the Zr‑O bonds of the bridging carboxylates Zr-O$_b$) considered in this study an increase of basis set size from double–ζ to triple–ζ quality gives an improvement in accuracy, which is reflected in smaller MAE and RMS values. This basis set size effect seems to be in general less pronounced for the Zr-μO bond lengths than for the Zr‑ligand bond lengths. While in the small basis set series all applied ECPs (Def2SVP, LANL2DZ and SDD) showed the same poor behavior, a trend with respect to the applied Zr basis set can be seen in the big basis set series (Def2TZVP, LANL2TZ, SDD). The accuracy increased when going from the least flexible LANL2TZ via SDD to the polarized Def2TZVP basis set. Interestingly, the improvement in accuracy upon increase of the flexibility of the basis set is not independent on the applied functional. While LDA functionals Xα and SVWN5 and the GGA functionals OLYP and PBE in combination with a small basis set consistently failed to reproduce bond lengths with adequate accuracy, the hybrid functionals mPW1PW91, B3LYP and CAM‑B3LYP and the meta‑GGA functional TPSS combined with a small basis set failed to reproduce the Zr-μO and Zr-O$_c$ bond lengths but reproduced Zr-O$_b$ bond lengths with high accuracy, even in combination with the small basis set. Overall, analysing the MAE values of the particular bond types showed clearly that application of the bigger basis sets gives more balanced results. Our results are in agreement with previous reports on transition metal clusters which propose polarization functions and basis sets of at least triple–ζ quality to accurately model cluster‑ligand bond lengths. [142] In the following only results from the big basis set series will be discussed.
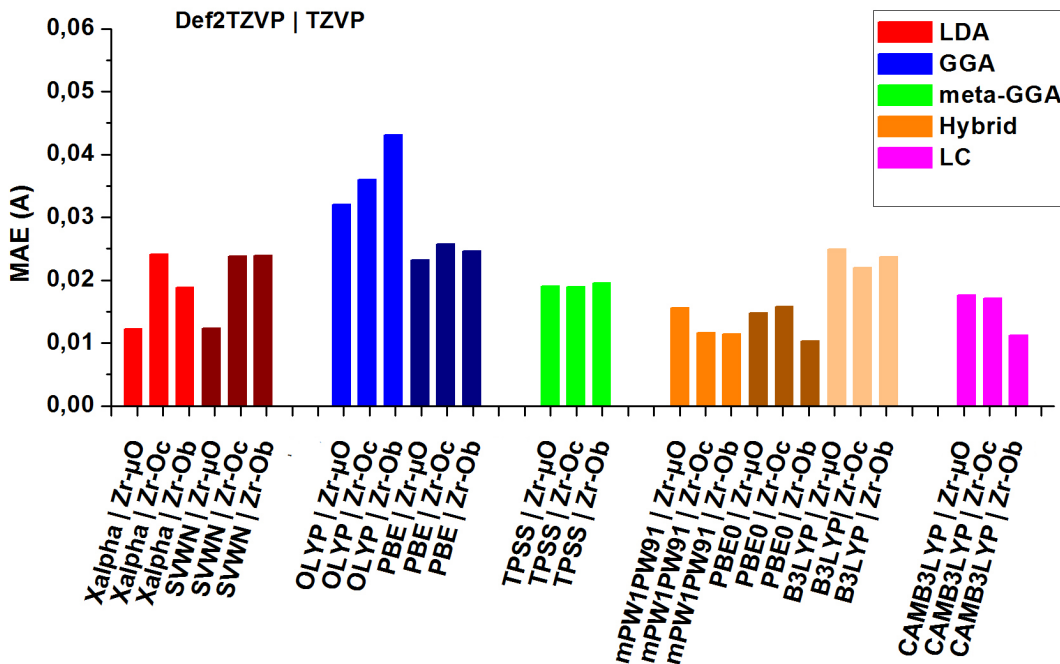
Figure 3.2: MAE values dependence on the functional for the Def2TZVP | TZVP basis set.
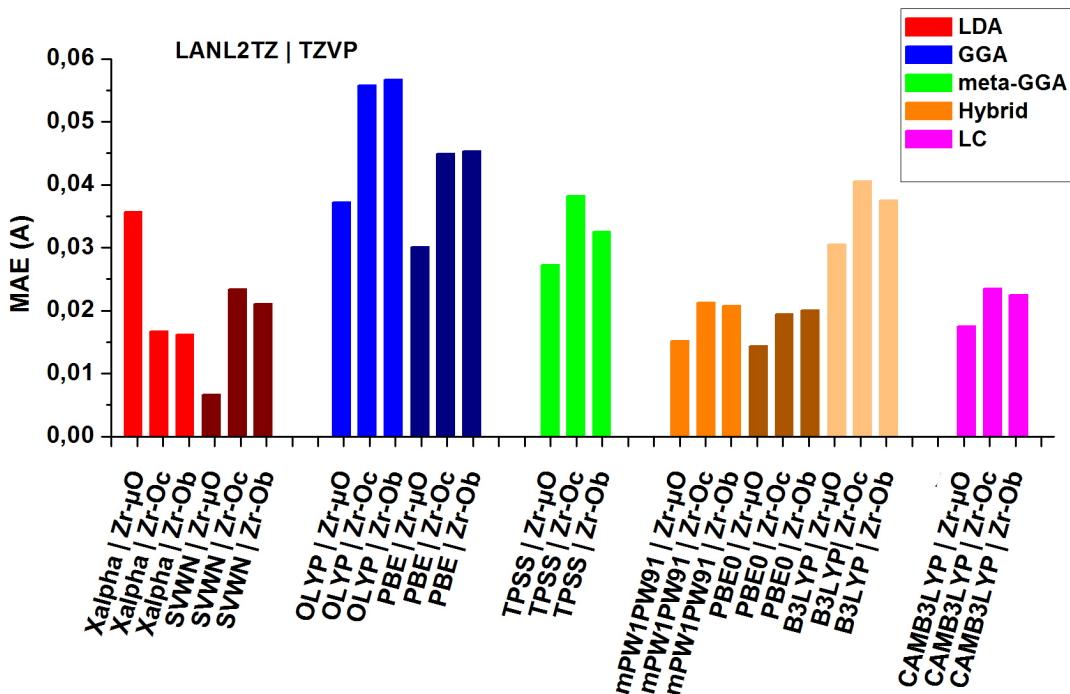

Figure 3.3: MAE values dependence on the functional for the LANL2TZ | TZVP basis set.
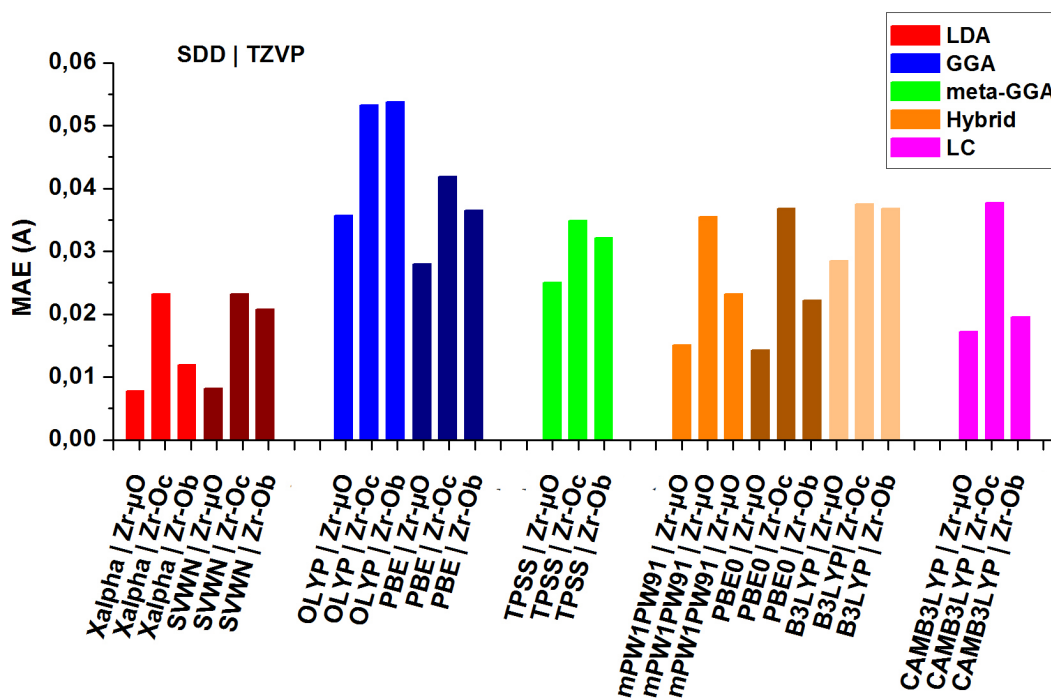
Figure 3.4: MAE values dependence on the functional for the SDD | TZVP basis set.
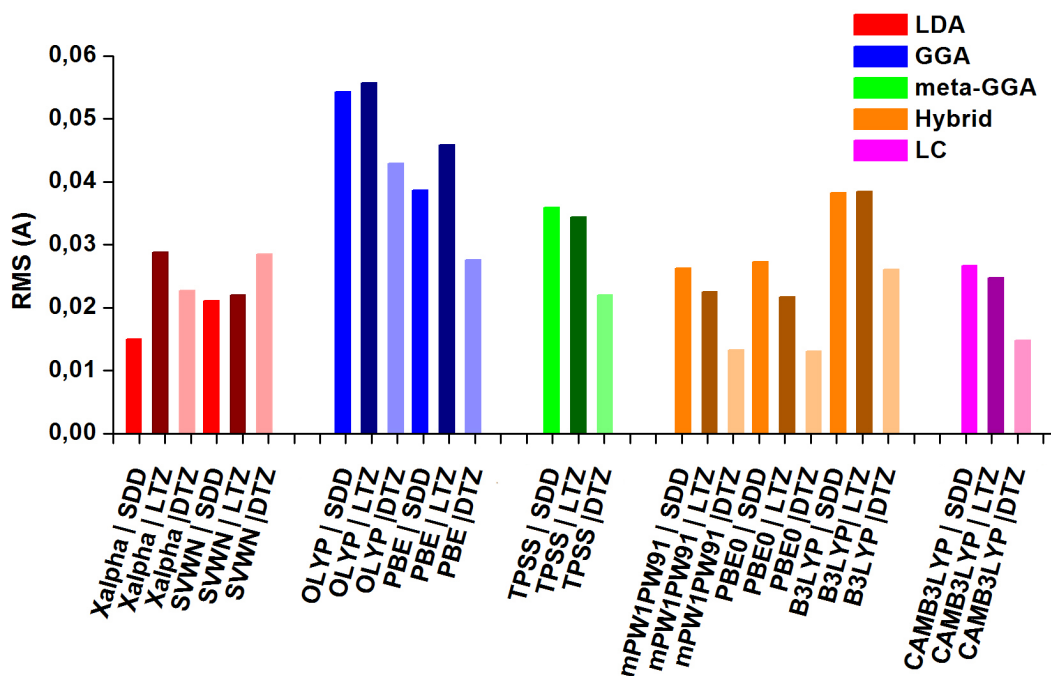

Figure 3.5: RMS values for all optimized structures using the triple–ζ basis set

Functional effect on cluster geometries: It was previously reported that pure GGA and hybrid functionals tend to overestimate bond lengths and that LDA functionals slightly under-estimate bond lengths but produce overall a better estimation. The results presented here fully reproduced this trend. [142] [143] [144] Bond lengths decreased in the order GGA > meta‑GGA ≈ Hybrid > LDA with the tendency of LDA functionals to underestimate the bond lengths with respect to the experimental results. The functionals were compared according to their MAE and RMS values for the three basis set combinations Def2TZVP|TZVP, LANL2TZ|TZVP and SDD|TZVP and are shown in Fig. 3.2 - Fig. 3.5. Structural results were particularly good with the LDA functionals, the hybrid functionals PBE0 and mPW1PW91 and the long range cor-rected functional CAM‑B3LYP throughout this series. The pure GGA functionals, especially the OLYP functional, gave the worst results with RMS values exceeding 0.04 Å. Especially the metal-ligand bond lengths were described with low accuracy by this functional family. In general, the hybrid functionals appear superior to any other functional family by comparing MAE values, with B3LYP being the only exception. However, including long range correction improved the results significantly. Thus, including HF exchange seems to be of uttermost importance towards obtaining accurate geometries. The meta‑GGA TPSS showed a balanced performance with respect to the different bonding situations in the cluster (*viz.* $Zr–\mu O$, $Zr–O_b$ and $Zr–O_c$) but dropped behind the hybrid functionals in terms of accuracy. This trend was found throughout all basis set combinations. However, the magnitude of error was smallest for the combination Def2TZVP|TZVP. The methods mPW1PW91 and PBE0 in combination with Def2TZVP| TZVP therefore gave the best RMS values with ≈ 0.01 Å. All RMS and MEA values and experimental values are shown in Tab. A.1 - A.8 at page XXIV in the appendix.

Functional effect on vibrational modes: Vibrational modes were calculated for all minimum structures. A comparison of the results obtained from the big basis set combination with the experimental ATR spectrum will be given in the following. The MAE values for the calculated frequencies are shown in Fig. 3.6. LDA, GGA and meta‑GGA functionals produced results with the smallest deviation from the experiment, as can be seen by the low MEA values which lie in the range of $20\,\mathrm{cm}^{-1}$ and $40\,\mathrm{cm}^{-1}$. Mixing with exact exchange increased the deviation, thus the hybrid functionals show relatively high MAE values of $> 60\,\mathrm{cm}^{-1}$. One interesting point should be mentioned here: Increasing the amount of exchange did not improve the accuracy. Both mPW1PW91 (25 % exchange) and PBE0 (25 % exchange) gave worse results than B3LYP (20 % exchange). The long‑range corrected functional CAM‑B3LYP performed equally bad as the mPW1PW91 and PBE0 functional.

Remarkably, the accuracy of the results depended solely on the functional used. Change of the basis set by keeping the same functional gave almost the same result with a maximum fluctuation of $5\,\mathrm{cm}^{-1}$ in the MIR and $30\,\mathrm{cm}^{-1}$ in the FIR region.

For a detailed analysis, the most pronounced vibrational modes were selected for comparison with experimental values. The selected vibrational modes include the asymmetric stretching vibration of CH_3 ($\nu_{\mathrm{exptl}} = 2978\,\mathrm{cm}^{-1}$), the symmetric CH_3 stretching vibration ($\nu_{\mathrm{exptl}} = 2926\,\mathrm{cm}^{-1}$), the asymmetric stretching vibration of the bridging carboxylates ($\nu_{\mathrm{exptl}} = 1582\,\mathrm{cm}^{-1}$, $1559\,\mathrm{cm}^{-1}$ and $569\,\mathrm{cm}^{-1}$), the symmetric stretching vibration of the bridging carboxylates ($\nu_{\mathrm{exptl}} = 1419\,\mathrm{cm}^{-1}$, $1371\,\mathrm{cm}^{-1}$ and $601\,\mathrm{cm}^{-1}$) and the asymmetric ($\nu_{\mathrm{exptl}} = 1559\,\mathrm{cm}^{-1}$) and symmetric ($\nu_{\mathrm{exptl}} = 1459\,\mathrm{cm}^{-1}$) stretching vibration of the chelating carboxylates. Furthermore the asymmetric deformation vibration of the $[Zr_4O_2]$ core ($\nu_{\mathrm{exptl}} = 292\,\mathrm{cm}^{-1}$) and the symmetric deformation vibration of the $[Zr_4O_2]$ core ($\nu_{\mathrm{exptl}} = 520\,\mathrm{cm}^{-1}$ and $247\,\mathrm{cm}^{-1}$) were considered.

While the vibrational modes in the MIR region, which includes the carboxylate and methyl vibrations, were described with sufficient accuracy by all functionals (LDA and GGA show approximately 1–5 % deviation, hybrid functionals show approximately 5–10 % deviation), the $[Zr_4O_2]$ core deformation vibrations, mostly the asymmetric $[Zr_3\text{-}\mu O]$ vibration, tends to be poorly reproduced by the hybrid functionals in combination with the Def2TZVP basis set. mPW1PW91 and PBE0 both described the asymmetric deformation vibration of the $[Zr_4O_2]$ core with an error of 30 %, while the error in case of CAM‑B3LYP was 53 %. Overall, the choice of functional seems to be the most critical factor in correctly reproducing the vibrational modes. RMS values of the calculated vibrations are shown in Tab. A.9 on page 40 in the appendix. Experimental IR bands are shown in Tab. 4.1 in chapter 4.
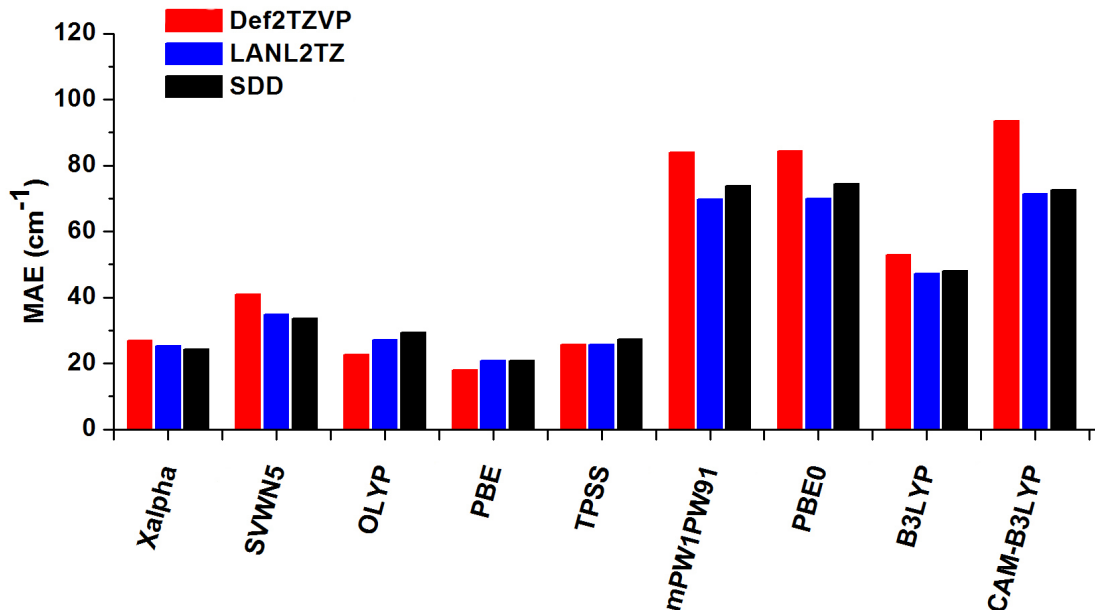
Figure 3.6: MAE values of the vibrational modes depending on the different functionals within the big basis set series.

Effect of Exchange‑Correlation functional on the HOMO‑LUMO energy: It is known that HOMO‑LUMO energies are very sensitive to the applied functional. LDA for example tends to underestimate band gap energies, while including exact exchange in form of hybrid functionals tends to overestimate band gap values.[145] The HOMO‑LUMO splitting in dependence of the functional is shown in Fig. 3.7. Our results follow the trend of previous reports, with LDA energies being the lowest, while including HF exchange increases the HOMO‑LUMO splitting energy up to unrealistic high values. The values obtained with the GGA functionals (3.4–3.7 eV) were within the range of HOMO‑LUMO energies which were reported for a similar system before.[62] [146] Applying different basis sets of one type, e.g. different basis sets of triple–ζ quality, had no impact on the HOMO‑LUMO splitting energy. Thus, within one basis set series the magnitude of the HOMO‑LUMO energy depended solely on the choice of the functional. Going from the triple–ζ to the double–ζ basis set shifted the HOMO‑LUMO gap towards lower energy to an extent of 0.2–0.3 eV. HOMO‑LUMO energies are shown in Tab. A.10 on page XXIV in the appendix.

Effect of basis set on the ligand binding energy: The dependence of ligand binding energies on the different basis set types and on the functionals are shown in Fig. 3.8. Variations from Def2TZVP to SDD or LANL2TZ were small and within the range of 50 kcal/mol. LANL2TZ predicts the highest binding energy. Going from LANL2TZ to the more flexible SDD
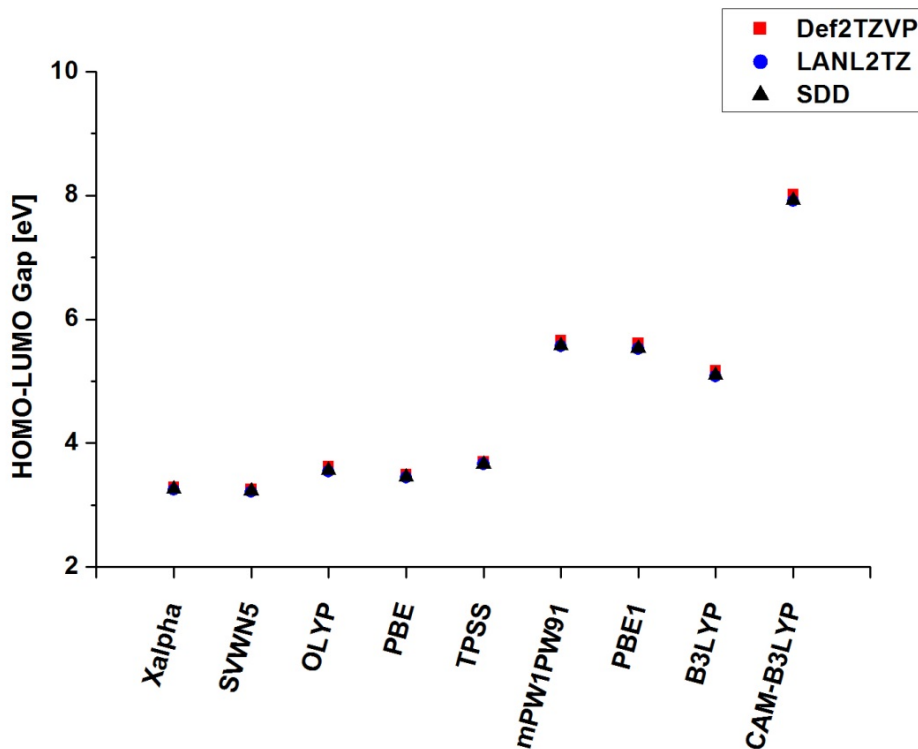
Figure 3.7: Dependence of HOMO‑LUMO splitting energies on the different functionals for the big basis set series.

basis set increased the binding energy insignificantly by $\approx 0.2\,\mathrm{kcal/mol}$. Including augmentation (Def2TZVP) increased the energy further by approximately $1.3\,\mathrm{kcal/mol}$. In total, the ligand binding energy was not very sensitive to changing the Zr basis set and ECPs.

The effect of CP correction was rather small, thus including CP decreased the binding energy by approximately $5\,\mathrm{kcal/mol}$.

Effect of functionals on the ligand binding energy: A functional dependency of the ligand binding energies is much more pronounced. The LDA functionals clearly predicted the strongest bonding between the ligands and the cluster. This is somehow expected, since a known drawback of LDA is to overestimate ligand binding energies.[142] GGA functionals and meta‑GGA functionals decrease the ligand binding energy, with the GGA functional OLYP predicting the weakest bonding. Increasing the amount of HF exchange in the hybrid functionals resulted in an increase of the ligand bond strength. Thereby the CAM‑B3LYP functional predicts ligand binding energies which are close to the values obtained for the LDA functionals. All ligand binding energies are shown in Tab.A.11 on page XXIV in the appendix.

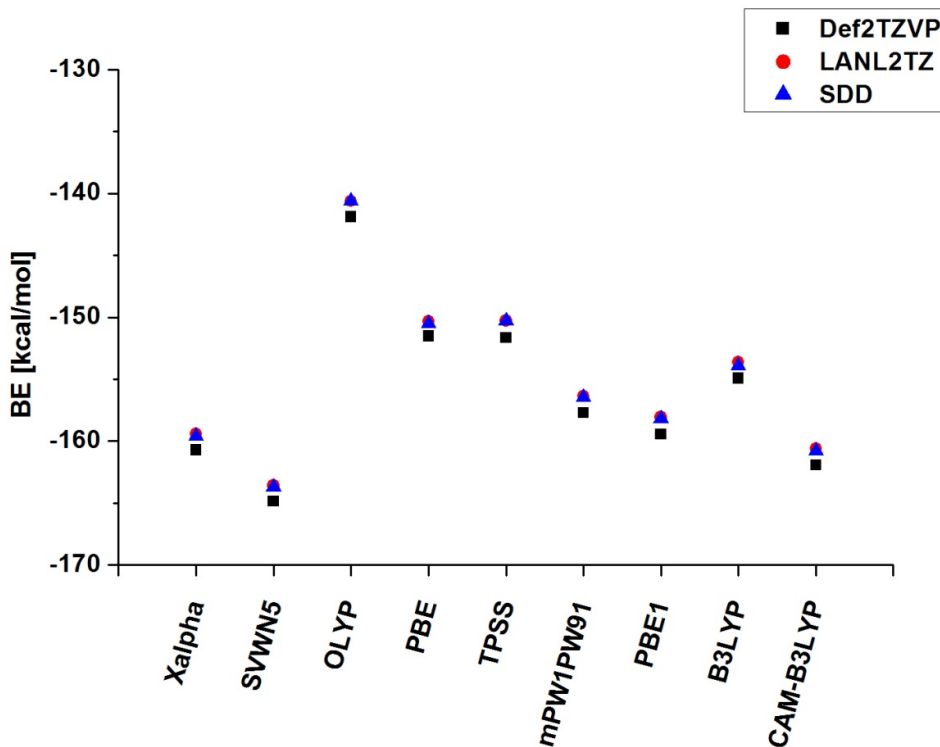**Figure 3.8:** Dependence of the ligand binding energy [kcal/mol] on the functional.

Dependence of ligand binding interaction on ligand placement and type of ligand:
The dependence of the ligand bond strength on the ligand position in the cluster and of differ-
ent ligand types was additionally investigated. The assessment of the functionals and basis sets
showed that the meta - GGA functional TPSS in combination with the Def2TZVP basis set and
corresponding ECP for the Zr atoms and the TZVP basis set for the light atoms showed a bal-
anced performance towards accurate prediction of geometries, vibrational frequencies and binding
energies. Therefore, all following results were obtained by the method TPSS Def2TZVP|TZVP.
CP correction showed only minor effects on the ligand binding energies but increased the compu-
tation time. CP corrections were therefore omitted in the following calculations. The aim of this
study was to model trends in ligand binding energies, rather than obtaining high level accurate
results.

In the first series one methacrylate ligand was replaced with an acetate ligand and the six unique
positions were varied. Position 1 corresponds to the chelating ligand (see Fig. 3.1 (a)). Position
2 - Position 6 corresponds to the chelating ligands in following order (the carboxy oxygen and
carbon atoms are labeled as in Fig. 3.1 (a)): Pos.2: O4-C2-O5; Pos. 3: O6-C3-O7; Pos. 4:
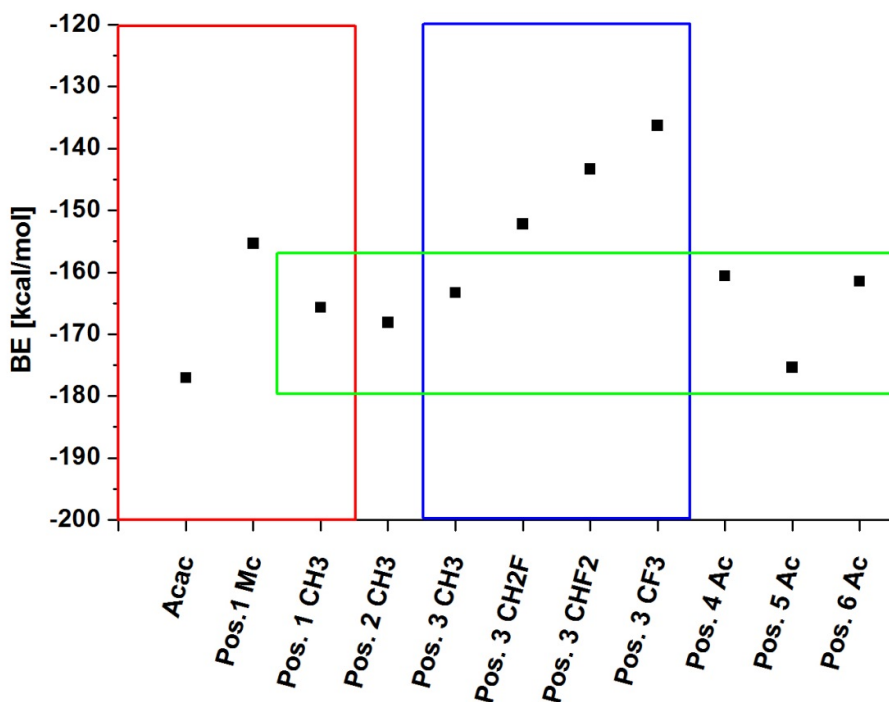O8-C4-O9; Pos. 5: O10-C5-O11; Pos. 6: O12-C6-O13. This series is marked with a green square

Figure 3.9: Ligand binding energies [kcal/mol] of the acetate ligand (Ac) at different positions on the cluster and of different ligand types.

in Fig. 3.9. Furthermore, the effect of electron‑pulling substituents was tested for the ligand in position 3. Thereby the H atoms of the acetate ligand were successively replaced by F atoms (this series is marked with a blue square in Fig. 3.9). The difference in binding energy between the chelating methacrylate ligand, the chelating acetate ligand and the chelating acetylacetonate ligand were additionally considered (red square in Fig. 3.9).

Depending on the position, the binding energy for the acetate ligand lies between -160 kcal/mol and -175 kcal/mol with the ligand in position 5 showing the strongest binding energy. There is no correlation between the predicted bond lengths or angles and the binding energy for the ligand at different positions. It seems very likely that the ligand binding energy does not solely depend on the binding geometry of the specific ligand on the cluster, but also on the environment by the other ligands. The difference between the strongest and weakest binding energy is relatively low at approximately 15 kcal/mol. Thus, upon ligand exchange reactions with carboxylic acids, all positions are equally accessible. For comparison, the activation barrier between the chelating-bridging interchange of the ligand dynamics was predicted previously to be of the magnitude of 17.5 kcal/mol. [62]

Introducing electron withdrawing groups in the ligand decreases the binding energy due to a -I effect. This is seen clearly in the series $CH_3 > CH_2F > CHF_2 > CF_3$ and a correlating decrease of the binding energy. Going from CH_3 to CH_2F showed the biggest effect by a decrease of the binding energy of $11\,kcal/mol$. Further substitution resulted in a decrease of $9\,kcal/mol$, and going from CHF_2 to CF_3 decreased the binding energy by further $7\,kcal/mol$. This decrease of the binding energy correlated well with an increase of the Zr-O bond lengths of the carboxy group. By going from CH_3 to CF_3 the bond lengths between the two carboxylate O atoms and the Zr atom increased according to: $2.19/2.24\,Å(CH_3) < 2.21/2.26\,Å(CH_2F) < 2.23/2.29\,Å(CHF_2) < 2.25/2.30\,Å(CF_3)$.

In a last series different chelating ligands were investigated. Based on the results of the first series, a site-selective ligand exchange with carboxylates as incoming ligands seems unlikely. Site-selective exchange, however, might be possible when predominately chelating ligands such as acetylacetonate ligands are used as incoming ligand. Exchange of the methacrylate with the acetate ligand resulted in an increase of the bond interaction by $10\,kcal/mol$. Exchange of the chelating carboxylate ligands with acetylacetonate ligand resulted in further increase of the bond strength.

Both the carboxylate and the acetylacetonate ligands are chelating monoanionic bidentate ligands with a delocalized negative charge. However, they have different bite angles (O-Zr-O angle). While the carboxylate ligands form a four-membered ring upon chelation (bite angle for the acetate ligand is $56.9°$ and for the methacrylate ligand $57.0°$), acetylacetonate forms a six-membered ring and has a larger bite angle ($73.3°$). This widening of the bite angle contributes to a stronger ligand binding interaction. Binding energies for the different positions on the cluster and for the different ligand types are summarized in Tab. A.13 on page XXIV in the appendix.

3.4 Conclusions

In summary, different functionals in combination with basis sets of different size and flexibility were assessed with respect to accurate description of geometry parameters and vibrational modes. It was shown that geometry parameters are very sensitive to the basis set size and that at least a basis set of triple–ζ quality is needed to accurately model bond lengths of the structure. The quality of the modelled structure increased with the flexibility of the basis set describing the Zr atoms and the augmentation with polarization functions. Within one basis set type, the geometry parameters depended also on the functionals: LDA and GGA tend to give poor results and to underestimate ligand bond lengths. Going from GGA to meta‑GGA or hybrid functionals increased the accuracy. Thereby, increasing the amount of exact exchange showed improvement on the geometry.

For the modelling of the vibrational modes, LDA and GGA functionals showed in general a better performance than hybrid functionals. The latter ones tend to overestimate the vibrational modes by 5–10 %. While the LANL2TZ and Def2TZVP basis sets showed similar results, SDD failed to accurately predict the vibrational spectrum. The meta‑GGA TPSS showed balanced results which are of comparable quality with the LDA and GGA‑derived results throughout the different basis set types.

For the HOMO‑LUMO energies, LDA functionals tend to underestimate the band gap, whilst GGA functionals and the meta‑GGA functional predicted HOMO‑LUMO energies which are in good agreement with previous calculations on Ti and Zr oxo clusters.[62][146] Including HF exchange increased the HOMO‑LUMO energy and resulted in an unrealistic large energy gap for the long‑range corrected functional. This behavior of hybrid functionals to overestimate HOMO‑LUMO energies is in agreement with previous results.[142]

Ligand binding energies were calculated on one position of the cluster for the different functionals and basis sets. While change of the basis set did not show a big effect, the choice of the functional seemed to be important. LDA predicted binding energies which were much too low, while GGA functionals overestimated the binding energies. This is in agreement with previous findings. Including HF exchange lowered the binding energy and gave more reliable results than GGA or LDA. The meta‑GGA functional predicted the binding energies at the same magnitude as the hybrid functionals.

Analyzing the ligand binding energy on different positions of the cluster showed only small variations of approximately 15 kcal/mol in the binding energy. This difference between the

binding energies of the ligands at different positions did not correlate with the Zr-O bond length or the O-Zr-O angles. Thus the close environment of the individual ligands might affect the conformation of the ligand and therefore also the binding energy. This, however, was different when electron‑withdrawing substituents are present in the close proximity of the coordinating carboxy group. Going from CH_3 to CF_3 by successive exchange of the H atoms with F atoms in the acetate ligand, the ligand binding energy decreased. This can be traced back to a strong electron‑withdrawing effect of the F atoms. The Zr-O bond lengths increased at the same time.

Exchange of the chelating carboxylate ligand by acetylacetonate resulted in a widening of the bite angle and in an increase of the ligand bond strength. This increase of the binding energy was rather small, but favors the coordination of the acetylacetonate ligand instead of carboxylate ligands. This might allow site selective ligand exchange. On the other hand, exchange of carboxylate ligands with other carboxylates seems to proceed without any site‑selectivity. Differences in the binding energies on the different positions are too small and may result, also considering the dynamic behavior of the ligands, in a statistic exchange of carboxylates with respect to the coordination sites on the cluster.

Chapter 4

Ligand Exchange on Transition Metal Oxo Clusters

Ligand exchange on transition metal oxo clusters

4.1 Introduction

Functionalized transition metal oxo clusters can be incorporated in organic polymers to obtain inorganic‑organic hybrid materials. One common synthetic approach towards functionalized oxo clusters is a "one‑pot" synthetic strategy, where transition metal alkoxides are reacted with functional carboxylic acids leading to functionalized carboxylate‑capped oxo clusters. This bottom up pathway is easy and gives the clusters mostly in high yields. Only clusters bearing a high number of functional carboxylate ligands on the cluster surface are typically accessible through these protocols. Incorporation of such clusters in organic matrices leads to highly crosslinked polymers. Typical polymer properties (e.g. flexibility, mechanical strength) are determined by the crosslinking density. Incorporation of clusters in a polymer causes, beside crosslinking of the polymer, also so‑called filler effects, which stem from the presence of inorganic particles in the organic matrix. Filler effects and crosslinking go hand in hand in a sense that increasing the cluster loading to achieve higher crosslinking densities goes along with an increasing amount of inorganic filler. Crosslinking and filler effects, however, can be decoupled when the ratio of functionalized and non‑functionalized ligands on the cluster surface can be precisely controlled.

Three ways are reported to achieve control over the composition of the ligand sphere and therefore the amount of functionalities on the cluster surface [53] : (I) Reduction of the number of functional ligands can be achieved by using a mixture of functional and non‑functional ligands in the "one‑pot" synthesis of the clusters. This approach, however, lacks control over size and shape of the cluster and the exact composition of the ligand sphere. [54] (II) Ligand exchange reactions can be used to exchange the original ligands partly or completely. Ligand exchange reactions are equilibrium reactions and can be controlled by the amount of incoming ligand. This allows a

precise control over the composition of the ligand sphere. Nevertheless, ligand exchange reactions may be ambiguous, because rearrangement or degradation of the cluster can occur. Thus the intactness of the cluster core must be verified in each case after ligand exchange. Chances to perform ligand exchange reactions under retention of the cluster core are increased when charge and coordination number of incoming and leaving ligand is balanced. (III) Blocking of functional ligands by chemical reactions allows to decrease the number of functional ligands. However, this attempt was not successful before. [53]

Of those three methods ligand exchange reactions are the most versatile with respect to control the composition of the ligand sphere, and a short summary of the state of the art will be given in the following.

The Ti oxo alkoxo cluster $Ti_{16}O_{16}(OEt)_{32}$ appears to be extraordinarily robust towards transalkoholysis reactions. The reactivity of the cluster towards different alcohols ROH (R = Me, Pr, Bu, CH_2Ph, BuC_6H_{11}, Ph and Ph=CH_2) resulted in partial exchange of the ethoxy ligands with the incoming nucleophile under retention of the cluster core. [147] This was used in the preparation of 2-hydroxyethylmethacrylate (HEMA) - based hybrid materials. The cluster $Ti_{16}O_{16}(OEt)_{32}$ was dissolved in the HEMA monomer which resulted in exchange of eight ethoxy groups with HEMA. The solution was polymerized and yielded a hybrid material with improved storage modulus and increased T_g which points to a crosslinking of the polymer. [148] [97] Ethoxy ligands of the cluster were similarly exchanged with 4-vinylphenoxy ligands through a transesterification reaction with 4-acetoxystyrene. Upon polymerization with styrene, hybrid materials with improved mechanical properties above the T_g were obtained. [149] Partial exchange of the ethoxy ligands of $Ti_{16}O_{16}(OEt)_{32}$ with pyrrolidone ligands was reported with the aim to form hybrid dynamers. Four of the ethoxy ligands were thereby exchanged with 1-(2-hydroxyethyl)-2-pyrrolidone to yield the cluster $Ti_{16}O_{16}(OEt)_{28}(OCH_2CH_2N(C=O)C_3H_6)_4$. Pyrrolidone ligands are hydrogen bond acceptor molecules. Upon mixing the cluster with thiourea - terminated PDMS, a weakly crosslinked polymer was obtained where the cluster was bonded to the polymer backbone through the hydrogen bonding of the pyrrolidone ligand. [150]

Upon exchange of alkoxo ligands with alcohols the charge and coordination number is perfectly balanced. This is not the case when alkoxo ligands are replaced by bidentate ligands such as carboxylates, and reports about alkoxo / carboxylate exchange are sparse. Nevertheless, exchange of two alkoxo ligands of the clusters $Ti_3O(O^iPr)_{10}$ or $Ti_3O(O^iPr)_9(OMe)$ with benzoic acid was reported to yield the cluster $Ti_3O(OOCPh)_2(O^iPr)_8$.[41] The reaction was performed by adding 1.5 eq. of benzoic acid to the preformed alkoxo cluster. Increasing the acid proportion to 2 eq.

resulted in partial degradation of the cluster and decreased yields.

The exchange of carboxylate ligands in transition metal carboxylate clusters with carboxylic acids was reported more often in the literature.

The cluster $Ti_8O_{10}(OOCR)_{12}$ ($R = C_6H_5$, CH_3, $CH(CH_3)_2$, $C(CH_3)_3$) appeared extraordinary stable in ligand exchange reactions with carboxylates.[55][54] Addition of trichloroacetic acid to $Ti_8O_{10}(OOCCH_3)_{12}$ resulted in complete exchange of the acetate ligands, and the cluster $Ti_8O_{10}(OOCCCl_3)_{12}$ was formed. The exchange reaction was reversible and thus all intermediate partially exchanged clusters were accessible. Similarly *Frot et al.* showed the full exchange of the benzoate ligands of $Ti_8O_{10}(OOC_6H_5)_{12}$ with acetate ligands and verified the intactness of the cluster core through ^{13}C MAS NMR spectroscopy and powder XRD.[54] Furthermore, ligands of the cluster $Ti_8O_{10}(OOC^iPr)_{12}$ were fully exchanged in a solvothermal reaction with trichloroacetic acid or pivalic acid. The intactness of the cluster core was evidenced by single crystal XRD.[55]

The cluster $Zr_6O_4(OH)_4(OMc)_{12}$ led to highly crosslinked polymers upon polymerization. Decreasing the number of functional ligands with the aim to decrease the crosslinking density in the hybrid material was achieved by partial exchange of four methacrylate ligands with isobutylate ligands. The same cluster $Zr_6O_4(OH)_4(OMc)_8(OIsob)_4$ was accessible as crystalline product from a "one‑pot" reaction of a mixture of methacrylic acid and isobutyric acid. A detailed NMR spectroscopic investigation of the exchange products and the crystallized products revealed that the cluster core stayed intact during the exchange reaction.[53]

If the incoming ligands are multifunctional, ordered structures, such as metal organic framework (MOF)‑like structures, can be built up starting from clusters as simple NBB. Solvothermal reaction of the cluster $Zr_6(O)_4(OH)_4(OMc)_{12}$ with dicarboxylic acids such as muconic acid or terephthalic acid led to MOF structures, which resembled the known structure of UiO-66 MOF.[58][104] The advantage of this approach, when compared to common MOF synthesis which often uses metal salts, is the bottom‑up strategy where clusters are used as NBB to assemble higher ordered structures.

Site‑selective exchange of ligands can be pursued, when incoming ligands which essentially differ in their ligand‑metal bond strength or which show a specific coordination behavior are used in exchange reactions. Acac-H for example is known to coordinate almost exclusively in a chelating coordination mode. Hence clusters bearing both chelating and bridging carboxylate ligands can potentially undergo selective ligand exchange. This was probed with the cluster $Zr_4O_2(OMc)_{12}$

in which two of the twelve methacrylate ligands are chelating. However, addition of acac-H led to degradation of the cluster and formation of the complex $Zr(OMc)_2(acac)_2$. [59]

An interesting different class of oxo clusters are clusters of the family $Mn_{12}O_{12}(OOCR)_{16}(H_2O)_4$ ($R = CH_3$, CH_2Cl, $CHCl_2$, CF_2Cl, CF_3, C_6H_5 and C_6F_5). These clusters have special magnetic properties and are commonly seen as single-molecule magnets (SMM). Ligand exchange on this type of cluster showed that the geometry of the cluster core was not altered, thus magnetic coupling between the Mn atoms remained after ligand exchange. The electronic structure of the ligand influences the electronic structure of the core and thereby can show effects on the magnetic behavior. Partial replacement of the acetate ligands of $Mn_{12}O_{12}(OOCCH_3)_{16}(H_2O)$ with o-cyanobenzoate ligands was reported with the aim to promote special packing in the crystal structure through the -CN ligands. Coordination of the electronegative ligands on the cluster resulted in altered antiferromagnetic exchanges. [151]

Furthermore exchange of the acetate ligands of the cluster $Mn_{12}O_{12}(OOCCH_3)_{16}(H_2O)$ with acrylates followed by copolymerization with ethylacrylate led to hybrid materials where the magnetic properties of the cluster were transferred to the polymer. [86]

4.2 Results and Discussion

Complete exchange of the methacrylate ligands of $Zr_4O_2(OMc)_{12}$ (**Zr4**, see Fig. 4.1) with pivalate ligands was tested. The intactness of the cluster core was verified by two-dimensional NMR spectroscopy as well as by exchange/re-exchange reactions and FIR spectroscopy. Simulated IR spectra based on DFT calculations allowed an exact assignment of the IR bands and the determination of the $[Zr_4O_2]$ core vibrations. Despite the possibility to exchange all methacrylate ligands of **Zr4** with pivalate ligands, the same does not necessarily holds true for other incoming carboxylate ligands which differ in their steric nature. This was tested in a study where the methacrylate ligands of **Zr4** or $Ti_4Zr_4O_6(OBu)_4(OMc)_{16}$ (**Ti4Zr4**, see Fig. 4.2) and the pivalate ligands of $Zr_4O_2(OPiv)_{12}$ (**ZrPiv**, OPiv = pivalate, see Fig. 4.1) were partially exchanged with carboxylic acids of different steric properties. The number of exchanged ligands depending on the amount of incoming ligands was evaluated in this studies. Scrambling reactions, as a second type of ligand exchange reactions were tested. Scrambling reactions are an attractive preparative route to mixed-ligand clusters, since the composition of the ligand sphere is completely predetermined by the proportion of the individual clusters. This enables to exchange an exact proportion of ligands and, in case of **Zr4**, an exact determination of the crosslinking ability of the cluster is possible.

Ligand exchange reactions of coordinatively bonded ligands such as carboxylate ligands are equilibrium reactions according to eq. 4.1.

$$M_xO_yL_z + n\,H\!\!-\!\!L' \rightleftharpoons M_xO_yL_{(z-n)}L'_n + n\,H\!\!-\!\!L \tag{4.1}$$
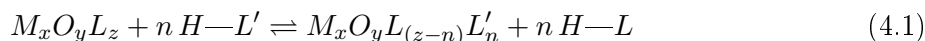
The system can be shifted to the left or the right side by varying the concentration of H-L or H-L'. The amount of incoming ligand H-L' which leads to a partial or complete exchange of the coordinated ligands depends therefore on the magnitude of the equilibrium constant of the exchange reaction. In case that the cluster core is retained after complete exchange of the ligands (going from left to right in eq. 4.1), the back reaction (going from right to left in eq. 4.1) must result in the original cluster $M_xO_yL_z$

This reaction was probed with the cluster **Zr4** and exchange of the methacrylate ligands with pivalate ligands. Treating the cluster with 250 eq. of pivalic acid resulted in the complete exchange of the methacrylate ligands, as shown in the room temperature NMR spectra in Fig. 4.3(b)
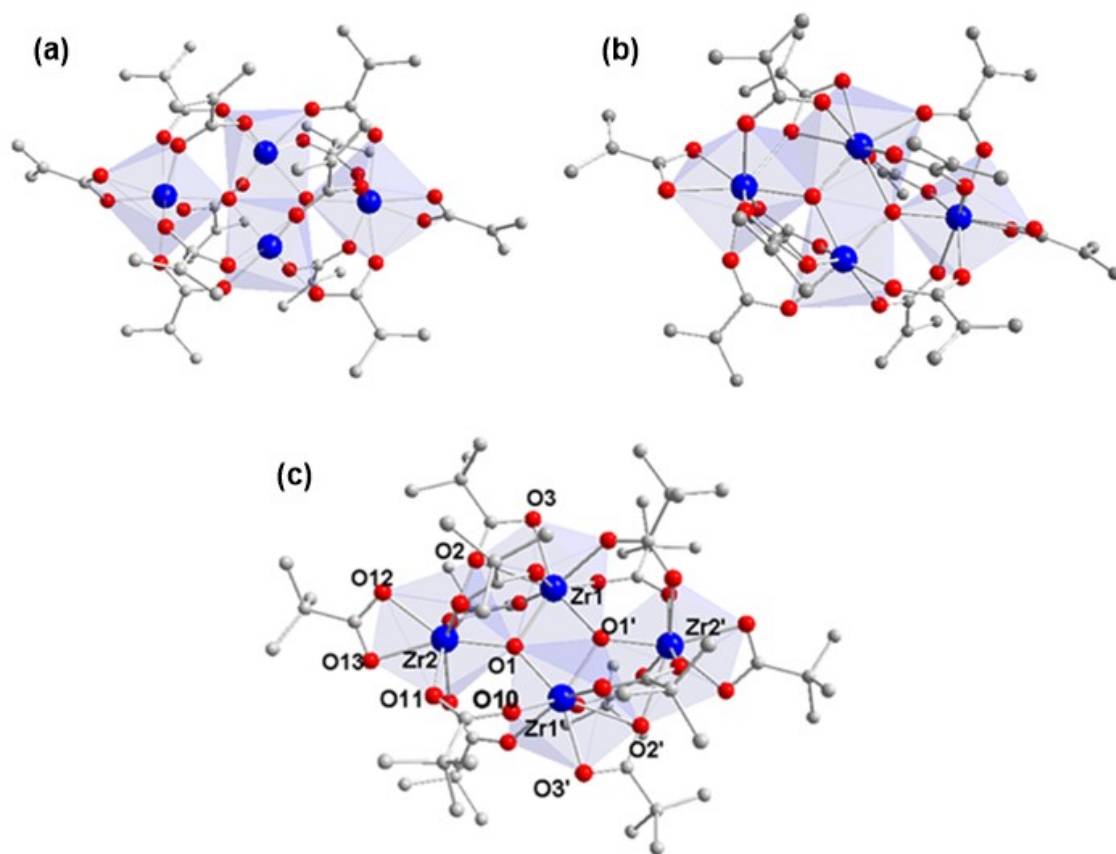
Figure 4.1: The two crystallographically determined structures of **Zr4** (symmetrical structure **Zr4** (a); asymmetric structure **Zr4_as** (b)) and the molecular structure of **ZrPiv**. Hydrogen atoms are omitted for clarity.

The ligands of the cluster **Zr4** undergo fast ligand exchange and only one set of signals with three singlets is observed in the room temperature spectra (see Fig. 4.3(a)). The signals can be assigned to the methyl protons at 1.92 ppm and the methylene protons at 6.22 ppm and 5.58 ppm. The same dynamic behavior was also found for the pivalate cluster **ZrPiv** which shows only one singlet at 1.16 ppm (see Fig. 4.3(b)).

The reversibility of the ligand exchange experiment was tested by multiple treatment of the cluster **ZrPiv** with a large excess of methacrylic acid. The re‑exchange product was examined by NMR spectroscopy and revealed a signal pattern which was identical with the pattern found for the pristine cluster **Zr4** (compare Fig. 4.3 (a) and Fig. 4.3 (c)).

IR spectroscopy was used to further investigate the intactness of the cluster core after exchange reaction. IR spectroscopy is undoubtedly a very convenient characterization method but unfortunately characteristic bands of the cluster core in the far‑infrared region (FIR) are difficult to identify and bands of the ligands in the mid‑infrared region (MIR) do not provide relevant

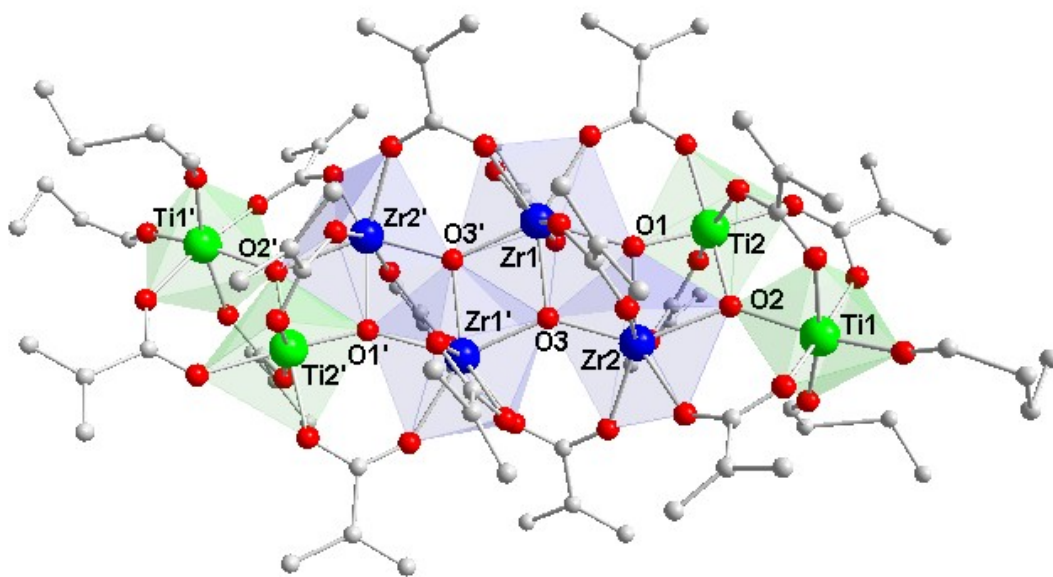**Figure 4.2:** Molecular structure of **Ti4Zr4**. Hydrogen atoms are omitted for clarity.
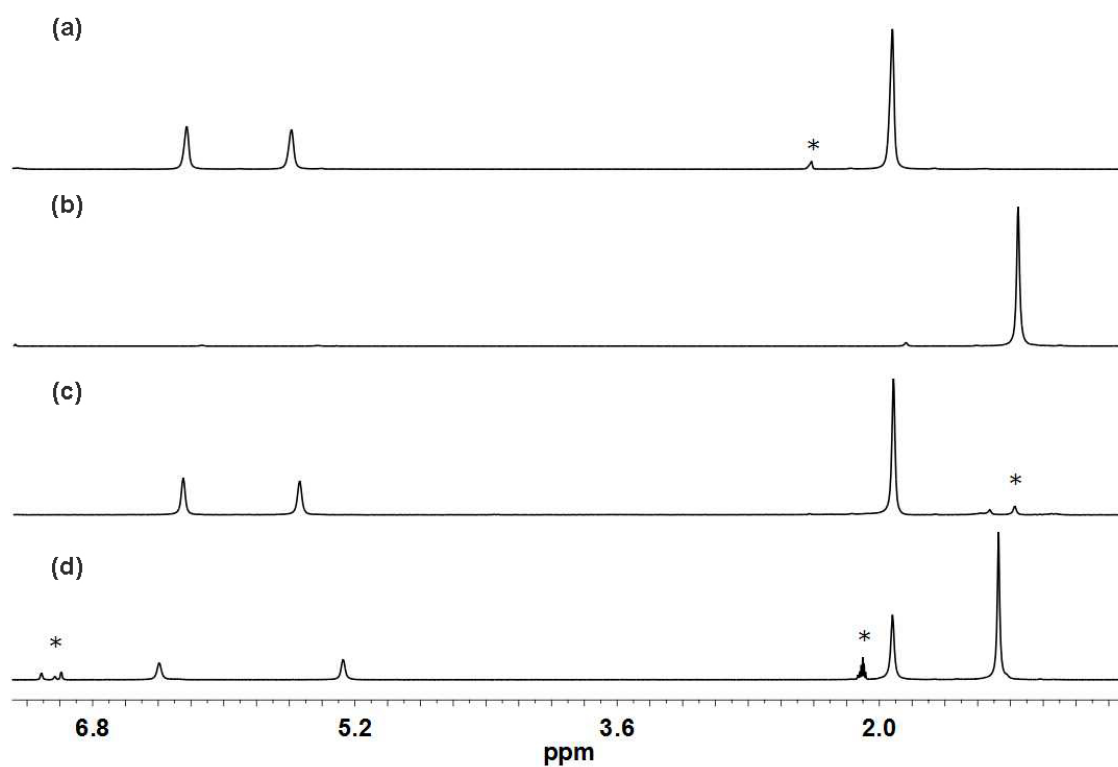

Figure 4.3: ^{1}H NMR spectra (CDCl$_3$, 25 °C, 250 MHz) of (a) original cluster **Zr4**, (b) exchange product **ZrPiv**, (c) the cluster **Zr4** after re‑exchange and (d) Zr$_4$O$_2$(OMc)$_6$(OPiv)$_6$ obtained through scrambling reaction. Residual solvent peaks (toluene and hexane) from washing are marked with an asterix.

information on the intactness of the core. The DFT calculated spectrum of the symmetric cluster **Zr4** (see Fig. 4.1 (a)) was therefore used to assign the core vibration bands and was compared with the experimental ATR - FIR spectra of the methacrylate and pivalate cluster (Fig. 4.4). The agreement in terms of band shift and band shape of the calculated and experimental spectra are sufficiently good. The unscaled calculated frequencies are shifted slightly by about 5 % to higher wave numbers. The bands of the asymmetric stretching vibration of the μ - O - bridges in the methacrylate cluster at $520\,\mathrm{cm^{-1}}$ (calculated: $512\,\mathrm{cm^{-1}}$) are slightly shifted to $524\,\mathrm{cm^{-1}}$ in the pivalate cluster. The symmetric and asymmetric stretching modes of the Zr - μ - O core of the methacrylate cluster can be found at $247\,\mathrm{cm^{-1}}$ (calculated: $263\,\mathrm{cm^{-1}}$) and $292\,\mathrm{cm^{-1}}$ (calculated: $276\,\mathrm{cm^{-1}}$) and appear at $228\,\mathrm{cm^{-1}}$ and $257\,\mathrm{cm^{-1}}$ in the pivalate cluster. The good agreement of the core vibration modes in both the methacrylate and pivalate cluster show that the core was preserved during the exchange reaction. Experimental and calculated IR bands are shown in Tab. 4.1.
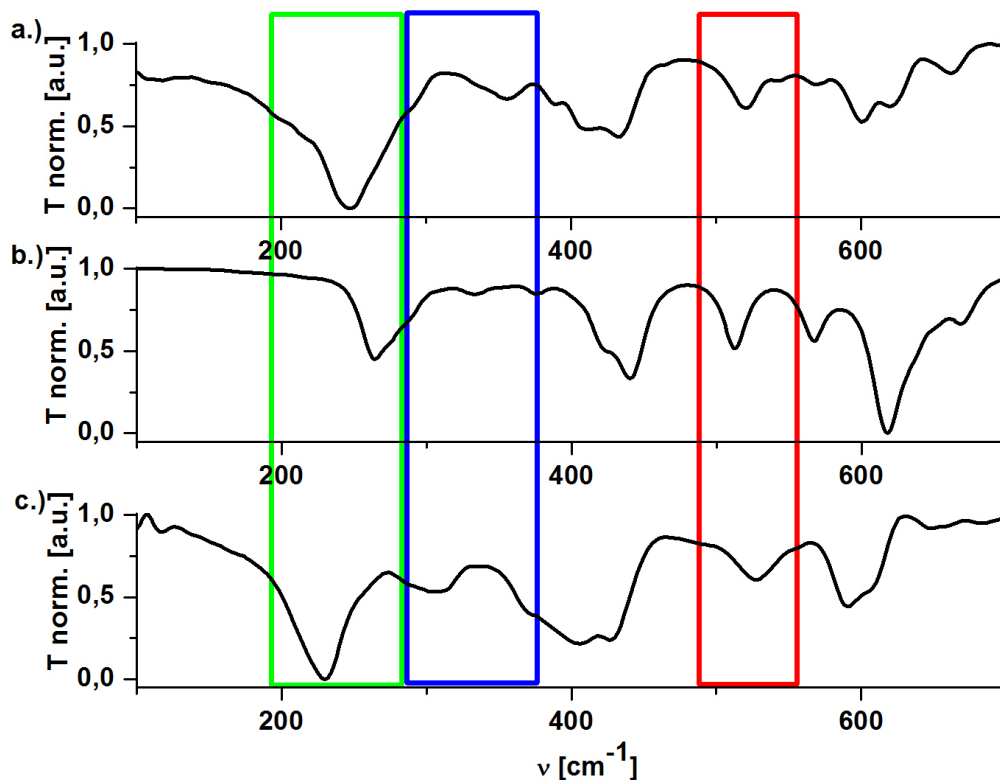

Figure 4.4: IR spectra of the FIR region of **Zr4** (calculated (Def2TZVP|TZVP, TPSS): (a), ATR: (b)) and experimental spectrum of **ZrPiv** (c).

Table 4.1: IR bands (cm^{-1}) of **Zr4** and **ZrPiv** and calculated IR bands of **Zr4** (TPSS Def2TZVP|TZVP level of theory).

Zr4	calc.	**ZrPiv**	assignment	**Zr4**	calc.	**ZrPiv**	assignment
2978	3149	2960	$\nu_{as}(CH_3)$	1009	1027	-	$\omega(CH_3)$
2926	3062	2928	$\nu_s(CH_3)$	940	979	-	$\omega(CH_2)$
1646	1732	-	$\nu_{as}(CCH_3CH_2)$	663	670	-	$\tau(CH_2)$
1582	1683	1579	$\nu_{as}(COO)^b$	601	619	591	$\nu_s(COO)^b$
1559	1662		$\nu_{as}(COO)^b$	569	567		$\nu_{as}(COO)^b$
1495	1578		$\nu_{as}(COO)^c$	520	512	523	$\delta_s(\mu O\text{-}Zr)$
1459	1515	-	$\nu_s(COO)^c$	433	438	425	$\nu(CCH_3R)^1$
1419	1498	1485	$\nu_s(COO)^b$	405	420	402	$\nu(CCH_3R)^1$
1371	1473	1361	$\nu_s(COO)^b$	292	276	257	$\delta_{as}(\mu O\text{-}Zr)$
1239	1280	1228	$\nu_s(CCH_3R)^1$	247	263	228	$\delta_s(\mu O\text{-}Zr)$

[1] R = CH$_2$ for **Zr4** and (CH$_3$)$_2$ for **ZrPiv**. b = bridging, c = chelating carboxylates; ω wagging vibration, τ twisting vibration, δ deformation vibration.

Crystals of only low quality for single crystal XRD could be grown from **ZrPiv**. Nevertheless the core of the cluster **ZrPiv** was determined and turned out to be the same as **ZrPiv** obtained from reaction of $Zr(O^iPr)_4$ and pivalic acid (see Fig. 4.1 (c)).

The two structures of **Zr4**, which show the molecular symmetry of C_i (**Zr4**) or C_1 (**Zr4_as**) were described in chapter 3 before. The structure of the cluster **ZrPiv** has the same $[Zr_4O_2]$ cluster core as the two modifications of the methacrylate cluster but two pivalate ligands show a chelating-bridging coordination (O2 bridging Zr1 and Zr2, and O2 and O3 chelating Zr1). The symmetry of the pivalate cluster in the solid state structure is thus C_i.

Neglecting vibrational motions in **Zr4** gives rise to a symmetry of C_{2h}. Thus, four sets of signals for the non-equivalent methacrylate ligands are expected in NMR spectroscopy. Only one set was observed in the room temperature NMR spectrum of **Zr4**, due to the dynamic exchange processes. This changes when the temperature is decreased to -80 °C and the one set splits up in four sets, in agreement with the symmetry considerations. These four sets correspond to the two chelating ligands, to the two ligands in the horizontal plane and two signals corresponding to the eight ligands oriented out of the plane. The carboxylate region of the ^{1}H-^{13}C NMR spectrum at -80 °C is shown in Fig. 4.5 (a) and shows the four signals of the carboxylate carbons. Three signals at high field (173.2 ppm, 174.2 ppm and 181.1 ppm) correspond to the bridging methacrylates while the fourth signal of the chelating methacrylates is shifted to low field (186.7 ppm).

The same splitting of signals was found for the pivalate cluster (see Fig. 4.5 (b)): The bridging pivalate ligands gave-cross peaks at 185.9 ppm, 186.3 ppm and 194.0 ppm and the chelating ligand at 199.3 ppm, thus the symmetry of the cluster was preserved upon complete exchange of the carboxylate ligands. After re-exchange of the methacrylate ligands with pivalate ligands the low-temperature ^{1}H-^{13}C NMR spectrum showed the same signal pattern as the spectrum of the pristine methacrylate cluster (compare Fig. 4.5 (a) and (c)).
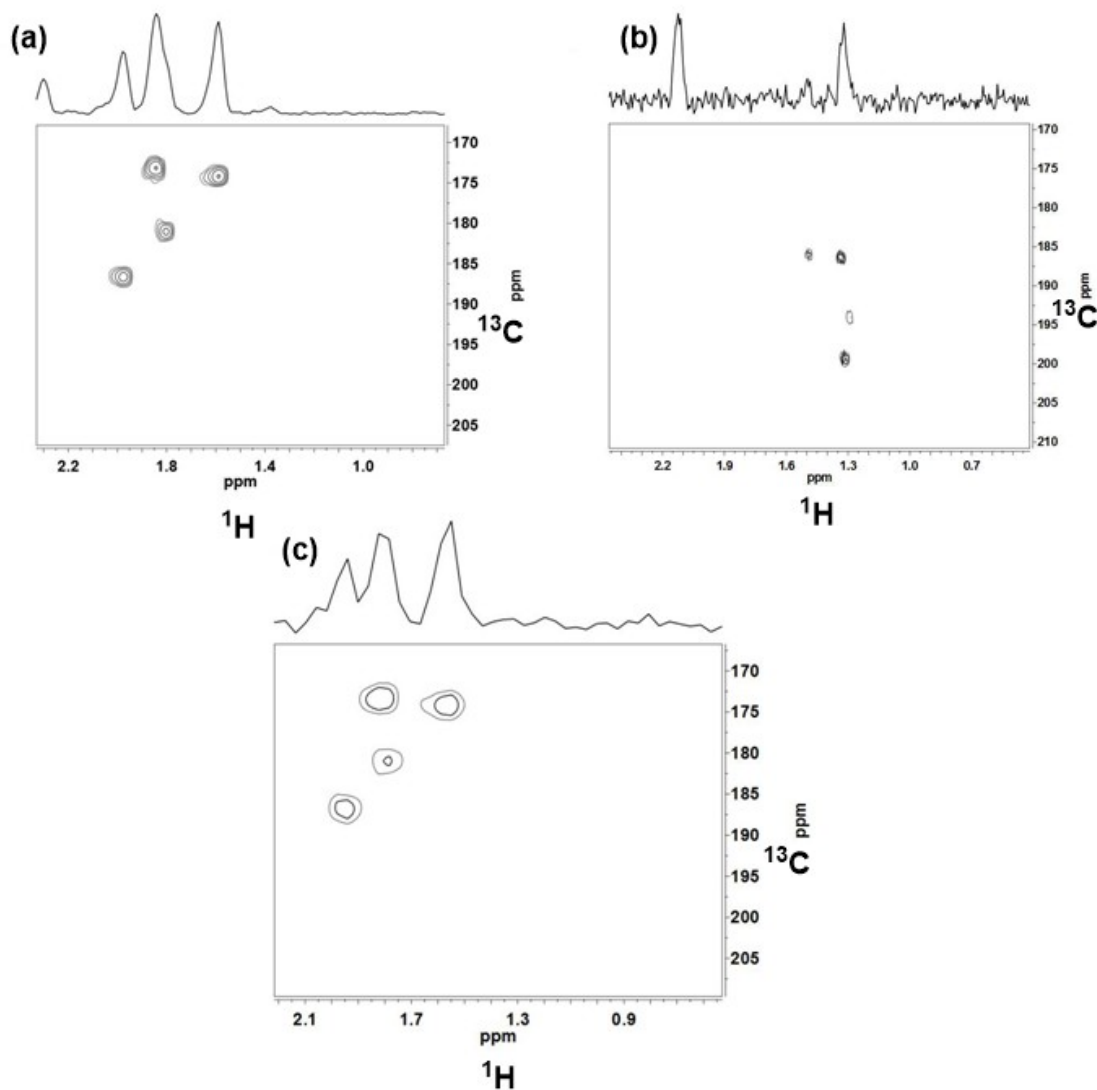
Figure 4.5: ^{1}H-^{13}C HMBC spectra (-80 °C, Tol-d_8, 300 MHz) of **Zr4** (a), **ZrPiv** (b) and **Zr4** after re-exchange (c).

Considering these results, a partial exchange of the ligands should lead to the mixed-ligand cluster $Zr_4O_2(OMc)_{12-x}(OPiv)_x$ with the same cluster core as **Zr4**. A reaction mechanism for carboxylate exchange with carboxylic acids was proposed before and proceeds through change of the coordination of the original carboxylate ligand from η_2 to η_1, coordination of H-L' to the vacated coordination site, proton transfer from the incoming ligand to the leaving group, elimination of the leaving ligand and change of the coordination of the incoming ligand from η_1 to η_2.

Having shown that complete exchange of the methacrylate ligands of **Zr4** with pivalate ligands proceeds under retention of the cluster core and that the mixed-ligand intermediate clusters

are accessible by ligand exchange reactions, we were also interested in investigating steric effects of the incoming ligand on the ligand exchange equilibrium reaction (see eq. 4.1). Carboxylic acids differing in their steric demand were probed. The steric demand thereby increased in the following order: acetic acid (HOAc) < propionic acid (HOProp) < isubutyric acid (HOIsob) < pivalic acid (HOPiv). The pKa values of the acids are very similar and range from 4.76 (acetic acid) to 5.02 (pivalic acid). Different amounts (*viz.* 4, 12, 48, 96, 300, 1000 eq. relative to the cluster) were added to a CH_2Cl_2 solution of **Zr4**. The solvent was evaporated after 30 min and the residue dried under vacuum. The number of ligands after the exchange reaction was determined by destroying the cluster in an acidic solution as described in the Experimental Section and by integration of the NMR signals of the formed acids. Results for exchange experiments on **Zr4** with ligands of different steric demand are shown in Fig. 4.6.
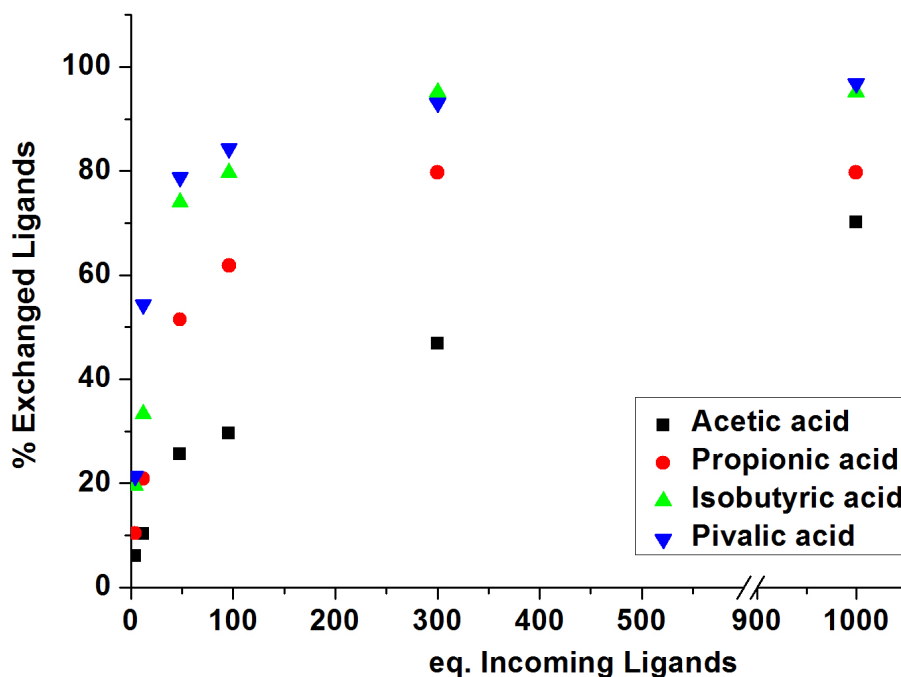
Figure 4.6: Percentage of exchanged ligands for the cluster **Zr4**.

Small amounts of incoming ligands exchanged readily the original ligands as can be seen in the steep increase of the curve. After exchange of approximately 50 - 60 % of the original ligands, exchange of the remaining ligands became increasingly difficult. This behavior was observed for all acids, but the trend is more pronounced for the sterically demanding carboxylic acids HOIsob and HOPiv. Complete exchange of the ligands was achieved by applying a high excess of HOIsob or HOPiv. However, only 70 % of the ligands were exchanged with acetate and 80 % of

the ligands were exchanged with propionate. Applying higher amounts of incoming ligands (e.g. > 1000 eq. with respect to the cluster concentration) did not increase the number of exchanged ligands but led to degradation of the cluster core.

The same experiment with HOAc, HOProp and HOIsob was repeated for the cluster **ZrPiv**. The results are summarized in Fig. 4.7 and gave the same picture as discussed before. After a steep increase at relatively low concentration of acid, the curves flattened and only 80 % of the pivalate ligands were exchanged at high incoming ligand concentrations with acetate or propionate, while complete exchange occured for isobutyrate. Interestingly, the proportion of exchanged ligands at a certain acid concentration is nearly the same for HOAc and for HOProp which was not the case in the exchange reaction with **Zr4**.
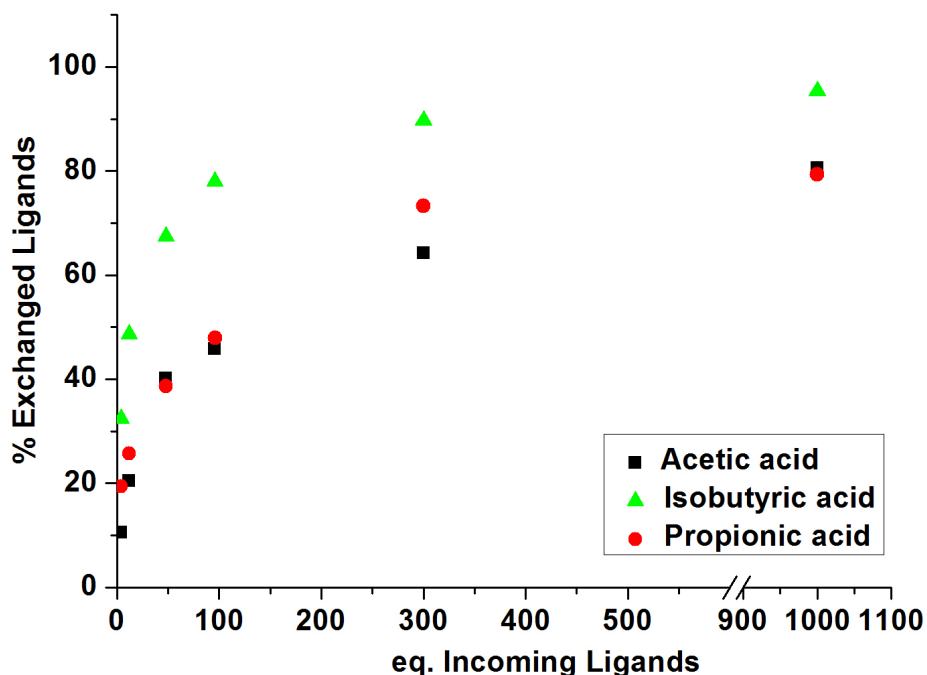
Figure 4.7: Percentage of exchanged ligands for the cluster **ZrPiv**.

To test the dependence on the type of cluster core, a third series was investigated where methacrylate ligands of **Ti4Zr4** were exchanged with 8, 16, 32, 64, 300 and 1000 eq. of HOAc, HOProp, HOIsob and HOPiv (Fig. 4.8).

The results resembled the previous experiments: After a steep increase at low incoming ligand concentration, the curves flattened and all methacrylate ligands were exchanged with pivalate or isobutyrate ligands, whilst acetate and propionate ligands exchanged only approximately 50 -

Figure 4.8: Percentage of exchanged ligands for the cluster **Ti4Zr4**.

60 % of the methacrylate ligands at high concentrations. Thereby, the amount of exchanged ligands was slightly lower at a certain acid concentration compared to the experiments with the clusters **Zr4** or **ZrPiv**.

The exchange process is assumed to happen on a rather fast time scale. Attempts to measure the kinetics of ligand exchange reactions by stop-flow IR measurements failed, which hampers 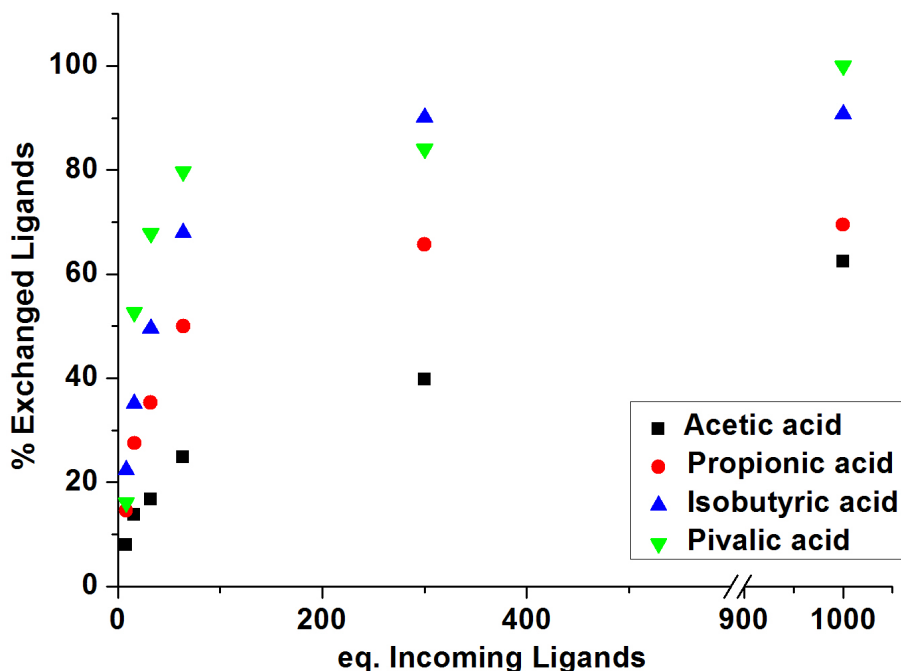an exact interpretation of the equilibrium experiment data. Different mechanistic pathways for ligand exchange reactions on nanoparticles were reported in literature which includes associative, dissociative and interchange mechanisms. [152] A dissociative mechanism would involve the formation of charged cluster species, which are not stable. An associative mechanism can be ruled out, since charge and coordination sites of the cluster core must be balanced. Therefore most possibly an interchange mechanism can be expected upon ligand exchange with carboxylic acids as incoming ligands according to the mechanism described in eq. 4.1. Since the interchange mechanism involves an increase of the number of ligands steric effects can be expected. However, this does not explain why only part of the carboxylate ligands were exchanged with acetate or propionate ligands. Values for the magnitude of the ligand exchange reactions are listed in tab. A.12 in the appendix on page XXIV.

A different approach of ligand exchange between two clusters with different ligands, but each having a uniform ligand shell are scrambling reactions. Since protic reactants are absent in this approach, the mechanism must differ to the mechanism described above (see eq. 4.2). A possible mechanism would be the formation of carboxylate bridges between the clusters. This could affect the structure of the cluster and it is not clear weather this exchange would proceed under retention of the cluster core.

$$M_xO_yL_z + n\,M_xO_yL'_z \rightarrow (1 + n)\,M_xO_yL_{\frac{z}{(1+n)}}L'_{\frac{n}{(1+n)}} \tag{4.2}$$
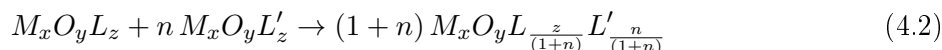
To test this possibility, the cluster $Zr_4O_2(OMc)_6(OPiv)_6$ was prepared by ligand exchange reaction with pivalic acid according to eq. 4.1. The carboxylate region of the ^{1}H-^{13}C HMBC spectrum of the mixed-ligand cluster is shown in Fig. 4.9 (a) and is a superposition of that of the pure methacrylate and pure pivalate cluster. Comparing the ^{1}H-^{13}C HMBC spectrum of the mixed-ligand clusters derived from carboxylate exchange (eq. 4.1) with that derived from the scrambling reaction (eq. 4.2) showed good agreement of the signal pattern. Both sets of carboxylate signals, one corresponding to the methacrylate and the second corresponding to the pivalate ligands, showed unresolved peaks in the high field and in the low field region. This points to the fact that the ligand exchange of cluster-bonded carboxylates with incoming carboxylic acids does not proceed site selectively. Both the chelating (highfield) and the bridging (low field) positions are occupied by methacrylate and pivalate ligands. The incoming carboxylates thus participate in the dynamic exchange process after ligand exchange. This is also evidenced by the appearance of only one set of signals for each ligand in the room temperature ^{1}H NMR spectra (see Fig. 4.3 (c) and (d)).

Nevertheless, the superposition of the methacrylate and pivalate signals could also be caused by co-existence of the purely methacrylate substituted and pivalate substituted clusters in solution. ^{1}H-^{1}H EXSY spectra of the $Zr_4O_2(OMc)_6(OPiv)_6$ cluster were recorded to exclude this possibility (see Fig. 4.10). NOE signals between the methacrylate and pivalate ligands were seen which prove that both the methacrylate and the pivalate signals are bonded to the same cluster core. The ^{1}H-^{1}H EXSY spectra of the cluster obtained from carboxylic acid exchange (Fig. 4.10 (a)) and through scrambling reaction (Fig. 4.10 (b)) are identical, thus the same mixed-ligand cluster $Zr_4O_2(OMc)_6(OPiv)_6$ was formed. Furthermore, this cluster must have the same cluster core as the clusters **Zr4** and **ZrPiv**, independently from the preparation protocol.

As stated above, the low-temperature ^{1}H-^{13}C HMBC spectra of the mixed-ligand cluster
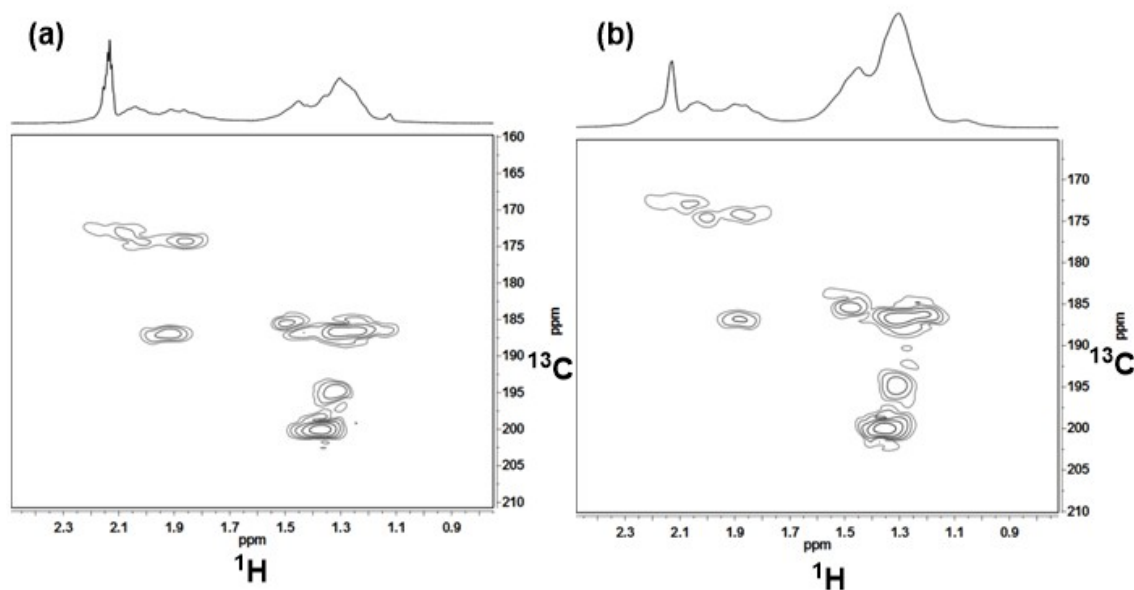
Figure 4.9: ^{1}H-^{13}C HMBC spectra (-80℃, Tol-d$_8$, 300 MHz) of Zr$_4$O$_2$(OMc)$_6$(OPiv)$_6$ obtained by carboxylic acid exchange (a) and through scrambling reaction (b).
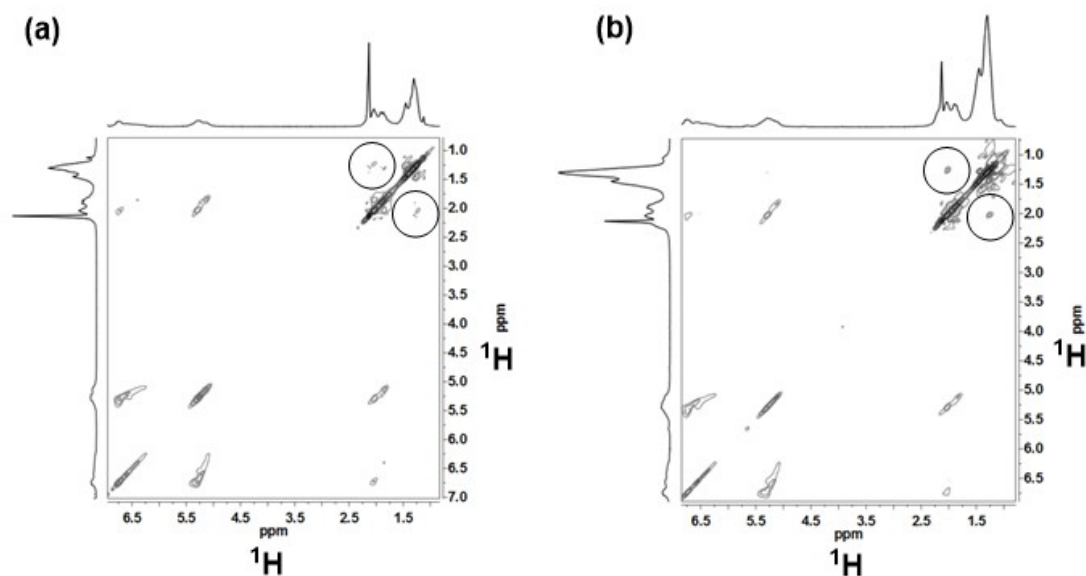
Figure 4.10: ^{1}H-^{1}H EXSY spectra (-80℃, Tol-d$_8$, 300 MHz) of Zr$_4$O$_2$(OMc)$_6$(OPiv)$_6$ prepared through carboxylic acid exchange (a) and through scrambling reaction (b). NOE signals are marked with a circle.

Zr$_4$O$_2$(OMc)$_6$(OPiv)$_6$ shows the full set of signals (bridging at high and chelating at low field) for both types of ligands (Fig. 4.9). Similarly the ^{1}H NMR spectrum at room temperature (Fig. 4.3 (d)) shows only one set of signals due to dynamic exchange processes for both ligand types. Therefore, both ligands participate in the exchange dynamics and site-selective exchange. This

means that preferred exchange of only chelating or only bridging ligands seems to be unlikely when leaving and incoming ligands are carboxylates. Site selective exchange, however, would be a big step forward in terms of NBB design and assembling higher ordered framework structures.

For site-selective functionalization of the cluster the entering group must most likely be a ligand which shows different bonding characteristics compared to carboxylate ligands. This can be either a more distinct affinity to a special coordination site on the cluster (e.g. a higher bond strength to one of the metals in a mixed metal cluster) or a special coordination behavior (e.g., exclusive exchange of chelating ligands). Acac as monoanionic bidentate ligand which is mainly chelating seems to be a good choice for specific exchange of chelating carboxylates. However, the risk of cluster degradation or rearrangement is increased when incoming and leaving ligands are of a different type. The cluster **Zr4** was degraded upon addition of acac-H as previously reported, and the complex $Zr(OMc)_2(acac)_2$ was formed quantitatively.[59]

Because of the previous finding that **Zr4** degrades upon reaction with acac-H [59], two other cluster structures were tested in exchange reaction with acac-H. The clusters $Ti_4Zr_4O_6(OBu)_4(OMc)_{16}$ (**Ti4Zr4**) and $[Zr_6O_4(OH)_4(OOCR)_{12}]_2 \cdot 6RCOOH$ (R = Et (**Zr12Pr**) and $CH_2CH{=}CH_2$ (**Zr12VAC**)) contain both chelating and bridging carboxylate ligands. Besides carboxylates in different coordination mode both clusters have other features which might effect a site specific ligand exchange.

In **Ti4Zr4** the carboxylates bridge Ti and Zr atoms or coordinate chelating to a Zr atom. Ligands coordinated to the Ti atom might have a different reactivity than those coordinated to the Zr atoms or bridging Ti and Zr atoms. Four butoxide ligands are coordinated on the terminal sides. These ligands could be substituted selectively (possibly by concomitant rearrangement of the cluster core) through acac ligands.

The dimeric clusters **Zr12VAC** and **Zr12Pr** (see Fig. 4.13) consist of two $[Zr_6O_4(OH)_4]$ core units which are connected through four bridging carboxylate ligands. This connection of the two core units appears to be stable upon dissolving the cluster, since the dimeric form does not disproportionate in solution in the monomeric form $Zr_6O_4(OH)_4(OOCR)_{12}$. The monomeric form is also stable and was obtained with different carboxylate ligands. Besides a possible exchange of one or more chelating carboxylate ligands on the terminal end of the cluster, an exchange of the interconnecting bridging carboxylates is conceivable upon reaction with acac-H.

The cluster **Ti4Zr4** is shown in Fig. 4.2 and consists of a zig-zag chain of four central $[ZrO_8]$ or $[ZrO_7]$ polyhedra and two terminating $[TiO_6]$ octahedra sharing common edges. Two additional

$[TiO_6]$ octahedra are condensed at both ends of the main chain. The butoxide ligands are coordinated to the terminal Ti atoms. Two methacrylate ligands chelate the Zr atoms in the center of the cluster (Zr1), four bridge two Ti atoms, four bridge two Zr atoms and the remaining six bridge a Ti and a Zr atom. Despite the mixed‑metal character of the cluster, methacrylate ligands show a dynamic behavior as evidenced by NMR spectroscopy.

Reaction of 4 eq. of acac-H with **Ti4Zr4** in CH_2Cl_2 led to the formation of the mixed‑metal cluster $Ti_2Zr_4O_4(OMc)_{16}$ (**Ti2Zr4**), which was crystallized and whose structure was elucidated by single crystal XRD (see Fig 4.11 (a)).
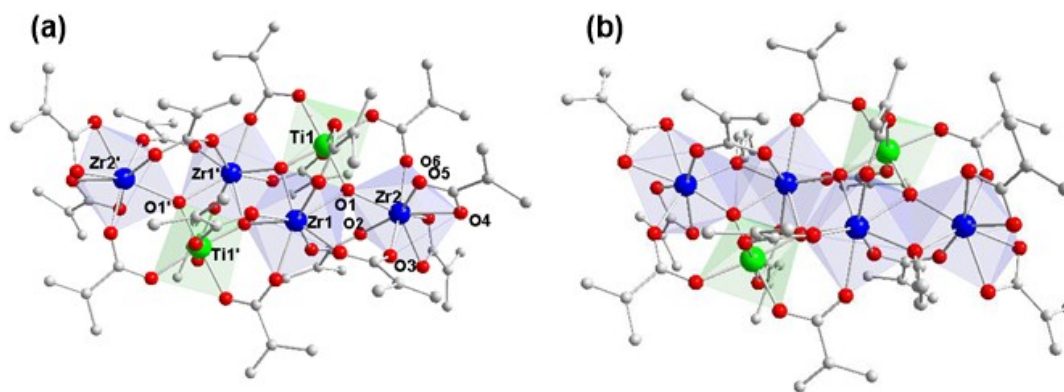

Figure 4.11: Molecular structure of $Ti_2Zr_4O_4(OMc)_{16}$ (**Ti2Zr4**) (a) and $Ti_2Zr_4O_4(OBu)_2(OMc)_{14}$ (**Ti2Zr4_2**) (b). Hydrogen atoms are omitted for clarity.

This cluster can formally be obtained by elimination of $Ti(OBu)_2(acac)_2$ and water and reorganization of the remaining cluster core. The complex $Ti(OBu)_2(acac)_2$ was verified by mass spectroscopy (MS) and NMR spectroscopy. The ESI mass spectrum (see Fig. 4.12) showed the sodium adduct of the complex with highest intensity at m / z = 415.1 as well as the $[Ti(OBu)(acac)_2]^+$ fragment at m / z = 319.1. The signal at m / z = 401.1 was assigned to the sodium adduct of $Ti(OBu)(O^iPr)(acac)_2$ which stems from ^iPrOH impurities in the mass spectrometer. Furthermore the $[Ti(OBu)_2(acac)_2Na_2Cl]^+$ adduct was found at m / z = 473.1.

The cluster **Ti2Zr4** has a centrosymmetric core which consists of a zig‑zag chain of two $[ZrO_8]$ dodecahedra (Zr1 and Zr1' in Fig 4.11 (a)) and two $[TiO_6]$ octahedra (Ti1 and Ti1') sharing edges. This chain is terminated by two $[ZrO_8]$ dodecahedra (Zr2 and Zr2') which share a corner (O1) with the $[ZrO_8]$ and $[TiO_6]$ polyhedra of the zig‑zag chain. Four methacrylate ligands are chelating, two at each terminal $[ZrO_8]$ unit. Two methacrylate ligands bridge two Zr atoms and the remaining four bridge a Ti and a Zr atom. This cluster is isostructural to a previously
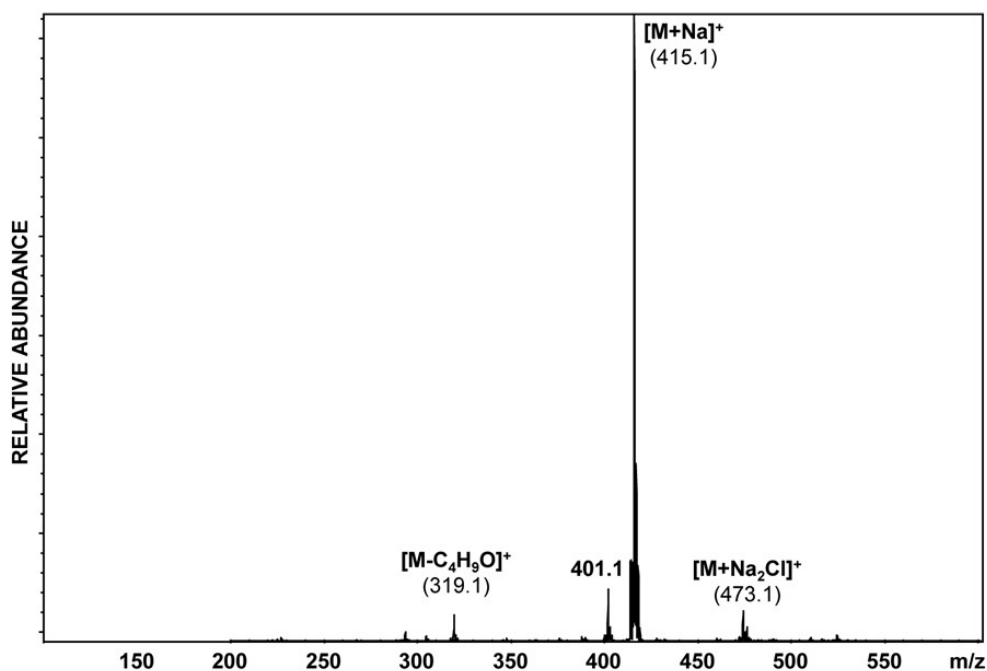
Figure 4.12: ESI mass spectrum of the supernatant after reaction of **Ti4Zr4** with reaction of 4 eq. acac-H. The signals correspond to the sodium adduct of $Ti(OBu)_2(acac)_2$ at $m/z = 415.1$ and fragments of the complex.

reported cluster $Ti_2Zr_4O_4(OBu)_2(OMc)_{14}$ (**Ti2Zr4_2**) where one of the methacrylate ligands bridging Zr1 and Zr2 or Zr1' and Zr2' is replaced by a μ_2-OBu group (see Fig. 4.11 (b)). [24] NMR spectra of **Ti2Zr4** show dynamic exchange of the methacrylate ligands.

Comparing the structures of **Ti4Zr4** (Fig 4.2) and **Ti2Zr4** (Fig. 4.11 (a)) shows that major cluster rearrangement took place upon reaction of **Ti4Zr4** with acac-H. The cleavage of a $[TiO(OBu)_2]$ unit from the structure vacates two coordination sites at Zr but at the same time results in three dangling OMc ligands. This is compensated by an increase of the coordination number of the terminal Zr atom from seven in **Ti4Zr4** to eight in **Ti2Zr4**. The two central $[Zr_2Ti(\mu_3O)]$ units of the original cluster appear twisted in **Ti2Zr4** and connect in a difference manner. This goes along with a major rearrangement of the ligand shell. No other clusters or degradation products were observed, which led to the conclusion that the cluster **Ti2Zr4** appears to be stable against further attack of acac-H.

The dimeric clusters **Zr12VAC** and **Zr12Pr** were used as a second cluster type for exchange reactions with acac. This dimeric cluster type was obtained with a variety of carboxylate ligands

as reported before. [33] The vinylacetate‑capped cluster is shown as example in Fig. 4.13 (a). This cluster dimer consists of two octahedral $[Zr_6O_4(OH)_4]$ units which are connected through four bridging carboxylate ligands. Each unit is capped by three chelating and seven bridging carboxylate ligands. The chelating ligands are coordinated on the terminal sites of the cluster.

Reaction of 50 eq. acac-H with the propionate and the vinylacetate substituted clusters resulted in exchange of each one terminal chelating carboxylate ligand and formation of the clusters $[Zr_6O_4(OH)_4(OOCCH_2CH=CH_2)_{11}(acac)]_2 \cdot CH_2=CHCH_2COOH_6$ (**Zr12VAC_acac**) and $[Zr_6O_4(OH)_4(OOCEt)_{11}(acac)]_2 \cdot EtCOOH_6$ (**Zr12Pr_acac**). The structure was solved completely for the vinylacetate capped cluster. Crystals grown from the propionate substituted cluster were only of poor quality and data could not be sufficiently refined. Nevertheless, the data collected for the propionate derivative showed clearly that the exchange products of the vinylacetate and propionate clusters are isostructural. The molecular structure of **Zr12VAC_acac** is shown in Fig. 4.13 (b). The six free carboxylic acid molecules (omitted in Fig. 4.13), which bind weakly through hydrogen bonding to the cluster core, were retained in the product clusters.
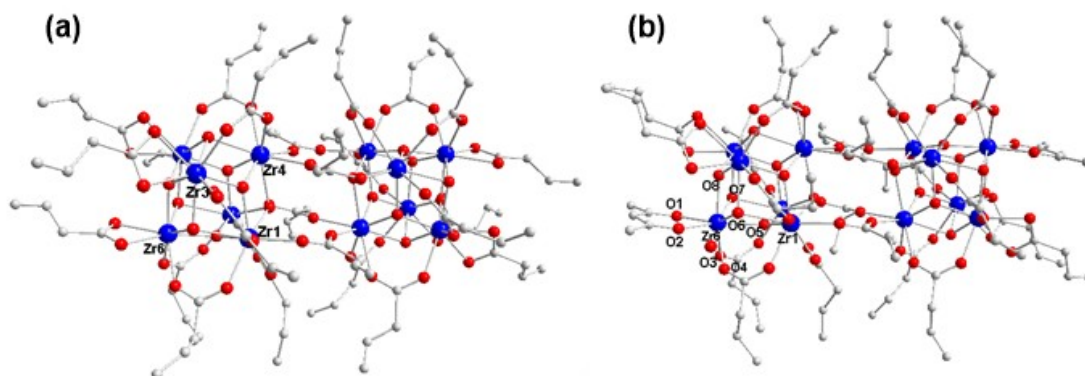
Figure 4.13: Molecular structure of **Zr12VAC** (a) and **Zr12VAC_acac** (b). Hydrogen atoms are omitted for clarity.

The clusters $[Zr_6O_4(OH)_4(OOCR)_{12}]_2$ and $[Zr_6O_4(OH)_4(OOCR)_{11}(acac)]_2$ are isostructural, thus the cluster core is retained during exchange of two carboxylate ligands with two acac ligands per formula unit. The bite angle of the acac ligand is larger than the bite angle of the chelating carboxylate ligands while the Zr‑O bond lengths of the acac ligands appear shortened compared to the carboxylate Zr‑O bond lengths. This does not have a distinct effect on other bond lengths and angles in the close environment of the acac ligand. The Zr‑O bond distances for the μ_3‑O and μ_3‑OH groups are slightly elongated in the acac‑exchanged clusters.

Despite the rather large excess of acac-H in the exchange reaction, substitution of a second

carboxylate ligand was not achieved. The reason might be an activation of the exchanged carboxylate ligand. Compared to the other two chelating ligands in the $[Zr_6O_4(OH)_4]$ unit, the carboxylate ligand which is coordinated to the exchange affine site seems to be more asymmetrically bonded (Zr‑O 225.2(3) and 231.0(3) pm] than the other two chelating carboxylates.

The experiment was repeated with addition of 2, 4, 8, 12, and 24 eq. of acac-H. Crystals grown from these experiments all had the same triclinic unit cell. The structure for the clusters obtained from the experiment with 24 eq. acac-H as incoming ligand was solved and showed a partial substitution of the carboxylate ligand by acetylacetonate ($\sim 60\%$ acac occupation for the propionate cluster and $\sim 70\%$ acac occupation for the vinylacetate cluster).

The exchange process was also monitored by NMR spectroscopy. Signals in the room temperature NMR spectra could not be assigned to individual ligands due to dynamic exchange processes. The dynamic exchange in $[Zr_6O_4(OH)_4(OOCR)_{12}]_2$ was investigated before in detail and revealed that the most dynamic region was that of the chelating carboxylate ligands. [33] Despite the broadening and unresolved signals, the clusters gave a distinct signal pattern (see for example the ^{1}H NMR spectrum of **Zr12Pr** in Fig. 4.14 (a)). The same pattern was found after exchange with 4 eq. acac-H (see Fig. 4.14 (b)) and 50 eq. acac-H (see Fig. 4.14 (c)). The signal at 2.05 ppm in Fig. 4.14 (b) and (c) is due to the coordinated acac ligand. Free acetylacetone would give a signal at low field (201.7 ppm) which is absent in the ^{1}H‑^{13}C HMBC spectrum of **Zr12Pr** (see Fig. 4.15).
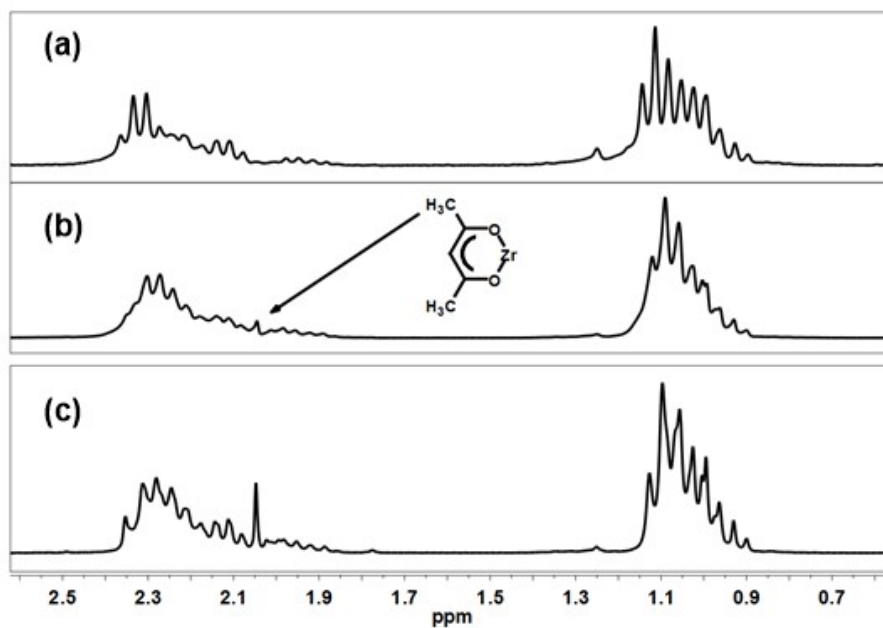
Figure 4.14: ^{1}H NMR spectrum (25 °C, CDCl$_3$, 250 MHz) of **Zr12Pr** (a) and the exchange products after exchange with 4 eq. acac-H (b) and 50 eq. acac-H (c).
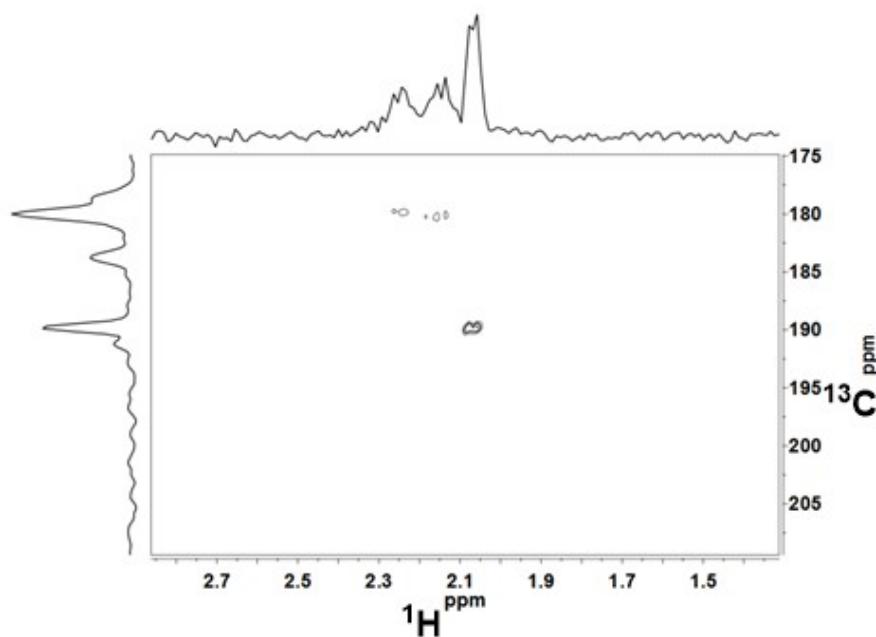

Figure 4.15: ^{1}H-^{13}C HMBC NMR spectrum (25 °C, CDCl$_3$, 300 MHz) of **Zr12Pr_acac**.

4.3 Conclusions

Ligand exchange of all of the methacrylate ligands of **Zr4** with pivalate proceeds under retention of the cluster core to yield the cluster **ZrPiv**. This was evidenced by HMBC NMR spectroscopy and by single-crystal XRD. Re-exchange experiments showed that the pristine cluster **Zr4** can be obtained again when **ZrPiv** is reacted with methacrylic acid. This leads to the conclusion that all intermediate mixed-ligand clusters $Zr_4O_2(OMc)_x(OPiv)_{12-x}$ are accessible through ligand exchange.

Exchange reactions with carboxylic acids of different steric demand with **Zr4**, **ZrPiv** and the mixed-metal cluster **Ti4Zr4** showed a dependence of the proportion of exchanged ligands on the amount of applied acid. Ligands are typically readily exchanged with low concentration of the acid. Upon increasing the acid concentration the reaction proceeded less readily. With the sterically demanding ligands HOIsob and HOPiv, nearly complete exchange was observed in all cases, while only part of the ligands was exchanged with HOAc or HOProp. Lack of kinetic data hampers a complete interpretation of these results, however, an interchange mechanism is likely.

Scrambling reactions between two clusters of the same core type but differing in their ligand sphere were introduced as a new preparation procedure. The exchange of ligands through scrambling reactions was illustrated by HMBC and EXSY NMR spectroscopy. Scrambling reactions are a facile method to obtain mixed-ligand clusters with a defined stoichiometry of the ligand sphere.

Different ligand exchange reactions with acac-H as predominately chelating ligand were performed aiming at a site-selective ligand exchange. This was successfully demonstrated for the clusters **Zr12VAC** and **Zr12Pr**. Thereby one of the chelating carboxylate ligands of the pristine clusters was exchanged with acac leading to the clusters **Zr12VAC_acac** and **Zr12Pr_acac**. The same reaction with the mixed-metal cluster **Ti4Zr4** led to elimination of $Ti(OBu)_2(acac)_2$ and rearrangement of the remaining core to yield the cluster **Ti2Zr4**. The structure of this cluster resembles the previously reported cluster **Ti2Zr4_2**.

4.4 Experimental

General methods: All operations with air or moisture sensitive materials were performed under nitrogen atmosphere using standard Schlenk techniques. Hexane, toluene and tetrahydrofurane were dried over Na/benzophenone prior to use. Dichloromethane was distilled over CaH_2. Acetonitrile was dried over P_2O_5 and freshly distilled. All solvents were kept under nitrogen atmosphere over molecular sieve. $Zr(OPr)_4$ (70 wt% in 1-propanol), $Zr(O^iPr)_4 \cdot {}^iPrOH$ (99.9 %), $Zr(OBu)_4$ (80 wt% in 1-butanol) and $Ti(OBu)_4$ (97 wt% in 1-butanol) was purchased from Sigma Aldrich and used as received. Methacrylic acid (99 %, Sigma Aldrich), pivalic acid (99 %, Sigma Aldrich), propionic acid ($\geqq$ 99.5 %, Sigma Aldrich), acetic acid ($\geqq$ 99.5 %, Sigma Aldrich), isobutyric acid (99.9 %, Sigma Aldrich) and vinylacetic acid (97 %, Sigma Aldrich), were freshly distilled over P_2O_5, prior to use.

NMR spectroscopy: ${}^1H$ and ${}^{13}C$ solution NMR spectra were recorded on a Bruker AVANCE 250 (250.13 MHz $\{{}^1H\}$, 62.86 MHz $\{{}^{13}C\}$). Gas‑tight Young tubes were used for all experiments. 2D spectra were recorded on a Bruker AVANCE 300 (300.13 MHz $\{{}^1H\}$, 75.13 MHz $\{{}^{13}C\}$) equipped with a 5 mm inverse probe head with z gradient unit with a Bruker standard pulse sequence. $CDCl_3$, CD_2Cl_2 and toluene-d8 were purchased from Euriso‑Top and degassed by freeze-pump-thaw cycles.

ATR‑IR spectroscopy: Solid state ATR‑IR spectra were recorded on a Perkin Elmer Spectrum 400 FT‑IR spectrometer equipped with a KBr window for MIR and a polyethylene window for FIR. 128 scans were averaged for MIR and 256 scans were averaged for FIR measurements. The spectra were processed with the Perkin Elmer Spectrum software and normalized with the implemented normalization routine.

X‑Ray structure analysis: All measurements were performed at 100 K unless otherwise specified, using monochromatized MoKα ($\lambda = 71.073$ pm) radiation. Data were collected on a Bruker AXS SMART APEX II four‑circle diffractometer with κ‑geometry with ϕ and ω scans and different frame widths. The data were corrected for polarization and Lorentz effects, and an empirical absorption correction (SADABS) was employed. The cell dimensions were refined with all unique reflections. SAINT PLUS software (Bruker Analytical X‑ray Instruments, 2007) was used to integrate the frames. Details of the X‑ray investigations are given in the appendix. The structures were solved by the Patterson method (SHELXS‑97 [153]). Refinement was performed by the full‑matrix least‑squares method based on F^2 (SHELXL‑97) with anisotropic thermal

parameters for all non-hydrogen atoms. Hydrogen atoms were inserted in calculated positions and refined riding with the corresponding atom.

Mass spectroscopy: Mass spectrometric measurements were performed on an Esquire 3000plus 3D-quadrupole ion trap mass spectrometer (Bruker Daltonics, Bremen, Germany) in positive-ion mode by means of electrospray ionization (ESI). Mass calibration was done with a commercial mixture of perfluorinated trialkyltriazines (ES Tuning Mix, Agilent Technologies, Santa Clara, CA, USA). The analyte was dissolved in butanol (p.a. Merck) to a concentration of ca. 1 mg/ml. Direct infusion experiments were carried out using a Cole Parmer model 74900 syringe pump (Cole Parmer Instruments, Vernon Hills, IL, USA) at a flow rate of 2 ml/min. Full scans were measured in the range m/z 100-1100 with the target mass set to m/z 1000. Mass calculations are based on the most abundant Ti isotope (^{48}Ti-isotope). Mass spectra and CID spectra were averaged during data acquisition time of 1 to 2 min; one analytical scan consisted of five successive micro scans resulting in 50 and 100 analytical scans, respectively, for the final mass spectrum.

Zr4: The cluster was prepared as previously reported.[63] The crystalline product was dried under vacuum, dissolved in a small amount of CH_2Cl_2 until a clear solution was obtained and precipitated with hexane. This procedure was repeated three times to remove free acid.

Ti4Zr4: The cluster was prepared as previously reported.[24] The yellow crystalline product was dissolved in toluene and the solvent was subsequently evaporated under vaccum to remove traces of free acid. This procedure was repeated three times.

Zr12VAC and Zr12Pr: The clusters were prepared as previously reported.[33] The clusters were purified by multiple precipitation with hexane.

Ligand exchange reactions:

Reaction of Zr4 with pivalic acid: Pivaliv acid 5.57 ml (49.35 mmol) was added dropwise to a solution of 200 mg (0.141 mmol) of **Zr4** in 10 ml of CH_2Cl_2 and stirred for 30 min. After evaporation of the solvent in high vacuum (10^{-6} mbar) the residue was redissolved in 0.5 ml of CH_2Cl_2 and precipitated from 50 ml of acetonitrile. The solution was centrifuged and the supernatant was decanted. The obtained white crystalline solid was dried under vacuum. Crystals of **ZrPiv** were grown by slow evaporation of a CH_2Cl_2 solution but were of poor quality and the structure could not be refined sufficiently. More suitable crystals were obtained by reaction of $Zr(O^iPr)_4$ and pivalic acid in the ratio 1 to 4.

In the re-exchange reaction, methacrylic acid (2.63 ml, 31.04 mmol) was added dropwise to a solution of 100 mg of **ZrPiv** (0.062 mmol) in 5 ml of CH_2Cl_2. The solution was stirred for 30 min and the solvent was subsequently removed under vacuum. The obtained white solid was dissolved in 0.5 ml of CH_2Cl_2 and precipitated by 50 ml of hexane. This procedure was applied three times.

Ligand exchange reactions with carboxylic acids differing in their steric demand: 200 mg of **Zr4**, 227 mg **ZrPiv** or 325 mg **Ti4Zr4** (0.141 mmol) was dissolved in 10 ml of CH_2Cl_2. The respective amount of carboxylic acid was added dropwise and the solution was stirred for 30 min. The solid residue was dried under high vaccum (10^{-6} mbar) for 2 h after removal of all volatiles. The product was dissolved in 5 ml toluene and the solvent removed in vacuum. This procedure was repeated three times.

50 mg of the product were dissolved in DMSO-d6. 10 μl of DCl were added and the solution was sonicated for 30 min. The solution was passed through a syringe filter to remove metal oxide particles. The NMR peaks used for determining the ligand ratio were chosen as follows: Methyl group of the methacrylic acid (3H, 1.9 ppm, s); methyl group of the acetic acid (3H, 1.88 ppm, s); methyl group of the propionic acid (3H, 0.88 ppm, t); methyl groups of the isobutyric acid (6H, 1.12 ppm, d); methyl groups of the pivalic acid (9H, 1.11 ppm, s).

Scrambling reaction: In a typical experiment 0.468 g (3.3 mmol) of **Zr4** and 0.532 g (3.3 mmol) of **ZrPiv** were dissolved in toluene and stirred at room temperature. After 30 min the solvent was removed in vacuum to yield 1g of $Zr_4O_2(OMc)_6(OPiv)_6$.

Reaction of Ti4Zr4 with acac-H: 50 mg (0.022 mmol) of **Ti4Zr4** was dissolved in 5 ml of CH_2Cl_2. Acac-H (2 or 4 molar eq.) was added and the reaction mixture was stirred for 30 min during which the pale yellow solution darkened. All volatiles were subsequently removed, and the crude product was dissolved in 2 mL of CH_2Cl_2. Crystals of **Ti2Zr4** were grown by slow evaporation of the solvent at -11℃. Yield: 78%. The unit cell of the obtained crystals was the same independent of whether 2 or 4 eq. of acac-H was used. The supernatant liquid of the crystallization experiment was separated for MS measurements. After removal of all volatiles, the solid residue was dissolved in BuOH.

[Ti(OBu₂(acac)₂]: ^{1}H NMR (25℃, $CDCl_3$, 250 MHz): $\delta = 0.94$ (s, CH_3), 0.97 (m, CH_3), 1.46 - 1.88 (m, CH_2), 4.62 (m, CH_2O), 5.37 (s, CH). ^{13}C NMR (25℃, $CDCl_3$, 62.9 MHz): $\delta = 13.59$ (CH_3), 19.24 (CH_3CH_2), 25.93 ($CH_3C(O)$), 35.17 (CH_2CH_2), 35.17 (CH_2O), 100.85

(CH$_3$C(O)CH), 188.46 (CH$_3$C(O)CH) ppm. ESI-MS (m / z, BuOH, NaCl) positive ion: (m / z M-Na$^+$ = 415.1).

Ti2Zr4: ^{1}H NMR (25 °C, CDCl$_3$, 250 MHz): δ = 1.18 - 2.25 (CH$_3$), 5.28 - 5.82 and 5.97 - 6.35 (CH$_2$). ^{13}C NMR (25 °C, CDCl$_3$, 62.9 MHz): δ = 18.31 (CH$_3$), 128.06 (CH$_2$), 138.20 (C(CH$_2$)CH$_3$), 173.68 (COO) ppm.

Reaction of Zr12Pr and Zr12VAC with acac-H: 50 mg of cluster (0.014 mmol of **Zr12Pr** or 0.013 mmol of **Zr12VAC**) was dissolved in 5 mL of CH$_2$Cl$_2$. After addition of acac-H the solution was stirred for 30 min. All volatiles were subsequently removed in vacuum and the residue was dissolved in 2 mL of THF. Crystals were grown by slow evaporation at -11 °C. The reaction was performed for 2, 4, 8, 12, 24 and 50 eq. of acac-H. Crystals obtained for 2 - 24 eq. of acac-H showed the same unit cell. The structure was solved for experiments with 24 molar eq. of acac-H for **Zr12Pr** and **Zr12VAC**. Crystals of a different unit cell were obtained by reaction with 50 eq. acac - H. Only the structure of the compound from the reaction of **Zr12VAC** with 50 eq. acac-H was solved. The measurement was done at 243 K since crystals cracked upon cooling to 100 K. The same reaction with **Zr12Pr** resulted in crystals of poor quality.

Zr12Pr_acac: ^{1}H NMR (25 °C, CD$_2$Cl$_2$, 250 MHz): δ = 0.98 - 1.11 (CH$_3$), 1.97 - 2.31 (CH$_3$CH$_2$), 2.02 (CH$_3$), 5.45 (CH), 11.02 (COOH). ^{13}C NMR (25 °C, CD$_2$Cl$_2$, 62.9 MHz): δ = 8.4 - 9.8 (CH$_3$), 26.71 (CH$_3$C(O)) 28.22 - 30.25 (CH$_2$), 100.37 (C(O)CH), 178.51 - 183.85 (COOH) 183.99 (CH3C(O)) ppm.

Zr12VAC_acac: ^{1}H NMR (25 °C, CD$_2$Cl$_2$, 250 MHz): δ = 2.62 - 3.00 (CH$_2$), 4.90 - 5.09 (CH), 5.73 - 5.87 (=CH$_2$)1.96 (CH$_3$), 5.48 (CH), 10.95 (COOH). ^{13}C NMR (25 °C, CD$_2$Cl$_2$, 62.9 MHz): δ = 8.4 - 9.8 (CH$_3$), 27.48 (CH$_3$C(O)), 28.22 - 30.25 (CH$_2$), 101.26 (C(O)CH), 178.51 - 183.85 (COOH), 184.87 (CH$_3$C(O)) ppm.

Table 4.2: Comparison of bond length and angles of clusters **Zr12VAC_acac** and **Zr12VAC**.

Bond lengths [pm]	Zr12VAC_acac	Zr12VAC	Bond angles [°]	Zr12VAC_acac	Zr12VAC
Zr6-O10	217.1(1)	225.2(3)	O26-Zr6-O10	73.77(9)	56.47(9)
Zr6-O26	218.8(4)	230.9(6)	O10-Zr6-O4	74.90(6)	82.06(4)
Zr6-O4	224.5(6)	221.3(3)	O26-Zr6-O7	75.35(1)	80.72(3)
Zr6-O5	211.6(9)	209.3(5)	O9-Zr5-O31	55.93(8)	56.61(6)
Zr5-O9	227.9(8)	230.0(9)	O9-Zr5-O4	82.22(1)	79.64(3)
Zr5-O31	230.1(9)	227.3(7)	O31-Zr5-O5	84.94(6)	87.23(8)

Table 4.3: Crystal data and refinement details for **ZrPiv**.

	ZrPiv
Emp. formula	$C_{64}H_{116}O_{27}Zr_4$
M_r	1682.45
Crystal system	Triclinic
Space group	P-1
a, pm	1419.4(5)
b, pm	1484.4(6)
c, pm	2244.6(8)
α, deg	95.733(6)
β, deg	103.482(5)
γ, deg	115.756(4)
V, $pm^3 \cdot 10^6$	4031.3
Z	2
D_x, $Mg \cdot m^{-3}$	1.385
μ , mm^{-1}	0.574
Crystal size, mm	0.35 x 0.25 x 0.13
No. measured refl.	21489
Obs. refl. [I >2 σ (I)]	8100
θ^{max}, deg	25.22
R[F^2 >2 σ (F)], wR(F^2), S	0.0572, 0.1793, 0.902
Refl./param.	14345 / 1428
Weighting scheme [a]	$w = 1 / [\ \sigma^2(F_0{}^2) + (0.1048P)^2 + 0P]$
$\delta \rho_{max,min}$, e $\cdot 10^{-6}$ pm^{-3}	0.981, -0.734

[a] $P = (F_0{}^2 + 2F_c{}^2)/3$

Table 4.4: Crystal data and refinement details for **Ti2Zr4** and **Zr12VAC_acac**.

	Ti2Zr4	Zr12VAC_acac
Emp. formula	$C_{64}H_{80}O_{36}Ti_2Zr_4$	$C_{122}H_{158}O_{76}Zr_{12}$
M_r	1885.96	3935.12
Crystal system	Triclinic	Triclinic
Space group	P-1	P-1
a, pm	1079.2(5)	1409.5(1)
b, pm	1110.3(2)	1429.4(5)
c, pm	1656.4(2)	2012.0(9)
α, deg	101.58(9)	98.8(1)
β, deg	96.224(2)	95.5(7)
γ, deg	96.154(2)	99.8(2)
V, $pm^3 \cdot 10^6$	1915.9	3915.6
Z	1	1
D_x, $Mg \cdot m^{-3}$	1.635	1.669
μ, mm^{-1}	0.812	0.858
Crystal size, mm	0.6x0.5x0.4	0.4x0.3x0.2
No. measured refl.	53061	100555
Obs. refl. [I $>$2 σ (I)]	4903	10870
θ^{max}, deg	25.09	25.41
R[$F^2 >$2 σ (F)], wR(F^2), S	0.0457, 0.1369, 1.088	0.0731, 0.2195, 1.036
Refl./param.	6790 / 486	14397 / 903
Weighting scheme [a]	w =1 /[$\sigma^2(F_0^2)$+(0.0665P)^2 + + 4.3097P]	w =1 /[$\sigma^2(F_0^2)$+(0.0950P)^2 + + 39.6146P]
$\delta\rho_{max,min}$, e $\cdot$ 10^{-6} pm^{-3}	1.607, -1.260	1.614, -1.624

[a] $P = (F_0^2 + 2F_c^2)/3$

Chapter 5

Tuning the Properties of Cluster - Based Hybrid Materials

Tuning the Properties of Cluster - Based Hybrid Materials

5.1 Introduction

Co - polymerization of multifunctional transition metal oxo clusters with organic monomers results in the formation of strongly crosslinked polymers. The cluster thereby acts as crosslinker due to the high number of polymerizable ligands on the surface. This influences properties of the polymer. At the same time, the presence of the (inorganic) cluster in an organic matrix introduces so called filler effects. These effects stem from an interaction of the (inorganic) particles with the organic phase and change of the microstructure of the organic matrix. Filler effects are not easy to understand and depend on the type and composition of the inorganic and organic phase, the way how the inorganic filler is incorporated in the organic phase and the type, shape and size of the inorganic filler particles. These effects were exhaustively studied for silica - reinforced polymer systems and summarized in a review article.[154] Other commonly used inorganic filler compounds are TiO_2, ZrO_2 or Al_2O_3, which exhibit similar trends with respect to filler effects in nanocomposites.

Polyethylene naphthalate (PEN) reinforced with SiO_2 filler particles, for example, showed a reduced overall crystallization time and an increased degree of crystallization with increasing silica content.[155] Similar results were found for the system PP/silica, where SiO_2 nanoparticles were formed *in - situ* through a sol - gel process. DSC investigation showed that the *in - situ* formed particles act as nucleating agents and induce crystallization of the polymer.[156] Reinforcement of poly(ϵ - caprolactone) (PCL) with surface - modified TiO_2 nanoparticles as initiators had only a small effect on the crystalline structure of the PCL phase. However, increase of the TiO_2 loading resulted in an increase of the crystallization rate.[157] Non - isothermal crystallization behavior of poly(trimethylene terephthalate) (PTT) in presence of untreated and surface - treated TiO_2 nanoparticles was tested. The hybrid material with incorporated surface - modified TiO_2

particles had a higher crystallization temperature than hybrid materials with incorporated un-modified particles. However, the degree of crystallization was higher in case of the untreated particles. Both types, treated and untreated nanoparticles act as nucleating agents in the PTT matrix. [158]

The effect of filler particles on the crystallinity of the organic matrix can be explained by parti-cle‑induced crystallization under non‑isothermal crystallization conditions. The result is a shift of the crystallization temperature to higher temperatures which indicates that the supercooling of the polymer at a given cooling rate was reduced. [154]

One of the main reasons for using fillers as additives in composite formulations are reinforcement effects on mechanical properties. This includes the maximum stress which a material can with-stand upon stretching or pulling a test specimen (tensile strength), the ability of a material to absorb shock or impact energy without breaking (impact strength), the ability to resist deforma-tion under load (flexural strength), hardness and the ability of a material to withstand fracture (fracture strength).

Isotactic polypropylene (iPP), for example, was blended with surface‑modified and unmodified SiO_2 nanoparticles and showed improvement of mechanical properties such as tensile and impact strength as well as elongation at break, up to a filler content of 2.5 wt%. Increasing the filler load-ing over 2.5 wt% resulted in decreasing mechanical properties. [159] A similar result was found for silica‑reinforced polyimide which was produced through sol‑gel process. It was found that the Young's modulus, tensile strength and elongation at break increased linearly with the silica loading up to 10 wt%. Exceeding 10 wt% loading resulted in a decrease of tensile strength and elongation at break. Nevertheless, improved mechanical properties were found up to a loading of 20 wt% in cases where a coupling agent was used in the same system. The coupling agent, a diol functionalized silane, was used as precursor in the sol‑gel process. The diol functions of the silica phase thereby underwent hydrogen bonding to the PI network and provided a better in-terface contact between the PI network and the silica nanoparticles. [160] Mechanical properties of epoxy / TiO_2 composites were investigated and showed an increase of flexural strength and impact strength up to a concentration of 3 wt%. The mechanical properties decreased above this critical point. [161] Reinforcement of polyphenylenesulphide (PPS) with TiO_2 nanoparticles re-sulted in increased flexural strength (up to 10 wt% TiO_2) and increased storage and loss modulus up to 25 wt% [162] Blending of high density polyethylene (HDPE) with TiO_2 particles resulted in increased bending strength, yield strength, Young's modulus and compressive strength, when compared to the neat polymer, up to a filler content of 50 wt% [163] Incorporation of surface-

capped SiO_2 particles or ZrO_2 nanoparticles in epoxy resin showed an increase in storage modulus at room temperature. This increase was more distinct for the SiO_2 particles than for the ZrO_2 nanoparticles and was attributed to the size of the filler rather than to the filler type. The smaller ZrO_2 nanoparticles were better distributed in the polymer but showed only a small effect on the modulus. This behavior changed when the modulus was measured in the rubbery region above T_g. Here the influence on the modulus was more pronounced for the smaller ZrO_2 particles. Increasing the particle content showed an increase of hardness in all samples. [164]

Filler effects on thermal properties were widely investigated. This includes thermal degradation temperature (T_d), the temperature dependent behavior of storage modulus (E') and loss modulus (E") and tan δ (tan δ = E"/E'), whose maximum correlates with T_g. Reinforced composites showed generally an increase in the thermal degradation temperature. Exceptions (see e.g. [164] [165] [166]) are scarce. Coupling agent - modified nanoparticles (see e.g. [160]) showed in general a slightly decreased T_d when compared to unmodified nanoparticle reinforced composites, but still an increased T_d when compared to the neat polymer.

Reinforcement effects on T_g are more complicated. Depending on the system, T_g can either increase (e.g. [160]) or decrease(e.g. [164]). Besides the system, other effects such as filler size, loading and dispersion show an effect on T_g. [167] This is reflected in the fact that nanocomposites can show an increase [168] [160] or a decrease of T_g [156] [169] by increasing the filler loading. Furthermore, an initial increase of T_g with a decrease after exceeding a certain loading threshold [167] [170], the reverse, an initial decrease with an increase at higher loadings [171], no impact of the filler on the T_g at all [168] [172] or the disappearance of T_g [165] was observed. [154]

As stated above, surface - modified filler particles with polymerizable surface groups led to crosslinking of the composite and thus introduce a second effect on the materials properties. Crosslinking always increases T_g of the polymer. [173] [174] This can be explained by higher immobilization of polymer segments upon a higher crosslinking degree. Therefore, a higher energy uptake is necessary to induce mobility in the polymer chains, which is reflected in an increase of T_g. The shift of T_g thereby is not independent on the chemical system. Increasing the amount of crosslinker in the polymer system changes the composition of the polymer and introduces an additional copolymer effect. [175] This complicates the matter, since the copolymer effect can either increase or decrease T_g, depending on the system.

The effect of crosslinking on the modulus can be seen at temperatures above the damping peak of tan δ (which corresponds to T_g) in the rubbery region by an increase of the modulus. The

material is rigid at temperatures below the damping peak and crosslinking does not show an effect on the modulus. [176] The damping peak in crosslinked samples is shifted to higher temperatures and is often broadened, mainly due to heterogeneities in the polymer network. Since T_g is a very sensitive parameter and depends on many influences of the system, the damping is a relative method to estimate the crosslinking density.

The gel point, which is defined as the transition from a liquid phase to a solid phase, is reached during polymerization reactions in much shorter time for crosslinked polymers. [177] This can be explained by a fast formation of a (infinite) polymer network in the presence of crosslinking agents. The gel point occurs, at least approximately, at the crossing point of the storage and loss moduli E' and E", which can be measured in rheology measurements. [178]

Regarding reinforcement of polymers with polymerizable nanoparticles or clusters, filler and crosslinking effects act together in a rather complicated way and determine the final properties of the composite. Effects can thereby be opposed to each other (e.g. increase of T_g due to crosslinking, but decrease of T_g due to filler effect), can overrule each other (e.g. a strongly crosslinked polymer will not show crystalline domains) or fortify each other (e.g. increase of modulus due to crosslinking and filler effects).

Crosslinking and filler effects in cluster reinforced hybrids were observed and described before. [150] [179] [180] [149] [148] Nevertheless a distinction of crosslinking and filler effects could not be achieved.

5.2 Results and Discussion

The methacrylate ligands of $Zr_4O_2(OMc)_{12}$ (**Zr4**) can be exchanged with pivalate ligands under retention of the cluster core to yield the cluster $Zr_4O_2(OPiv)_{12}$ (**ZrPiv**). Furthermore scrambling reactions between **Zr4** and **ZrPiv** allow to gradually change the number of functional groups on the cluster surface. This two reactions were described in chapter 4. The possibility to copolymerize clusters of the same core type but with varying number of polymerizable ligands allows to investigate crosslinking and filler effects independently.

In a first series, hybrid materials with increasing content of **Zr4** were prepared. Increasing the cluster loading resulted in an increased crosslinking density of the polymer. In a second series, clusters $Zr_4O_2(OOCR)_x(OOCR')_{12-x}$ with two different carboxylate ligands, namely polymerizable methacrylate and non-polymerizable pivalate ligands were employed. The cluster proportion in the hybrid material was kept constant, but the ratio of polymerizable and non-polymerizable ligands was gradually varied. Thus, the crosslinking density was varied independent on the cluster content. Comparison of both series sheds light on which properties of the hybrid materials are influenced by nanofiller and crosslinking effects, respectively.

Variation of the Zr4 proportion: The hybrid materials were prepared by photochemical polymerization of different amounts of **Zr4** (viz. 2, 5, 10 and 20 wt%) and 2-hydroxyethylmethacrylate (HEMA) in the presence of IRGACURE 2959 as initiator under the same conditions. HEMA was chosen as the base polymer because both the functionalized cluster **Zr4** and the non-functionalized cluster **ZrPiv** are sufficiently soluble in HEMA. The resulting hybrid materials were denoted as **2%ZrMc**, **5%ZrMc**, **10%ZrMc** and **20%ZrMc**, respectively. A cluster-free sample of HEMA, denoted as pHEMA, was prepared under the same conditions for comparison. No attempts were undertaken to achieve complete conversion, for example by step-polymerization [79], because the goal of this work was to compare the influence of the cluster loading on the crosslinking density and on the materials properties.

In-situ photorheometry is a powerful technique to monitor changes in mechanical properties during UV curing. [181] [182] The change of the storage (E') and loss (E") modulus as function of the irradiation time can be monitored while the sample undergoes a liquid-to-solid transition. Thereby the change of the moduli correlates with the polymerization rate, the degree of polymerization and the crosslinking density of the formed network. At the same time information on the double bond conversion (DBC) can be obtained when *in-situ* photorheometry is coupled with time resolved infrared spectroscopy. *In-situ* NIR-photorheometry was performed for pHEMA,

2%ZrMc, **5%ZrMc**, **10%ZrMc** and **20%ZrMc** (Fig. 5.2) to investigate effects of increasing cluster loading on E' and E".

Fig. 5.1 shows selected NIR spectra of HEMA during the polymerization. The change in the absorption at $6167\,cm^{-1}$ corresponds to the decrease of the double bond of HEMA during the polymerization reaction. The double bond conversion was calculated by comparing the integrals of the band at $6167\,cm^{-1}$ before (t=0s) and after (t=600s) the polymerization. DBC was in the range of 90% (pHEMA) - 70% (**20%ZrMc**) with a deviation of 2% (see Tab. 5.1). The samples pHEMA - **5%ZrMc** showed approximately the same values, while DBC decreased for the samples **10%ZrMc** and **20%ZrMc**. The decrease in DBC at higher cluster loading stems from the formation of cluster rich and cluster depleted domains during the polymerization. This was also evidenced by SAXS measurements and will be commented on below. The curves for DBC over time are shown in Fig. 5.2.
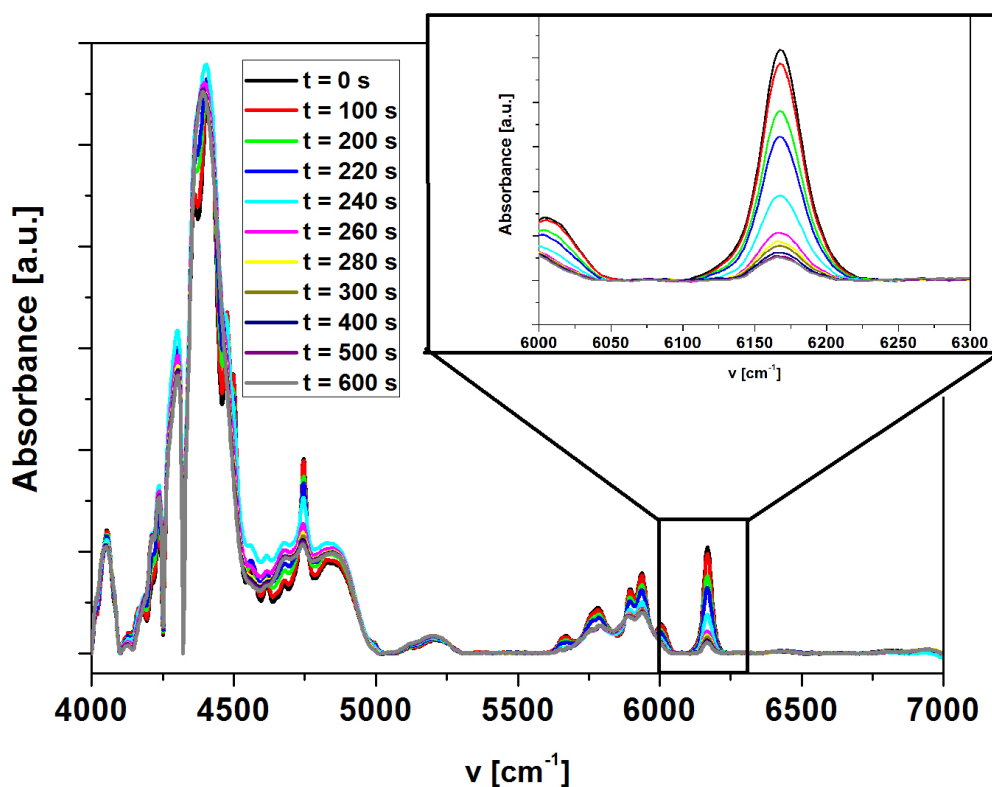
Figure 5.1: Selected time resolved NIR spectra for pHEMA and the hybrid materials **2%ZrMc - 20%ZrMc**.

A delay time with small E' and E" was observed after initiating the UV curing which correlates well with the amount of incorporated cluster. Increasing the cluster proportion corresponds to

increased crosslinking and results in faster network formation for 2 - 10 wt% cluster loading. A more pronounced shift of the polymerization onset would in principle be possible from **5%ZrMc** to **10%ZrMc** because the number of potential crosslinks is doubled. This, however, was not the case which is in good agreement with the observed decrease in the DBC.

The moduli increased rapidly until a plateau was reached. The slope of the curves during this increase was nearly the same for the samples pHEMA and **2%ZrMc - 10%ZrMc**. **20%ZrMc** was different and will be commented later. Upon reaching the plateau, a slight increase of the modulus was observed for **5%ZrMc** and **10%ZrMc** which corresponds to post - crosslinking reactions. The steep increase in modulus corresponds to the transition from the liquid monomer to the solid polymer and formation of the polymer network. The magnitude of E' and E" in rheological experiments is sensitive to molecular chain entanglements or the chain structure, such as network formation or branching. [183] Thus upon higher crosslinking densities at higher cluster loadings an increase of the final moduli of E' and E" is expected. However, rheology is not the most sensitive method to determine the magnitude of E' and E" and the change in the magnitude of E' and E" will therefore be discussed on the basis of the DMTA measurements below.

Storage and loss moduli for **20%ZrMc** were different: the delay time and the time to reach a plateau value were longer, and the slope of the curves was less steep. This is probably due to the increased number of cluster - bonded methacrylate ligands whose contribution to the polymerization reaction becomes increasingly dominant for high cluster loadings. Free movement of the methacrylate ligands is hampered which slows down the reaction rate. This is in agreement with the observed low DC values as discussed before. A decrease of the polymerization rate by high cluster loading was observed before for POSS - reinforced polymers. [184] [185]

The gel point (G_p) is defined as the intersection of E' and E" and reflects the point where individual polymer chains or network fragments join together to form one uniform network. High crosslinking of the polymer results in a decreased time to reach G_p. In the series pHEMA - **10%ZrMc** the time to reach G_p was decreased, which points to a stronger crosslinking due to increasing the amount of crosslinking clusters in the samples. The sample **20%ZrMc** shows an increased time to reach G_p which is in accordance with the lower DBC and slower polymerization rate.

SAXS measurements were carried out to investigate the cluster distribution in the polymer and covered a scattering vector range of q = 0.1 - 20 nm^{-1}. This wide range was used to normalize the
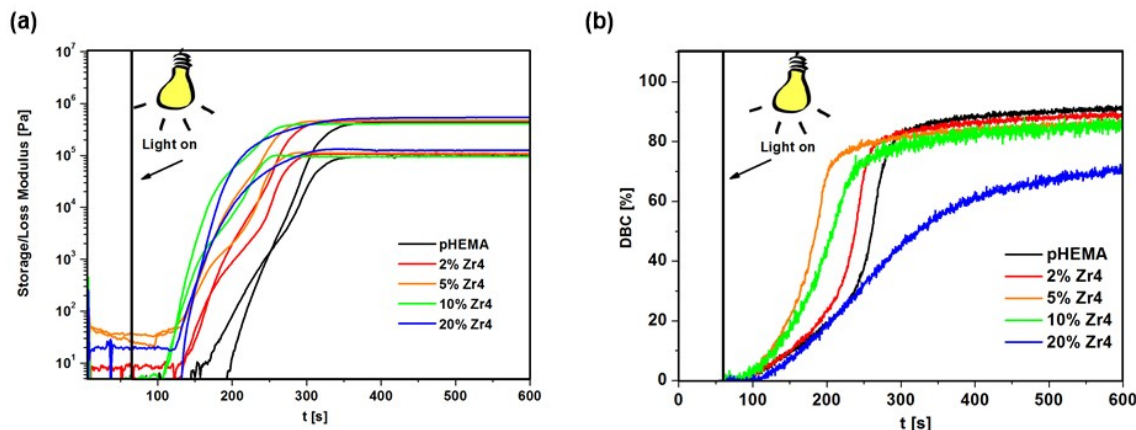
Figure 5.2: Double bond conversion (DBC) over time and time resolved photorheometry for pHEMA and the hybrid materials **2%ZrMc - 20%ZrMc**. Left: Change of storage (E') and loss modulus (E") over time; right: DBC over time.

scattering intensities using the short range order peak of the polymer at about $q = 12\,\text{nm}^{-1}$. The contribution of the polymer background was then subtracted to obtain structural information from the clusters alone.

All scattering curves showed two features, a broad short range order peak at about $q = 4\,\text{nm}^{-1}$ corresponding to the cluster - cluster distances and a broad shoulder or intensity increase towards low q - values. The latter is attributed to electron density differences between crosslinked domains and the pristine polymer. The model describing the scattering intensities therefore consists of two parts. The clusters are modelled as a Gaussian distribution of spheres with a radius R and a Gaussian half - width b. Since both values showed only small variations, they were kept constant at $R = 0.4\,\text{nm}$ and $b = 0.05\,\text{nm}$ to reduce the number of fit parameters. A hard sphere model was used for the interaction of the clusters, with a hard sphere radius R_{HS} and a hard sphere volume fraction η (Tab. 5.2). [186] The hard sphere volume fraction η is a measure for the probability to find a neighbouring cluster and thus characterizes the degree of agglomeration. $2R_{HS}$ is the typical distance between clusters. The size of the crosslinked domains is described by their radius of gyration R_g, and the Porod exponent p is a scaling factor, which characterizes their distribution. [187] Fitted SAXS scattering curves of the hybrid materials are shown in Fig. 5.3.

For all hybrid materials, the inter - cluster distance $2R_{HS}$ is nearly identical, and the Porod exponent p scatters around a value of two, which is typical for flexible polymers. Two significant trends were observed: In the series **2%ZrMc - 20%ZrMc**, the size of the crosslinked domains (R_g, see Tab. 5.2) increased strongly, whereas there was only a slight increase of the hard sphere

Table 5.1: Composition of the polymer formulation, degree of conversion (DBC), onset of thermal decomposition (T_{th}), T_g values, onset of polymerization (t_{pol}) and time to reach the gel point (t_{GP}). Initiator concentration 5 mg in each case.

	m (Cluster) [mg / mmol]	m (HEMA) [mg]	DBC [%]	T_d [°C]	T_g [°C]	onset of polymerization [s]	t_{GP} [s]
pHEMA		1000	91.3	205	112	184	185
2%ZrMc	20 / 0.014	980	88.9	314	113	137	106
5%ZrMc [a]	50 / 0.035	950	86.4	322	117	104	76
10%ZrMc	100 / 0.071	900	85.5	329	122	98	57
20%ZrMc	200 / 0.141	800	70.4	341	-	109	88
ZrMc [a]	50 / 0.035	950	86.4	322	118	104	76
Zr20	51 / 0.035	950	88.9	319	115	126	93
Zr40	53 / 0.035	950	87.1	324	112	128	112
Zr60	54 / 0.035	950	87.5	322	108	136	139
Zr80	55 / 0.035	950	90.4	319	104	145	157
ZrPiv	57 / 0.035	950	89.2	322	-	166	162

[a] **ZrMc = 5%ZrMc**

Table 5.2: Hard sphere volume radius R_{HS}, hard sphere volume fraction η, domain radius of gyration R_g and Porod scaling exponent p.

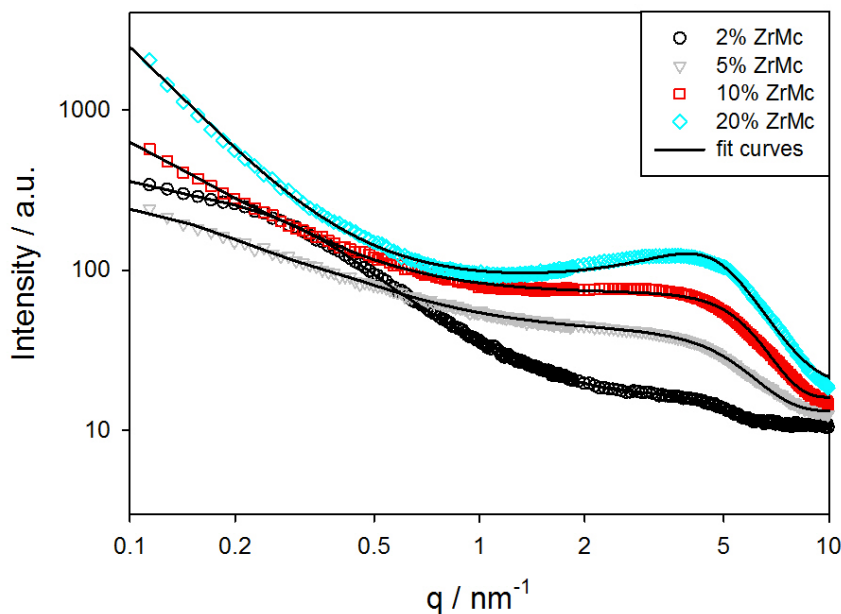|	R_{HS} [nm]	η	R_g [nm]	p
2%ZrMc	0.64	0.09	5	2.2
5%ZrMc [a]	0.51	0.08	10	1.6
10%ZrMc	0.50	0.12	15	1.9
20%ZrMc	0.60	0.15	> 30	2.3
ZrMc [a]	0.51	0.08	10	1.6
Zr20	0.60	0.15	5	2.1
Zr40	0.61	0.18	10	1.9
Zr60	0.59	0.20	10	1.8
Zr80	0.61	0.25	10	2.0
ZrPiv	0.60	0.29	16	2.3

[a] **ZrMc = 5%ZrMc**

Figure 5.3: SAXS intensities for hybrid materials **2%ZrMc‑20%ZrMc** and pHEMA. The symbols show the experimental intensities and the lines are fit curves.

volume fraction η. The relatively low value of η suggests that the clusters are homogeneously distributed within the domains even for **10%ZrMc** or **20%ZrMc** and only the size of the cross‑linked domains increases with increasing amount of cluster loading.

The onset of thermal decomposition (T_d) in cluster‑reinforced polymers is typically shifted to higher temperatures relative to the native polymer.[87][188][189][190] Comparison of the TGA for pHEMA and **2%ZrMc‑20%ZrMc** (Fig. 5.4) showed an increase of T_d with higher cluster loading. Incorporation of 2 wt% cluster increased T_d from 205 °C (for pristine pHEMA) to 314 °C. Further increase of cluster loading had only a minor influence on T_d which reached its maximum for the sample **20%ZrMc** (341 °C).

While only one degradation step was observed for pHEMA, the cluster‑reinforced hybrid materials show a second step at approximately 450 °C. This was observed before for cluster‑reinforced polymers [190][75] and was attributed to char formation and subsequent degradation of the char (second step at approximately 450 °C). Char formation depends mainly on the degree of crosslinking and increases with increased crosslinking.[191] When the cluster loading in pHEMA was increased, the temperature of the second onset remained unchanged, the wt% loss, however, increased from **2%ZrMc** to **20%ZrMc**.

Filler effects on T_g are difficult to predict and very different effects were observed.[170] Dynamic
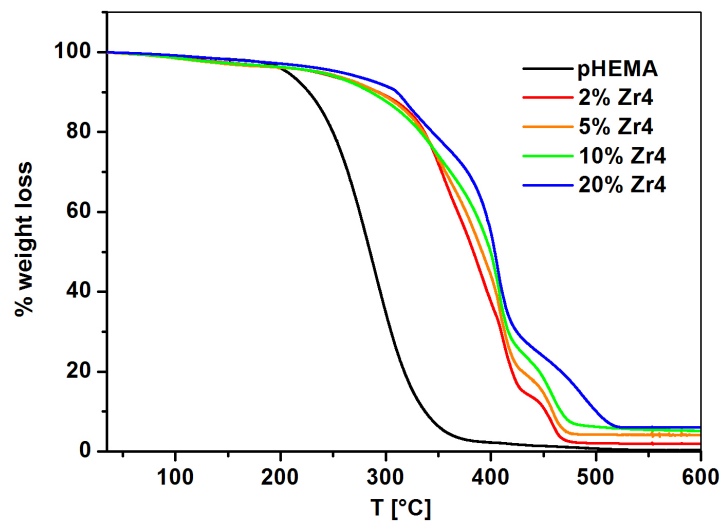
Figure 5.4: TGA traces for the hybrid materials **2%ZrMc - 20%ZrMc** and pHEMA.

mechanical thermoanalysis (DMTA) is a sensitive method to determine T_g. The tan δ curves of the DMTA measurements for pHEMA, **2%ZrMc**, **5%ZrMc** and **10%ZrMc** are shown in Fig. 5.5 The sample **20%ZrMc** was too brittle to obtain meaningful data and was therefore omitted in the following discussion. Incorporation of 2 wt% of cluster in the polymer decreased T_g from 76 ℃ in cluster - free pHEMA to approximately 41 ℃. The cluster thus acts as plasticizer, which results in decrease of T_g.
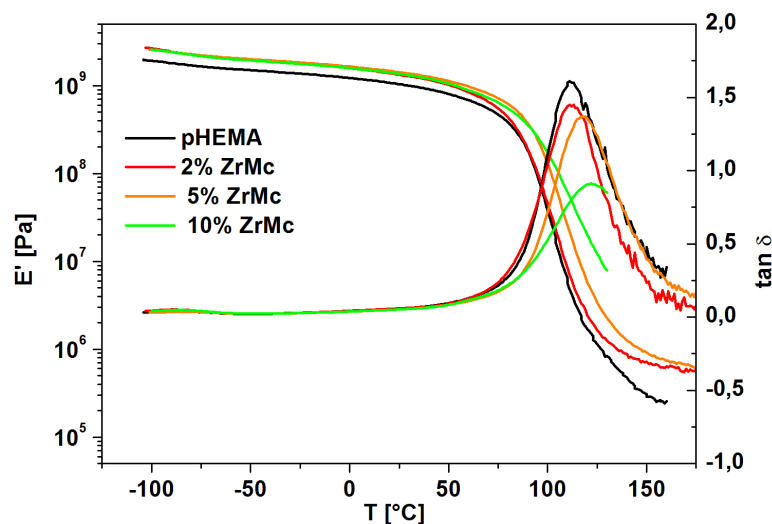
Figure 5.5: DMTA curves (tan δ and E') for the hybrid materials **2%ZrMc - 20%ZrMc** and pHEMA.

Increasing the cluster proportion in the hybrid material to 5% increased T_g. Increasing the cluster loading results in an increase of the crosslinking density of the polymer and thus higher tan δ and T_g values. The magnitude of tan δ reflects the ability of the polymer to dissipate energy. An increase in crosslinking density decreases the chain mobility of the polymer and results in smaller tan δ values. The restricted chain movement of crosslinked polymers is also the reason for an increase of T_g. Further increase of cluster loading to 10 wt% had, however, only a minor effect on the T_g. Doubling the number of potentially crosslinking groups from **5%ZrMc** to **10%ZrMc** should lead to a bigger shift of T_g. However, T_g is a very complex parameter and depends on the polymer structure, such as chain length and crosslinking density.

The storage modulus in the rubbery region is increased by increasing the cluster loading. This stems from an increased crosslinking of the samples.

The results of the first series, from the undoped polymer pHEMA to **20%ZrMc**, show that increasing the cluster proportion results in polymers with higher thermal stability and an increase of E' and E''. Incorporation of small amounts of cluster, however, results in a plasticizer effect on the polymer. Only when going to higher cluster loadings the crosslinking effect becomes more dominant. This is reflected in an increase of T_g and of E' and E''.

Variation of the crosslinking ability of the clusters: In the first series of hybrid polymers crosslinking density was increased by increasing the cluster proportion. Thus, the inorganic proportion of the materials (also acting as a nanofiller) and the crosslinking ability was increased at the same time. In a second series, samples with a constant cluster loading were prepared and the crosslinking ability was varied by varying the ratio of polymerizable and non‑polymerizable ligands attached to the same cluster core.

The mixed ligand clusters were prepared through scrambling reactions between **ZrPiv** and **Zr4** according to chapter 4. The ratio between reactive and unreactive ligands can be precisely tuned by this method through the employed stoichiometric ratio of both clusters. For example, a mixture of 20 mol% **ZrPiv** and 80 mol% **Zr4** leads to a cluster with the composition $Zr_4O_2(OMc)_{9.6}(OPiv)_{2.4}$.

Hybrid polymers were prepared from HEMA and $Zr_4O_2(OMc)_{12-x}(OPiv)_x$ under the same conditions as in the first series. The cluster loading, corresponding to the sample **5%ZrMc** from the first series, was kept constant within the second series. These polymer samples are denoted as **Zr20**, **Zr40**, **Zr60** and **Zr80** corresponding to the exchange of 20, 40, 60 and 80% of the

methacrylate ligands of **Zr4** with pivalate ligands. Furthermore, hybrid materials with **Zr4** and **ZrPiv** were prepared.

In-situ rheological measurements showed that the induction time as well as the time to reach G_p decreased continuously from **ZrMc** to **ZrX** and **ZrPiv** (see Fig. 5.6 and Tab. 5.1). The polymerization rate was similar for all samples as deduced from the slope of the change in the moduli. The final DBC values are the same within the error of 2%.
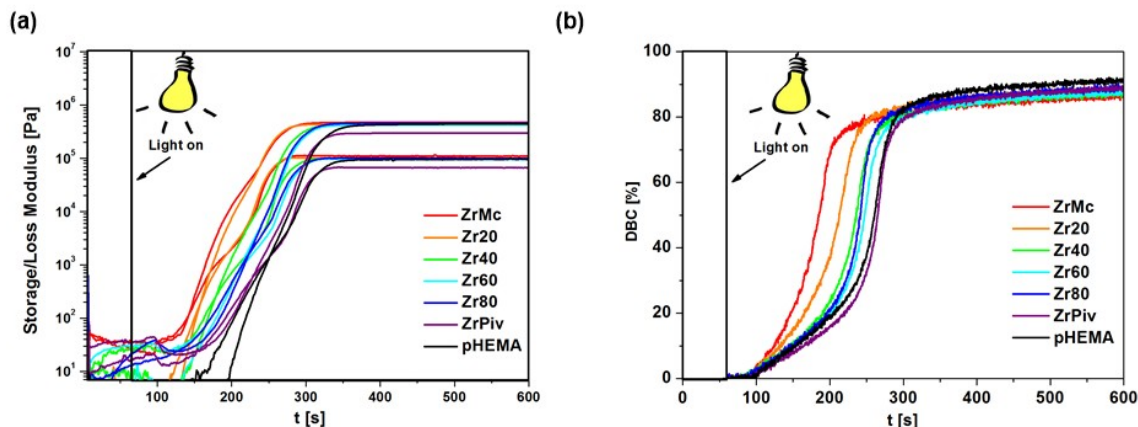

Figure 5.6: Double bond conversion (DBC) over time and time resolved photorheometry for pHEMA and the hybrid materials **ZrMc-ZrX-ZrPiv**. Left: Change of storage (E') and loss modulus (E") over time; right: DBC over time.

As for the samples of the first series, the typical cluster diameter 2R and the inter-cluster distance $(2R_{HS})$, obtained from SAXS measurements (see Fig. 5.7), were nearly constant at about $2R_{HS} = 1.2$ nm and $2R = 0.8$ nm, respectively, for the second series. Likewise, the Porod exponent was around two (see Tab. 5.2). In strong contrast to the first series, there was a strong increase of the hard sphere volume fraction η with decreasing number of methacrylate ligands per cluster. This, however, had nearly no effect on the size of the cross-linked domains (characterized by $2R_g$) which remained more or less constant. The exchange of methacrylate ligands leads to reduced crosslinking, which apparently resulted in an increased agglomeration tendency for the clusters, as indicated by the distinct and continuous increase of the hard sphere volume fraction η (see Tab. 5.2).

A test experiment was performed to verify that agglomeration occurs as a result of a reduced crosslinking density. A mixture of monofunctional HEMA and bifunctional ethoxylated bisphenol A diacrylate (BPA) was polymerized in the presence of the clusters **ZrX** (X = Mc, 20, 40, 60, 80, Piv). BPA thereby acts as weak crosslinker upon polymerization. The hard sphere volume
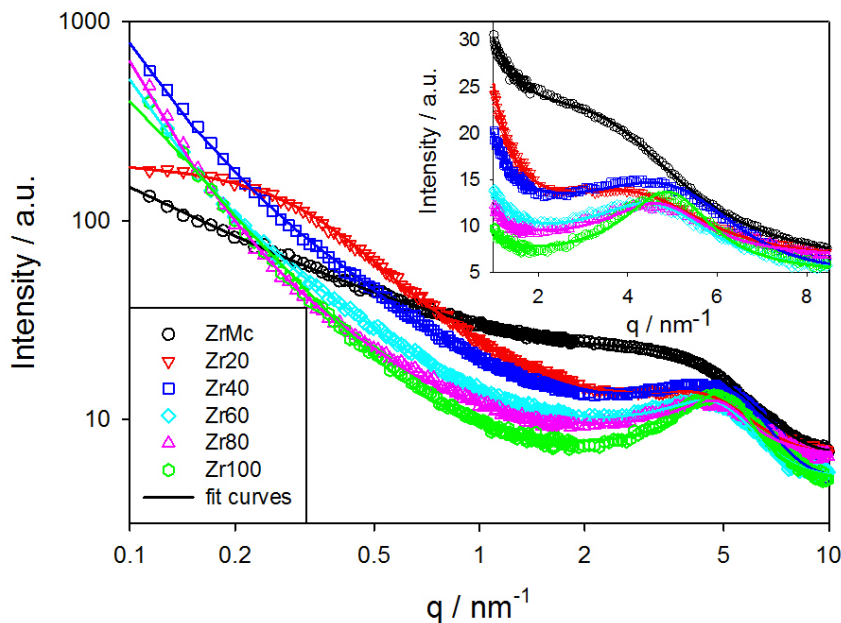
Figure 5.7: SAXS intensities for hybrid materials **ZrMc - ZrX - ZrPiv**. The symbols show experimental intensities and the lines are fir curves. The insert is an enlargement to visualize the increased degree of agglomeration (more pronounced short range order peak) with decreasing crosslinking density.

fraction values for the HEMA/BPA hybrid material showed uniform values comparable to the values of the ZrMc/HEMA hybrid materials (see Fig. 5.8). Agglomeration of the clusters is thus prevented by an organic crosslinker.

Thermal decomposition of the samples **ZrMc - ZrX - ZrPiv** (see Fig. 5.9) was nearly identical. An increase of the thermal decomposition temperatures compared to the cluster - free polymer pHEMA was observed (see Tab. 5.1). This increase is of the same magnitude as **5%ZrMc**, which has the same cluster loading as the samples of the second series. Likewise a second step at approximately 450 °C, attributed to char formation, was found for the **ZrMc - ZrX - ZrPiv** series. An effect of the varying crosslinking density was not observed, the second degradation step occurred approximately at the same temperature for all samples, including the non - crosslinked sample **ZrPiv**, and the weight loss was the same in all experiments. The second degradation step (char formation) is therefore due to the presence of clusters in the polymer (formation of an interphase around the clusters) and not due to crosslinking. This correlates well with an increased char formation upon increasing the cluster content in the first series (see Fig. 5.4).

DMTA curves for the samples of the second series are shown in Fig. 5.10. T_g decreased in the
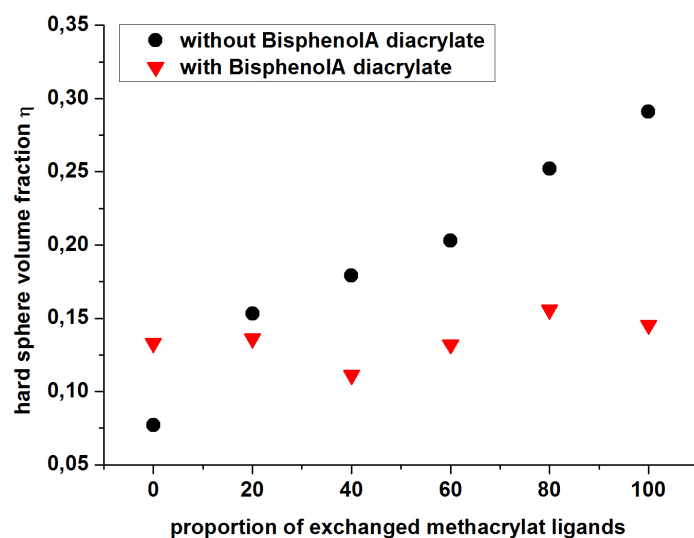
Figure 5.8: Dependence of the hard sphere volume fraction values (η) on crosslinking density for the cluster reinforced HEMA and for the HEMA/BPA polymer.
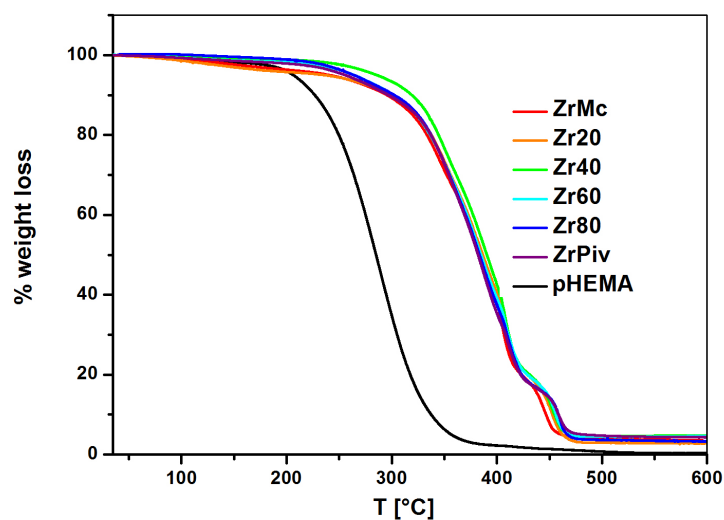

Figure 5.9: TGA traces for the hybrid materials **ZrMc - ZrX - ZrPiv** and the pristine polymer pHEMA.

series **pHEMA > ZrMc > Zr20 > Zr40 > Zr60 > Zr80** in agreement with an expected decreased crosslinking density in the hybrid materials. The sample **ZrPiv** was too brittle to obtain meaningful data.

Interestingly **Zr40** showed a T_g value close to that of the neat polymer and **Zr60** and **Zr80** a T_g value which is lower than that of pHEMA. This can be explained by a filler effect. Clusters

filling the free volume between the polymer chains enhance the movement of the polymer chains and reduce T_g (plasticizer effect). The fact that T_g decreased almost linearly by approximately 4°C steps from **ZrMc** to **Zr80** allows the conclusion that this decrease of T_g within the series of the cluster reinforced samples reflects the decrease in crosslinking density. A decrease of the crosslinking density also results in a decrease of E' and E" in the rubbery region.
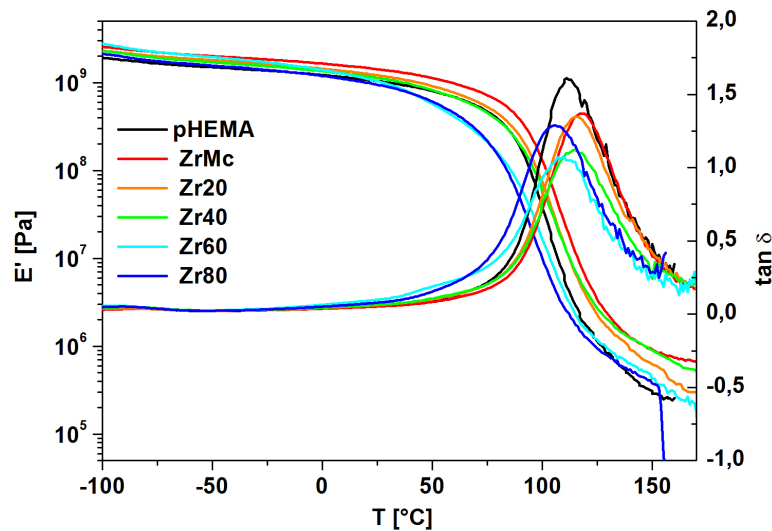
Figure 5.10: DMTA curves ($\tan\delta$ and E') for the hybrid materials **ZrMc - ZrX - ZrPiv** and the pristine polymer pHEMA.

Solvent uptake upon swelling of a polymer correlated well with the crosslinking density of the polymer. The mass swelling ratio $\Delta mt/\Delta mw$ decreased from pHEMA to **ZrMc** according to the change in crosslinking density (see Fig. 5.11). It is worth noting, however, that swelling roughly correlated with the crosslinking density only from **ZrMc** to **Zr80**, while that of the non - crosslinked cluster - doped polymer **ZrPiv** was much higher and in a comparable range to that of cluster - free pHEMA.
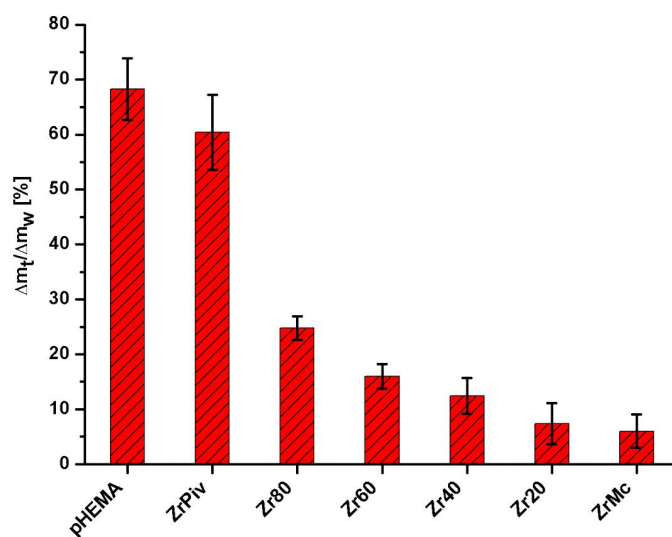
Figure 5.11: Degree of swelling for the hybrid materials **ZrMc - ZrX - ZrPiv**.

5.3 Conclusions

The properties of cluster-based hybrid materials are influenced, among others, by the proportion of cluster in the polymer, the type of cluster, nanofiller effects and dispersion of the clusters in the polymer. In previous studies on the structure and properties of transition metal oxo cluster-based hybrid materials, only the amount of cluster was systematically varied. This means that the proportion of the clusters as inorganic building blocks (also acting as nanofiller) and the number of potential crosslinking sites was varied at the same time. The used clusters were strongly crosslinking due to the great number of polymerizable ligands per cluster. In the current work crosslinking and nanofiller effects were to some extent separated by varying the number of polymerizable ligands of the same cluster while keeping the cluster proportion in the polymer constant (series 2). The properties of the thus obtained hybrid polymers allow a comparison with hybrid materials containing different proportions of the same cluster with only polymerizable ligands (series 1). The cluster proportion of series 1 was kept at a level where major agglomeration can be ruled out according to SAXS investigations.

Photochemical polymerization was performed under identical conditions for both series. The degree of conversion (DC) of the double bonds was ca. 70-75 % up to a cluster loading of 5 wt% and did not depend on the number of polymerizable groups per cluster. For higher cluster loadings (in series 1) the DC decreased. In situ rheology measurements showed clearly that the delay time for the polymerization onset as well as the storage (E') and loss modulus (E") after polymerization correlates well with crosslinking by the clusters. Both the delay time and the moduli increased with either increasing cluster proportions (series 1) or an increasing number of polymerizable groups per cluster (series 2). A plasticizer effect was observed for low cluster proportions (2 wt%). The sample containing 20 wt% cluster showed a different polymerization behavior probably due to the increased contribution of cluster-bonded methacrylate ligands, whose free movement is hindered.

The cluster dispersion, studied by SAXS, showed clear differences between both series of hybrid polymers. In the first series (variation of the cluster proportion) the clusters were homogeneously distributed in the polymer and the size of cluster-crosslinked domains increased when the cluster loading was increased. In series 2, however, an increasing agglomeration tendency of the clusters was observed when the number of polymerizable ligands per cluster was decreased.

The onset of thermal decomposition in the hybrid polymers was generally increased compared to cluster-free pHEMA. The amount of incorporated cluster (series 1) and the number of poly-

merizable ligands per cluster (series 2) showed little influence on the thermal decomposition. We therefore conclude that the onset temperature is hardly affected by the crosslinking density and that the increased thermal stability is a filler effect. Investigation of other cluster-crosslinked polymers came to the same conclusion.[190] A second degradation step in the TGA traces was reported before and was traced back to char formation. Increasing the cluster loading increased the wt% loss of this second step. The second degradation step in series 2 was nearly independent of the number of polymerizable ligands. Char formation can therefore clearly be traced back to the cluster proportion in the polymer.

Incorporation of a small cluster proportion in the polymer decreased the glass transition temperature (T_g) compared to cluster-free pHEMA. When the cluster loading was increased, this effect, however, was over-compensated, and T_g shifted to higher temperatures. This is clearly a crosslinking effect, because decreasing the crosslinking in series 2 resulted in an increasing T_g shift to lower temperatures relative to pHEMA depending on the number of polymerizable ligands.

The swelling of the hybrid materials of the second series correlated well with crosslinking ability of the clusters.

5.4 Experimental

General methods: All operations involving the preparation and modification of the clusters were performed in nitrogen atmosphere using standard Schlenk techniques. Hexane and toluene were dried over Na/benzophenone prior to use. Dichloromethane was distilled over CaH_2. Methacrylic acid (99%) and pivalic acid were obtained from Sigma Aldrich and freshly distilled over P_2O_5 prior to use. 2 - Hydroxyethylmethacrylate (HEMA, 97%, Sigma Aldrich) was distilled over P_2O_5 at reduced pressure prior to use and kept under inert atmosphere. $Zr_4O_2(OMc)_{12}$ (**Zr4**) was prepared as previously reported.[188] Exchange of the methacrylate ligands of **Zr4** with pivalate ligands to obtain $Zr_4O_2(OPiv)_{12}$ (**ZrPiv**) and scrambling reactions between **Zr4** and **ZrPiv** were performed as described in the experimental section in chapter 4.

Preparation of the polymer samples: Polymer samples were prepared by photopolymerization in a UViTRON IntelliRay 600 UV chamber. The emitted wavelength spectrum was 400 - 580 nm at a measured total intensity of $\approx$ 100 mW cm^{-2} detected with an Ocean Optics USB 200+ spectrometer. Clusters were dissolved in the HEMA monomer (see Tab. 5.1 for the composition of the precursor mixture) under inert atmosphere until a clear solution was obtained (typically 30 min). Afterwards IRGACURE 2959 as initiator (5 mg per g monomer mixture) was dissolved in the sample and the solution was poured in a silicone mold ($5 \times 2 \times 40 \, mm^3$) and cured for 800 sec. Samples for the SAXS test experiment were prepared in the same way as described above. The clusters were dissolved in a 1:1 (w/w) mixture of HEMA and BPA.

Small - angle X - ray scattering (SAXS): Small - angle X - ray scattering experiments were performed at a laboratory X - ray source (Nanostar, Bruker AXS) equipped with a pinhole camera and with CuK$_\alpha$ radiation from a microfocus source (Incoatec, High Brilliance). The beam was monochromatized and collimated by Montel optics. X - ray patterns were recorded with a position sensitive area detector (VANTEC 2000) and radially averaged to obtain the scattering intensity in dependence on the scattering vector $q = (4\pi/\lambda) \sin\theta$, with 2θ being the scattering angle and $\lambda = 0.1542$ nm the x - ray wavelength. SAXS measurements were carried out at a sample to detector distance of 108 and 13 cm, respectively. The integrated scattering data were merged in the overlap to cover a q - range of 0.1 - 20 nm^{-1}. The first term in eq. 5.4 describes the crosslinked domains by the approach of Beaucage.[187] G and B are numerical prefactors, R$_g$ the radius of gyration and the Porod exponent p a scaling factor for the distribution of these structural units. The clusters themselves are modelled as a Gaussian distribution of spheres with a radius R and a Gaussian half - width b (for an analytical solution of the integral see ref. [192]). The

fits showed only a small variation of R and b. Therefore, both were kept constant at R = 0.4 nm and b = 0.05 nm to reduce the number of fit parameters. A hard sphere model was used for the interaction of clusters, with a hard sphere radius RHS and a hard sphere volume fraction η. [186] C is again a numerical prefactor and the function F is defined in ref. [186].

$$I(q) \propto G\,exp\left(\frac{-q^2 R_g^2}{3}\right) + B\left[\frac{(erf(qR_g/\sqrt{6}))^3}{q}\right]^p +$$

$$+ C\int_{r=0}^{\infty} dr\left(\frac{4\pi}{3}r^3\right)^2 exp\left(-\frac{1}{2}\frac{(r-R)^2}{b^2}\right)\left(3\frac{\sin(qr)-qr\cos(qr)}{(qr)^3}\right)^2 S(q)$$

$$\text{with } S(q) = \frac{1}{1 + 24\eta F(2qR_{HS})/(2qR_{HS})}$$

$$(5.1)$$

Thermogravimetric analysis (TGA) and Dynamic Mechanical Thermoanalysis (DMTA): TGA analysis was carried out using a NETZSCH TG 209 at a heating rate of 10 K min^{-1} under air. DMTA measurements were performed with an Anton Paar MCR 301, with a CTD 450 oven and a SRF 12 measuring system. Polymer specimens (5 x 3 x 30 mm) were tested in torsion mode with a frequency of 1 Hz and a strain of 0.1%. The temperature was increased from -100 to 150 °C with a heating rate of 5 K min^{-1}.

Photorheology: A plate‑to‑plate time‑resolved photorheometer (Anton-Paar MCR-301) with a P‑PTD 200/GL Peltier glass plate and a disposable PP25 measuring system was used. The experimental setup was reported previously. [193] UV light (Omnicure S2000, 320‑500 nm) was directed via a light guide through a glass plate to the underside of the sample. Light intensity at the cure surface was 40 mW cm^{-2} as determined with an Ocean Optics USB 2000+ spectrometer. The monomer/initiator mixture was placed between the two plates of the rheometer. After a 60s dark period, the UV lamp was switched on. Real‑time measurements were made in oscillation mode at 25 °C, 1% strain, 10 Hz and 100 μm thickness. For the NIR measurements, the rheometer is additionally coupled with a Bruker Vertex 80 FTIR spectrometer equipped with a NIR light source, CaF$_2$ beam splitter and external mirrors to guide the IR beam through the sample beeing analyzed by rheology. The IR beam passes through a glass plate holding the sample and is reflected by the PP25 measuring system and guided to the external MCT‑detector. The IR chamber was continuously purged with dry air.

Swellability: Polymer samples (3 specimens per sample) were placed in ethanol and stored for 7 d. Ethanol was replaced after the first, the second and the third day. The samples were dried with a paper towel, weighted, placed in a vacuum oven and dried at 50 ℃ until constant weight was reached.

Chapter 6

Nanostructured Functional Hybrid Materials Fabricated by Stimulated Emission Depletion

Nanostructured Functional Hybrid Materials Fabricated by Stimulated Emission Depletion

6.1 Introduction

The fabrication of complex structures on a nanosized length scale is an important topic in materials science. The interest in miniaturization of complex structures is especially promoted by electronics industry which follows Moore's law [194], as well as by the aim to use nanostructured materials to mimik the physiology of tissues. [195]

Far-field photolithography is a powerful tool for fabrication of millimeter to nanometer-sized three-dimensional structures and opens possibilities, such as fabrication of photonic crystals or cell scaffolding. [196] [197] In photolithography, a laser beam is typically focused in the resin and starts locally a free-radical photopolymerization. The exposed volume of the photoresin is thereby restricted to the focal point of the laser beam. Three-dimensional direct laser writing (3D DLW) became commercially available and structures with a lateral resolution of 100 nm are routinely achievable.

However, Abbe's resolution limit states that the achievable resolution depends on the wavelength of the used light. Resolution in lithography can be thus enhanced by using light sources with short wavelengths, such as deep UV (DUV), extreme UV (EUV) or electron beam (EBL).

In the 90ies it was shown that Stimulated Emission Depletion (STED) lithography can theoretically overcome Abbe's resolution limit. The concept behind the STED technique is the excitation of a photoinitiator by a laser beam while a second laser beam depletes the photoinitiator in the outer rim of the point spread function (PFS) and inhibits a polymerization reaction. Thus the excitation volume is confined by the depletion laser and is not limited by the wavelength of the initiating laser anymore. In theory, this technique allows for unlimited small structures. In reality, structures with a lateral width of 55 nm and resolution of 120 nm were realized. [198] The

effective resolution is limited by the materials properties. In fact, only acrylate - based resins in combination with 7-diethylamino-3-thenoylcoumarin (DETC) as photoinitiating system showed a STED effect in lithography. Thus, there is an interest in the development of new resins with extraordinary stability after polymerization, which can be used in STED lithography.

A second trend in nanostructuring focuses on surface functionalization of structured materials. [199] [200] [201] Surface functionalization allows altering polymer properties as well as the fabrication of materials with multiple properties. [193] Amongst others, functionalized polymers were applied in the fabrication of reactive hydrogels [195] [202] or reactive thiol-ene structures [203] which are capable to bind proteins or metals. These materials were applied in advanced opto-electronic and sensor devices [204] [205] or were used as cell culture matrices. [206]

While most of the lithographically derived structures are based on organic resins, only few reports on cluster - based structures exist. A tin oxo cluster - based photoresist was reported and applied in EUV direct laser writing. [194] While one - dimensional lines with a width of 18 nm were obtained in this example, micrometer - sized three - dimensional structures were reported by DLW in a POSS - based resin lately. [207] [208] Nevertheless, no examples on STED derived hybrid materials are reported in literature so far.

In the following, the fabrication of cluster - based three - dimensional structures by means of multiphoton- and STED lithography will be reported. The clusters have a mixed ligand sphere with a methacrylate functionality for covalent bonding to the polymer and additionally a mercapto functionality. This mercapto function remains active after the lithographic process and can be used for further chemical reactions on the surface of the nanosized structures.

6.2 Results and Discussion

The first part of this study involves the doping of a photoresist typically used in STED-lithography with different concentrations of mercapto‑functionalized zirconium clusters and determination of the optimal excitation and depletion power. 13 % and 24 % of the methacrylate ligands of $Zr_4O_2(OMc)_{12}$ (**Zr4**) were exchanged with 3-mercapto propionate ligands as described in the experimental section. The samples are denoted as **Zr4_SH1** (13 % exchanged ligands) and **Zr4_SH2** (24 % exchanged ligands). The resin formulation is based on pentaerythritol triacrylate (PETA) (see Fig. 6.1 (c)) with 0.25 wt% DETC as photoinitiator. The clusters were dissolved in CH_2Cl_2 and mixed with PETA. The resin was accordingly drop‑cast on a coverslip and deposited in vacuum (100 mbar) at room temperature for 20 minutes to remove the solvent. PETA in combination with DETC was used before successfully in STED lithography. [206] [209]

Two types of lithographic techniques were applied in a first experiment. A pulsed excitation laser (780 nm) was used for two‑photon lithography. Thereby the resin polymerizes in the focus of the laser beam and line structures were achieved. In STED lithography a second donut‑shaped continuous wave (cw) laser beam (532 nm) was switched on. The photoinitiator in the outer sphere of the excitation laser was depleted which led to a decrease of the feature size (see Fig. 6.1 (a) for the setup of the STED experiment).
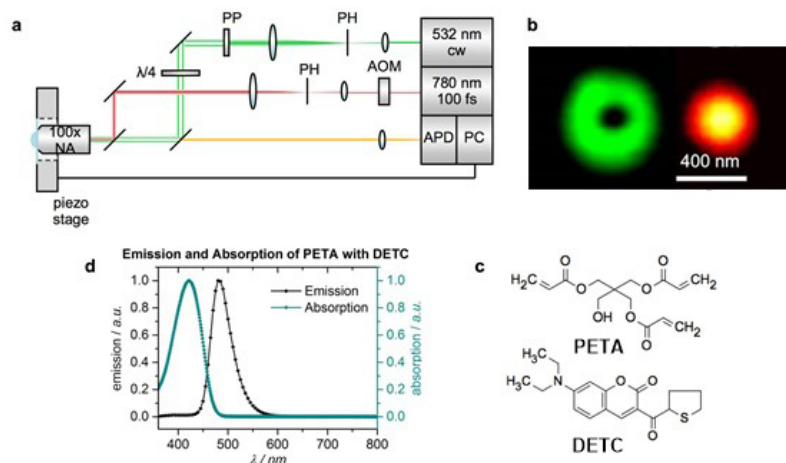
Figure 6.1: Setup of the STED experiment (a): green shows the depletion beam (532 nm, cw) and red the excitation beam (780 nm pulsed). The depletion beam is shaped into a donut form using a spiral phase plate. Abbreviations: Continuous wave (cw), acousto optic modulator (AOM), pin hole (PH), 2π spiral phase plate (PP), avalanche photo diode (APD), personal computer (PC). (b): Point spread function of the excitation laser (red) and the depletion laser (green). (c): Emission and absorption spectra of PETA and DETC photoresin. (d): Molecular structure of PETA and DETC.

Testing for the STED-effect was carried out by writing of so called "depletion patterns", which are shown in Fig. 6.2. These patterns are structured by means of different combinations of excitation and depletion powers. The lines in one column of the depletion pattern (see Fig. 6.2 (a)) were created with a constant excitation power and each line was written with different, increasing depletion powers. The height of the lines varied as these patterns were created by using two ordinary point-spread functions. This allowed plotting the feature height versus the depletion power and therefore comparison of the different photoresin with regard to their depletion efficiency. Depletion curves (see Fig. 6.2 (b)-(d)), plots of feature height versus the depletion power, were obtained from these patterns. Two-photon excitation powers of 3.2 mW and depletion powers of 7.8 mW were found to give the smallest feature size.
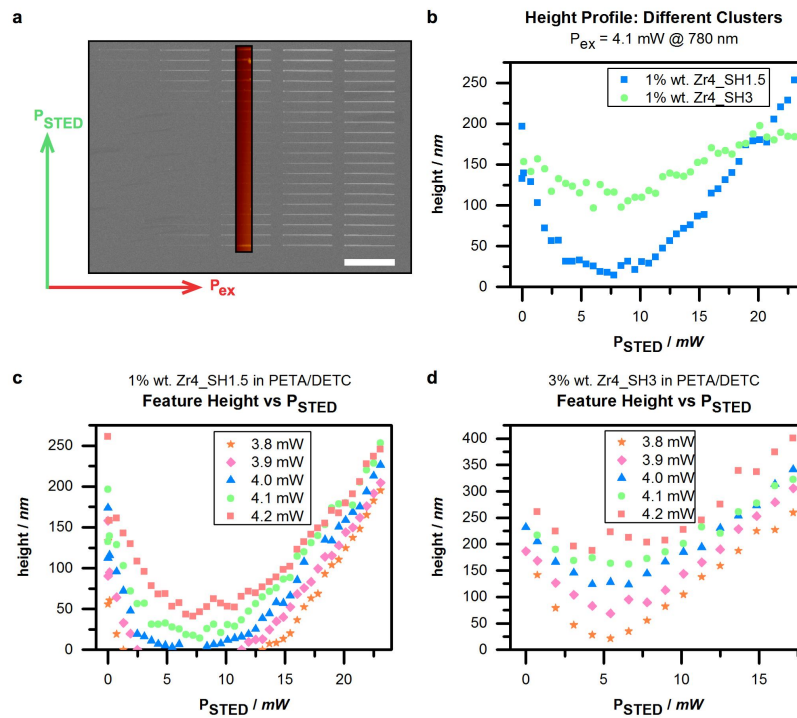
Figure 6.2: SEM and AFM (inset) images of the depletion patterns (a). Depletion curves for resin with different amounts of **Zr4_SH1** and **Zr4_SH2** (b)-(c).

A SEM image of a line written by 2-photon excitation and by STED lithography is shown in Fig. 6.3. 2-photon excitation (3.2 mW excitation power) gave a line with a width of 106 nm. The line width was reduced by 33 % by switching on the green depletion laser (7.8 mW depletion power) and had then a width of 72 nm. Thus, the presence of the clusters in the resin does not suppress the STED effect.
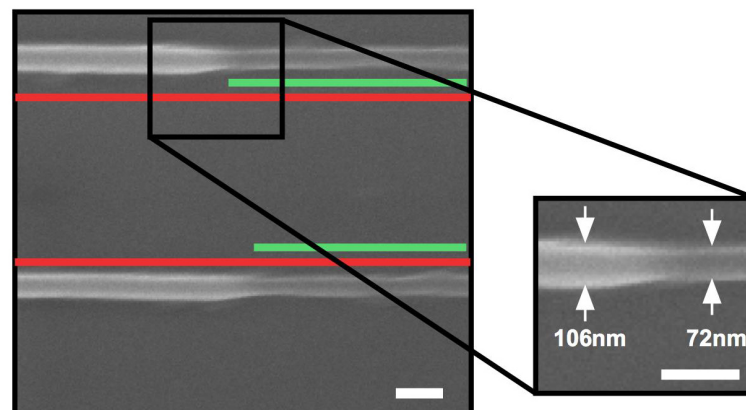
Figure 6.3: SEM image of a line written by 2-photon excitation (red line) and STED-induced reduction of the feature size (green line). Scale bar: 200 nm.

Based on the results of the depletion pattern experiment three-dimensional woodpile structures were written in PETA/DETC and PETA/DETC/1 wt% **Zr4** photoresins as SH-negative structures and in PETA/DETC/1 wt% **Zr4_SH2** photoresin as SH-positive structures. The reactivity of the mercapto groups after the lithography process was tested by covalent functionalization with Alexa647-maleimide. A sketch of the reaction is shown in Fig. 6.4.
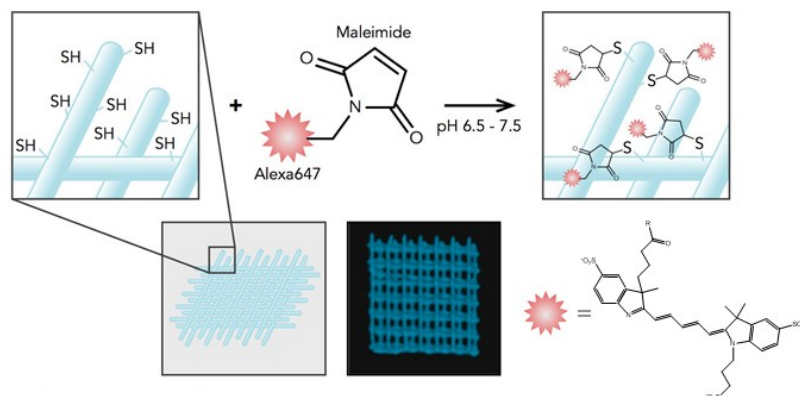
Figure 6.4: Sketch of the lithographically structured polymers, the incubation process with Alexa647-maleimide and confocal image of the woodpile structure.

Confocal laser scanning microscopy (LSM) images were used to compare the fluorophore-functionalized samples and the negative control (see Fig. 6.5). The grey bars represent the emission of DETC incorporated in the polymer. The fluorescence signal of DETC remained constant for all three structures. In contrast, the Alexa647-maleimide signal grew strongly when mercapto-functionalized cluster was incorporated in the polymer. The weak Alexa647-maleimide signal in the negative structures results from unspecific binding of the fluorophore on the surface of the structure. The 10-times increased signal for the mercapto-functionalized structure showed clearly that the mercapto groups were active after the lithography process and can be used for chemical reactions.
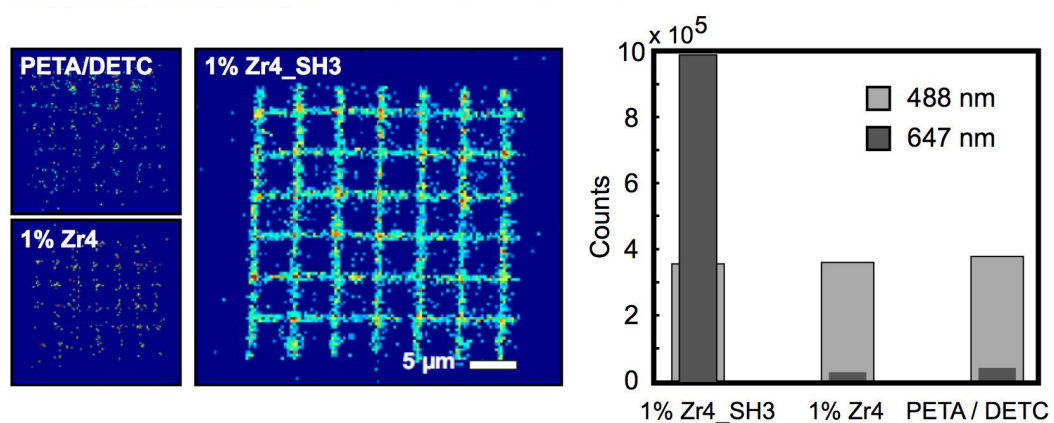
Figure 6.5: Confocal LSM images of the SH-negative woodpile structures (PETA/DETC and PETA/DETC/**Zr4**) and of the mercapto-functionalized woodpile structure (PETA/DETC/**Zr4_SH2**) after incubation. Right: Fluorescence signal intensity of DETC (grey bars) and of the fluorophore (blue bars) for the three structures.

6.3 Conclusions

A new cluster - based resin was developed and its performance in DLW and STED - lithography was tested. STED - effect was not suppressed up to a concentration of $3\,\mathrm{wt\%}$ of cluster in the monomer PETA. This was evidenced by writing depletion patterns and determining the height of the written lines at different levels of excitation and depletion powers. The STED - effect was tested by writing lines in the cluster - based resin by DLW and by switching on the depletion laser. STED induces a decrease of the line width by $33\,\%$. Three - dimensional structures were written in pure PETA, in PETA doped with $\mathrm{Zr_4O_2(OMc)_{12}}$ and in PETA doped with a bifunctional methacrylate / 3-mercaptopropionate cluster. Labeling of the structures with a fluorophore dye revealed that the mercapto functionalized structure shows enhanced fluorescence when compared to the non - mercapto functionalized structures.

6.4 Experimental

Lithography Setup: The two-photon polymerization initiators were excited with 780 nm ultra-short laser pulses (FemtoRay780, 50 MHz repetition rate, 100 fs pulse duration, Menlo Systems GmbH, Munich, Germany) and locally depleted at the outer rim of the point spread function with a depletion beam (532 nm, continuous wave, Verdi-V5, Coherent, Santa Clara, CA, USA). The 532 nm depletion beam was shaped into a donut form using a 2π spiral phase mask (RPC Photonics, Rochester, NY, USA) and a $\lambda/4$ plate converting the depletion beam into a circularly polarized beam with a handedness that matches the 2π spiral phase plate. The lasers were focused through an oil immersion objective lens (Zeiss α-plan Apochromat, 100x, numerical aperture NA = 1.46 oil immersion lens). Power adjustment of the excitation beam was provided by an acousto-optic modulator (Q1133, Isomet, Springfield, VA., USA). An avalanche photo diode (APD-SPCM-AQRH, PerkinElmer Optoelectronic Inc., Waltham, Massachusetts, USA) was used for adjusting the foci. A three axes piezo stage (P-562.3CD, Physik Instrumente PI, Karlsruhe, Germany) with a bidirectional positioning accuracy of 1 nm and a travel range of 200 x 200 x 200 μm, was used for sample motion. The high-precision stage was mounted on top of a coarse xy-motor stage (M-686.D64, Physik Instrumente PI, Karlsruhe, Germany) with a travel range of 25 x 25 mm. The stages were driven in closed loop with two controllers (E710.3CD and C-867.260, both from Physik Instrumente PI, Karlsruhe, Germany). For sample positioning, recording of images and controlling the writing process, a custom built LabView (LabView 2011, National Instruments Corporation, Austin, Texas, USA) program was used.

Confocal Laser Scanning Microscopy: Specific binding between Maleimide-Cy5 and a Wood-pile structure was quantified by a confocal laser scanning microscope LSM 700 (Carl Zeiss AG, Oberkochen, Germany). Images were taken using a 64x objective NA= 1.4 Oil DIC Plan-Apochromat. Generally, image sizes were 101.6 x 101.6 μm (line rate of 0.03 ms) by 3.6 μm (22 z-stacks). Samples were illuminated using 488 nm and 647 nm (Laser modules LSM 700) and after appropriate filtering, emitted signals were imaged on PMTs (Spectral Detection LSM 700). Zen data processing software (Carl Zeiss AG, Oberkochen, Germany) was used for image visualization, images were additionally analysed using MATLAB. The images were background corrected and detected signals were averaged for the analysis.

Combined Fluorescence Microscopy and Atomic Force Microscopy: The sample was sealed by a home-built chamber and rinsed with phosphate-buffered saline (PBS). AFM measurements were performed using a NanoWizard 3 (JPK Instruments AG, Berlin, Germany) sys-

tem mounted on an Axiovert 200 inverted microscope (Carl Zeiss AG, Oberkochen, Germany). The microscope was equipped with a 100x NA=1.45 oil-immersion Plan-Apochromat TIRFM objective (Olympus, Tokyo, Japan) and a 20x NA=0.8 Plan-Apochromat objective (Carl Zeiss AG, Oberkochen, Germany). Samples were illuminated in epifluorescence configuration via the epiport using 488 nm (250 mW) and 647 nm (250 mW) light from a diode laser (Toptica Photonics, Munich, Germany), or 532 nm light from a solid state laser (Millennia X, Spectra Physics, Mountain View, CA), with intensities of 3-10 kW cm^{-2}. The emitted signals were imaged on a back-illuminated, TE-cooled CCD-camera (Andor iXon Du-897 BV, Belfast, UK) after appropriate filtering. Acousto-optical modulators (1205C, Isomet, Springfield, VA, USA) for the 532 nm light were used for the precise control of the illumination timings. Diode lasers (488 nm and 647 nm) allowed direct modulation by means of TTL pulses. Timing protocols were generated by an in-house program package implemented in LABVIEW (National Instruments, Austin, TX, USA). Illumination times were adjusted to values between 1 and 5 ms. The sample surface was first imaged with the fluorescence microscope to determine an appropriate site for the force curve measurements. Topographical images and elasticity measurements were recorded in QITM mode (Quantitative Imaging mode) at room temperature in liquid (PBS) at a resolution of 128 x 128 pixels. The maximum force determined by the vertical deflection of the cantilever was set to 300 pN. Force distance cycles (scan rates) were controlled by the z length (250 nm), extension time (10 ms) and retraction time (50 ms). Uncoated silicon cantilevers (MSNL-10, Bruker Corporation, Billerica, USA) with a nominal spring constant in the range of 0.01-0.03 N m^{-1} were used. The spring constant for each cantilever was calibrated using the thermal noise method. JPK data processing (JPK Instrument, Berlin, Germany) software was used for image processing and estimation of the Young's Modulus. The height, adhesion and slope of the force curve were collected simultaneously in both trace and retrace directions. Height images were line-fitted as required. Isolated scan lines were occasionally removed. The Young's Modulus was estimated from force curve by using the JPK data processing software with the following settings: Model (cantilever tip): cone; opening angle (cantilever tip): 35°, Poisson ratio: 0.5; Method: Hertz Model.

General Methods: All operations which include the synthesis of the cluster and the ligand exchange reactions were performed under nitrogen atmosphere using standard Schlenk techniques. Hexane and toluene were dried over Na/benzophenone prior to use. Dichloromethane was distilled over CaH$_2$. All solvents were kept under nitrogen atmosphere over molecular sieve. Zr(OPr)$_4$ (70 wt% in 1-propanol) was purchased from Sigma Aldrich and used as received.

Methacrylic acid (99 %, Sigma Aldrich) and 3-mercaptopropionic acid (99 %, Sigma Aldrich) were freshly distilled over P_2O_5, when necessary under vacuum, prior to use. Pentaerythritol triacrylate (PETA, Sigma Aldrich) and diethylamino-3-thenoylcoumarin (DETC, Acros) were used as received.

NMR Spectroscopy: ^{1}H solution NMR spectra were recorded on a Bruker AVANCE 250 (250.13 MHz 1H, 62.86 MHz 13C). Gas-tight Young tubes were used for all experiments. CD_2Cl_2 was purchased from Euriso-Top and degassed by freeze-pump-thaw cycles, DCl (7.6 N in D_2O) and D_2O was purchased from Euriso-Top and used as received.

IR Spectroscopy: Solid state ATR-IR spectra were recorded on a Perkin Elmer Spectrum 400 FT-IR spectrometer equipped with a KBr window for MIR and a polyethylene window for FIR. 128 scans were averaged for MIR and 256 scans were averaged for FIR measurements.

Preparation of Zr4: The cluster was prepared as previously reported.[63] The crystalline product was dried under vacuum, dissolved in a small amount of CH_2Cl_2 until a clear solution was obtained and precipitated with hexane. This procedure was repeated three times to remove free acid.

Preparation of Zr4_SH1 and Zr4_SH2: In a typical experiment 200 mg **Zr4** (0.141 mmol, 1 eq.) was dissolved in 5 ml of CH_2Cl_2. 18.5 μl (0.212 mmol, 1.5 eq., **Zr4_SH1**) or 36.9 μl (0.423 mmol, 3 eq., **Zr4_SH2**) 3-mercaptopropionic acid were added and the reaction was stirred for 30 min. The solvent was removed afterwards, the white residue was dissolved in 1 ml of CH_2Cl_2 and precipitated from hexane. This procedure was repeated three times. The obtained product was washed three times with toluene and dried under vacuum. The intactness of the cluster was verified as described in chapter 4. NMR and IR spectra are shown in the appendix on page XXX - XXXI.

Zr4_SH1: ^{1}H NMR (25 °C, CD_2Cl_2, 250 MHz): $\delta = 1.29$ (SH), 1.87 (CH_3), 2.66 (-CH_2CH_2SH), 5.55 (=CH_2), 6.17 (=CH_2); ^{13}C NMR (25 °C, CD_2Cl_2, 62.9 MHz): $\delta = 17.64$ (-CH_3), 19.82 (CH_2-SH), 40.43 (CH_2), 126.79 (=CH_2), 138.09 (CH_3-C=CH_2); IR (ATR): $\nu = 3932$ (b), 2566 (w, SH), 1694 (s), 1589 (w), 1532 (s), 1419 (s), 1310 (s), 1283 (s), 1238 (s), 1204 (w), 1166 (m), 1099 (m), 1001 (s), 940 (s), 870 (s), 827 (s), 801 (w), 657 (w), 593 (w), 495 (w);

Zr4_SH2: ^{1}H NMR (25 °C, CD_2Cl_2, 250 MHz): $\delta = 1.29$ (SH), 1.87 (CH_3), 2.66 (-CH_2CH_2SH), 5.55 (=CH_2), 6.17 (=CH_2); ^{13}C NMR (25 °C, CD_2Cl_2, 62.9 MHz): $\delta = 17.64$ (-CH_3), 19.82 (CH_2-SH), 40.43 (CH_2), 126.79 (=CH_2), 138.09 (CH_3-C=CH_2); IR (ATR): $\nu = 2958$ (w), 2924 (w), 2573 (w, SH), 1691 (m), 1638 (m), 1585 (w), 1521 (s), 1412 (s), 1371 (m), 1310 (m), 1284 (w),

1242 (s), 1102 (w), 1001 (s), 940 (s), 876 (s), 827 (s), 797 (w), 729 (w), 661 (w), 601 (s), 499 (s);

Determination of the number of exchanged ligands: 50 mg of **Zr4_SH1** or **Zr4_SH2** was suspended in D_2O and 20 μl DCl was added. The solution was sonicated for 60 min before a ^{1}H NMR spectra was recorded. The ratio of methacrylate and mercapto-propionate ligands was determined according to the ratio of the integrals of the methyl group of methacrylic acid (1.65 ppm, 3H) and the -CH_2CH_2 signal of the mercaptopropionic acid (2.48 ppm, 4H) and was found to be 1:0.20 for **Zr4_SH1** and 1:0.42 for **Zr4_SH2**. Thus, 13 % of the methacrylate ligands were exchanged with mercapto propionate ligands in **Zr4_SH1** and 24 % were exchanged in **Zr4_SH2**. From this follows that the formula of **Zr4_SH1** is $Zr_4O_2(OMc)_{10.4}(OPrSH)_{1.6}$ and the molecular formula of **Zr4_SH2** is $Zr_4O_2(OMc)_{9.1}(OPrSH)_{2.9}$. The ^{1}H NMR spectra of the free acids after destroying the cluster are shown in the appendix on page XXXI.

Preparation of the photoresin: The photoresin was prepared by dissolving the initiator DETC (0.25 wt%) in the PETA monomer. For the preparation of the cluster based resins, the cluster was dissolved in absolute CH_2Cl_2 and mixed with the photoresin. The solvent was removed afterwards under vacuum.

Chapter 7

Summary

Summary

In this work ligand exchange reactions on transition metal oxo clusters were investigated and applied to synthesize clusters with a mixed ligand sphere. Although the focus of the work was on understanding the ligand exchange reactions, the obtained clusters were also employed in the fabrication of hybrid materials. Modification of the ligand sphere of the clusters on properties of the hybrid materials was investigated.

In the first part of this work DFT calculations were employed to calculate the binding energies of different carboxylate ligands and of the acetylacetonate ligand. In a first step, different basis sets and functionals were tested with respect to accurately describing the geometry and the vibrational modes of the cluster $Zr_4O_2(OMc)_{12}$ (OMc = methacrylate). Basis set size effects were observed. Increasing the basis set size by going from double–ζ quality to triple–ζ quality generally resulted in a better prediction of geometrical parameters and vibrational modes. Functional effects were observed when going from LDA via GGA and meta - GGA functionals to hybrid functionals: While LDA and pure GGA functionals calculated too short bond lengths, meta - GGA and including exact HF exchange resulted in better results. Especially an increasing amount of exact HF exchange showed an improvement of the predicted bond lengths and angles.

Interestingly, including HF exchange resulted in an overestimation of the vibrational modes, thus hybrid functionals failed to accurately reproduce the IR frequencies. Overall, the meta - GGA functional TPSS showed a balanced performance with respect to geometry parameters and vibrational modes and was the functional of choice for the calculation of the ligand binding energies.

A main question with respect to ligand exchange reactions is a possible site - selective exchange of the ligands on the cluster. This question can be tackled in different ways: First, ligands may be selectively exchanged according to possible differences in their ligand binding energies or to differences in the electronic structure of the ligands. Second, site - selective ligand exchange

may be achieved by exploiting different coordination behaviour of the ligands (e.g. chelating *vs.* bridging coordination).

Theory can give an answer at least to the first question. Ligand binding energies for a carboxylate ligand at different positions of the cluster $Zr_4O_2(OMc)_{12}$ were calculated and compared. Whilst the binding energies showed a difference with respect to the position on the cluster, these differences were too small to expect site-selective effects upon ligand exchange experiments. However, the ligand binding energy can be tuned by introducing substituents which alter the electronic structure of the ligand. Replacement of a chelating carboxylate ligand by an acetylacetonate ligand resulted in an increased binding energy of the latter. Employing chelating ligands in exchange reactions therefore might have a higher chance to achieve site selectivity.

The prediction of the theoretical results was confined by experiment. Ligand exchange of the cluster $Zr_4O_2(OMc)_{12}$ with an excess of pivalic acid resulted in complete exchange of the twelve methacrylate ligands. This reaction is reversible, thus by reaction of $Zr_4O_2(OPiv)_{12}$ (OPiv = pivalate) with an excess of methacrylic acid the original methacrylate cluster was obtained again. The retention of the cluster core during exchange and re-exchange was evidenced by two-dimensional NMR spectroscopy and by single crystal XRD. HMBC NMR spectra of $Zr_4O_2(OMc)_{12}$ at -80 ℃ showed a splitting in four sets of signals, which is in agreement with symmetry considerations. Thereby the signals of the chelating and bridging carboxylates were identified. Exchange of part of the methacrylate ligands with pivalate ligands resulted in HMBC spectra which showed overall the splitting in four signals for the methacrylate and the pivalate ligands each. Thus, exchange with carboxylic acids does not show any site-selective effect.

A different method to obtain mixed-ligand clusters is scrambling between two clusters of the same type, but with a different ligand sphere. This was demonstrated by scrambling reaction of $Zr_4O_2(OMc)_{12}$ and $Zr_4O_2(OPiv)_{12}$. To prove that the clusters undergo scrambling reactions, HMBC spectra of $Zr_4O_2(OMc)_6(OPiv)_6$ either obtained by carboxylic acid exchange or by scrambling reaction were compared. The peak pattern is essentially the same, and the existence of both ligands (methacrylate and pivalate) on the same cluster core was proven by NOESY NMR spectroscopy. The NOE effect is a short-range effect with an expansion of approximately 5Å. The splitting of the signals in the HMBC spectra, however, led to the conclusion that scrambling reactions are also not site selective.

As mentioned before, ligand exchange of only chelating ligands appears to be possible and thus to achieve site selectivity. Ligand exchange with acetylacetone was performed on two clusters. Upon

reaction with acetylacetone, the cluster $Ti_4Zr_4O_6(OBu)_4(OMc)_{16}$ partially degraded under formation of $Ti(OBu)_2(acac)_2$ and rearrangement to give the new cluster $Ti_2Zr_4O_4(OBu)_4(OMc)_{16}$. The formation of the complex was evidenced by mass spectroscopy, whilst the structure of the new cluster was elucidated by single crystal XRD. When the cluster $[Zr_6O_4(OH)_4(OOCR)_{12}]_2$ (OOCR = propionate or vinylacetate) was reacted with an excess of acetylacetone one of the three chelating ligands in $[Zr_6O_4(OH)_4(OOCR)_{12}]_2$ was exchanged to yield the cluster $[Zr_6O_4(OH)_4(OOCR)_{11}(acac)]_2$. The core of the cluster thereby remained intact.

Scrambling reactions are a facile synthetic route to mixed-ligand clusters. The stoichiometry of the ligand sphere is thereby solely determined by the ratio of the employed clusters. Thus the number of polymerizable and non-polymerizable ligands can be gradually adjusted. Polymerization of clusters differing in the amount of polymerizable ligands (thus differing in their crosslinking ability) led to hybrid materials with different crosslinking densities. Going from the fully functional cluster $Zr_4O_2(OMc)_{12}$ to the fully non-functionalized cluster $Zr_4O_2(OPiv)_{12}$ allowed for preparation of hybrid materials covering the region of strongly crosslinked Class II hybrid materials to non-crosslinked Class I hybrid materials. Besides the crosslinking effect on the materials properties, incorporation of clusters also introduces filler effects. Analysing the change in materials properties in two series of cluster-reinforced polymers allowed for separation of these two effects: In the first series, the amount of $Zr_4O_2(OMc)_{12}$ in the polymer was varied. Thus, by increasing the cluster loading more strongly crosslinked materials were obtained. At the same time the filler content increases by increasing the cluster loading. In the second series, the cluster loading remained the same. However, clusters with different proportions of polymerizable ligands were employed. Since the cluster loading is the same throughout the second series, only the crosslinking capability of the clusters changed. Materials properties such as T_g, thermal decomposition behaviour, mechanical properties (storage (E') and loss modulus (E")) and rheological properties during the polymerization were investigated and compared for both series. Thus gradually changing the composition of the ligand sphere allowed a gradual change in the materials properties (T_g, E' and E"). Thermal decomposition was only influenced by the amount of incorporated cluster, whilst changes in T_g, E' and E" were traced back to the crosslinking capability of the cluster.

A second application of ligand exchange reactions was demonstrated by the fabrication of functionalized nanostructures. Stimulated Emission Depletion (STED) lithography was employed for fabrication of these structures. Since only acrylate-based resins were employed in STED lithography, two main points were of interest: (I) Is it possible to develop a cluster-based resin

which does not suppress the STED effect? (II) is it possible to introduce functional groups in the structure which are able to undergo chemical reactions after the lithographic process?

A mixed‑ligand methacrylate/mercaptopropionate cluster was obtained by ligand exchange reactions of $Zr_4O_2(OMc)_{12}$ with 3‑mercaptopropionic acid. In a first experiment the effect of the cluster loading on the STED performance was tested. It was shown that up to a cluster loading of 3 wt% the STED effect was not suppressed by the cluster and allowed fabrication of lines with a 30% smaller width compared to two‑photon polymerization. In a second experiment three‑dimensional woodpile structures were fabricated in an acrylate‑based resin, in an acrylate‑based resin in the presence of $Zr_4O_2(OMc)_{12}$ and in an acrylate‑based resin in the presence of $Zr_4O_2(OMc)_9(OPrSH)_3$ (OPrSH = mercaptopropionate). The structures were incubated in a maleimide fluorophore dye solution. Investigation of the incubated structures with scanning laser microscopy revealed that the fluorescence intensity of the mercapto‑functionalized structure showed a ten‑fold enhancement when compared to the non‑functionalized structures. Thus, the mercapto groups remain active for chemical reactions after the lithographic process.

Bibliography

[1] L. L. Hench and J. K. West, *Chem. Rev.*, 1990, **90**, 33 – 72.

[2] P. J. Ollivier and T. E. Mallouk, *Chem. Mater.*, 1998, **10**, 2585 – 2587.

[3] J. Rouxel and M. Tournoux, *Solid State Ionics*, 1996, **84**, 141 – 149.

[4] J. Gopalakrishnan, *Chem. Mater.*, 1995, **7**, 1265 – 1275.

[5] J. Livage, *Chem. Mater.*, 1991, **3**, 578 – 593.

[6] J. Livage, M. Henry, and C. Sanchez, *Prog. Solid St. Chem.*, 1988, **18**, 259 – 341.

[7] U. Schubert and N. Hüsing, *Synthsis of Inorganic Materials*, Wiley-VCH, Weinheim, 3rd ed., 2012.

[8] E. J. A. Pope and J. D. Mackenzie, *J. noncryst. Sol.*, 1986, **87**, 185 – 198.

[9] J. A. Ibers, *Nature*, 1963, **197**, 686 – 687.

[10] D. C. Bradley and C. E. Holloway, *J. Chem. Soc. A*, 1968, **0**, 1316 – 1319.

[11] D. C. Bradley, R. C. Mehrota, and A. Rothwell, I. P. Singh, *Alkoxo and Aryloxo Derivatives of Metals*, Elsevier, Weinheim, 2001.

[12] G. D. Smith, C. N. Caughlan, and J. A. Campbell, *Inorg. Chem.*, 1972, **11**, 2989 – 2993.

[13] P. Toledaon, M. In, and C. Sanchez, *C. R. Acad. Sci., Paris Ser. II*, 1991, **313**, 12479 – 1253.

[14] P. Toledano, M. In, and C. Sanchez, *C. R. Acad. Sci., Paris Ser. II*, 1990, **311**, 1161 – 1172.

[15] C. Sanchez, M. In, P. Toledano, and P. Griesmar, *C. R. Acad. Sci., Paris Ser. II*, 1992, **271**, 669.

[16] J. V. Silvertin and J. L. Hoard, *Inorg. Chem.*, 1963, **2**, 243 – 249.

[17] S. Doeuff, Y. Dromzee, F. Taulelle, and C. Sanchez, *Inorg. Chem.*, 1989, **28**, 4439 − 4445.

[18] P. I. Laaziz, A. Larbot, C. Guizard, J. Durand, and L. Cot, *Acta Cryst. C*, 1990, **46**, 2332 − 2334.

[19] U. Schubert, E. Arpac, W. Glaubitt, A. Helmerich, and C. Chau, *Chem. Mater.*, 1992, **4**, 291 − 295.

[20] T. J. Boyle, T. M. Alam, and C. J. Tafoya, *Inorg. Chem.*, 1998, **37**, 5588 − 5594.

[21] U. Schubert, *J. Mater. Chem.*, 2005, **15**, 3701 − 3715.

[22] R. Papiernik, L. G. Hubert-Pfalzgraf, J. Vaissermann, and M. C. H. B. Goncalves, *J. Chem. Soc. Dalton Trans.*, 1998, **14**, 2285 − 2287.

[23] X. Lei, M. Shang, and T. P. Fehlner, *Organometallics*, 1997, **16**, 5289 − 5301.

[24] B. Moraru, G. Kickelbick, and U. Schubert, *Eur. J. Inorg. Chem*, 2001, **5**, 1295 − 1301.

[25] B. Moraru, S. Gross, G. Kickelbick, G. Trimmel, and U. Schubert, *Monatsh. Chem.*, 2001, **132**, 993 − 999.

[26] G. Kickelbick and U. Schubert, *Chem. Ber.*, 1997, **130**, 473 − 477.

[27] G. Kickelbick, D. Holzinger, C. Brick, G. Trimmel, and E. Moons, *Chem. Mater.*, 2002, **14**, 4382 − 4389.

[28] B. Moraru, N. Hüsing, G. Kickelbick, and U. Schubert, *Chem. Mater.*, 2002, **14**, 2732 − 2740.

[29] G. Kickelbick, P. Wiede, and U. Schubert, *Inorg. Chim. Acta*, 1999, **284**, 1 − 7.

[30] P. Piszczek, A. Radtke, A. Grodzicki, A. Wojtczak, and J. Chojnacki, *Polyhedron*, 2007, **26**, 679 − 685.

[31] M. Y. Reza, H. Matsushima, M. Koikawa, M. Nakashima, and T. Tokii, *Bull. Chem. Soc. Jpn.*, 1998, **71**, 155 − 160.

[32] G. Kickelbick and U. Schubert, *J. Chem. Soc. Dalton Trans.*, 1999, **8**, 1301 − 1305.

[33] M. Puchberger, F. R. Kogler, M. Jupa, S. Gross, H. Fric, G. Kickelbick, and U. Schubert, *Eur. J. Inorg. Chem*, 2006, **16**, 3283 − 3293.

[34] F. Faccini, H. Fric, U. Schubert, E. Wendel, O. Tsetsgee, K. Müller, H. Bertagnolli, A. Venzo, and S. Gross, *J. Mater. Chem.*, 2007, **17**, 3297 − 3307.

[35] A. Gross, G. Kickelbick, M. Puchberger, and U. Schubert, *Monatsh. Chem.*, 2003, **134**, 1053 – 1063.

[36] L. Armelao, C. Eisenmenger-Sittner, M. Groenewolt, S. Gross, C. Sada, U. Schubert, E. Tondello, and A. Zattin, *J. Mater. Chem.*, 2005, **15**, 1838 – 1848.

[37] M. Jupa, G. Kickelbick, and U. Schubert, *Eur. J. Inorg. Chem*, 2004, **9**, 1835 – 1839.

[38] L. Rozes, N. Steunou, G. Fornasieri, and C. Sanchez, *Monatsh. Chem.*, 2006, **137**, 501 – 528.

[39] A. Pandey, V. D. Gupta, and H. Nöth, *Eur. J. Inorg. Chem.*, 2000, **6**, 1351 – 1357.

[40] T. J. Boyle, R. P. Tyner, T. M. Alam, B. L. Scott, J. W. Ziller, and B. G. Potter, *J. Am. Chem. Soc.*, 1999, **121**, 12104 – 12112.

[41] I. Mijatovic, G. Kickelbick, M. Puchberger, and U. Schubert, *New J. Chem.*, 2003, **27**, 3 – 5.

[42] V. W. Day, T. A. Eberspacher, Y. Chen, J. Hao, and W. G. Klemperer, *Inorg. Chim. Acta*, 1995, **229**, 391 – 405.

[43] R. Ghosh, M. Nethaji, and A. G. Samuelson, *Chem. Comm.*, 2003, **20**, 2556 – 2557.

[44] X. Lei, M. Shang, and T. P. Fehlner, *Organometallics*, 1996, **15**, 3779 – 3781.

[45] N. Steunou, F. Robert, K. Boubekeur, F. Ribot, and C. Sanchez, *Inorg. Chim. Act.*, 1998, **279**, 144 – 151.

[46] I. Gautier-Luneau, A. Mosset, and J. Galy, *Z. Kristallogr.*, 1987, **180**, 83 – 95.

[47] G. A. Seisenbaeva, E. Ilina, S. Hakansson, and V. G. Kessler, *J. Sol. Gel. Sci. Technol.*, 2010, **55**, 1 – 8.

[48] A. Rammal, F. Brisach, and M. Henry, *C. R. Chimie*, 2002, **5**, 59 – 66.

[49] P. Piszczek, A. Grodzicki, M. Richert, and A. Wojtczak, *Inorg. Chim. Act.*, 2004, **357**, 2769 – 2775.

[50] P. Piszczek, M. Richert, and A. Wojtczak, *Polyhedron*, 2008, **27**, 602 – 608.

[51] G. Kickelbick and U. Schubert, *Eur. J. Inorg. Chem.*, 1998, **2**, 159 – 161.

[52] J. B. Benedict, R. Freindorf, E. Trzop, J. Cogswell, and P. Coppens, *J. Am. Chem. Soc.*, 2010, **132**, 13669 – 13671.

[53] F. R. Kogler, M. Jupa, M. Puchberger, and U. Schubert, *J. Mater. Chem.*, 2004, **14**, 3113 – 3138.

[54] T. Frot, G. L. Cochet, C. Sassoye, M. Popall, C. Sanchez, and L. Rozes, *Eur. J. Inorg. Chem.*, 2010, **36**, 5650 – 5659.

[55] T. Frot, J. Marrot, C. Sanchez, L. Rozes, and C. Sassoye, *Z. Anorg. Allg. Chem.*, 2013, **12 – 13**, 2181 – 2185.

[56] C. Serre, F. Millange, S. Surble, and G. Ferey, *Angew. Chem. Int. Ed.*, 2004, **46**, 6286 – 6289.

[57] S. Surble, C. Serre, C. Mellot-Draznieks, F. Millange, and G. Ferey, *Chem. Comm.*, 2006, **3**, 284 – 286.

[58] V. Guillerm, S. Gross, C. Serre, T. Devic, M. Bauer, and G. Ferey, *Chem. Comm.*, 2010, **46**, 767 – 769.

[59] B. Moraru, G. Kickelbick, M. Battistella, and U. Schubert, *J. Organomet. Chem*, 2001, **635**, 172 – 174.

[60] L. G. Hubert-Pfalzgraf, *J. Mater. Chem.*, 2004, **14**, 3113 – 3123.

[61] H. Bußkamp, G. B. Deacon, M. Hilder, P. C. Junk, U. H. Kynast, W. W. Lee, and D. R. Turner, *Crysta. Eng. Comm.*, 2007, **9**, 394 – 411.

[62] P. Walther, M. Puchberger, F. R. Kogler, K. H. Schwarz, and U. Schubert, *Phys. Chem. Chem. Phys.*, 2009, **11**, 3640 – 3647.

[63] G. Trimmel, S. Gross, G. Kickelbick, and U. Schubert, *Appl. Organometal. Chem.*, 2001, **15**, 401 – 406.

[64] S. Gross, *J. Mater. Chem.*, 2011, **21**, 15853 – 15861.

[65] U. Schubert, *Chem. Mater.*, 2001, **13**, 3487 – 3494.

[66] C. Sanchez, L. Rozes, F. Ribot, C. Laberty-Robert, D. Grosso, C. Sassoye, C. Boissiere, and L. Nicole, *C. R. Chimie*, 2010, **13**, 3 – 39.

[67] U. Schubert, *Chem. Soc. Rev.*, 2011, **40**, 575 – 582.

[68] M. Carraro and S. Gross, *Materials*, 2014, **7**, 3956 – 3989.

[69] F. Mammeri, E. Le Bourhis, L. Rozes, and C. Sanchez, *J. Mater. Chem.*, 2005, **15**, 3787 – 3797.

[70] J. Wen and G. L. Wilkes, *Chem. Mater.*, 1996, **8**, 1667 – 1681.

[71] L. Rozes and C. Sanchez, *Chem. Soc. Rev.*, 2011, **40**, 1006 – 1030.

[72] U. Schuebert, *J. Sol Gel Technol.*, 2004, **31**, 19 – 24.

[73] U. Schuebert, *Macromol. Symp.*, 2008, **267**, 1 – 8.

[74] F. Graziola, F. Girardi, M. Bauer, R. D. Maggio, M. Rovezzi, H. Bertagnolli, C. Sada, G. Rossetto, and S. Gross, *Polymer*, 2008, **49**, 4332 – 4343.

[75] F. R. Kogler, T. Koch, H. Peterlik, S. Seidler, and U. Schubert, *J. Polym. Sci. Part B: Polym. Phys.*, 2007, **45**, 2215 – 2231.

[76] Y. Gao, N. R. Choudhury, J. Matisons, U. Schubert, and B. Moraru, *Chem. Mater.*, 2002, **14**, 4552 – 4529.

[77] M. Sangermano, S. Gross, L. Pracella, A. Priola, and G. Rizza, *Macromol. Chem. Phys.*, 2007, **208**, 1730 – 1736.

[78] G. Trimmel, B. Moraru, S. Gross, V. D. Noto, and U. Schubert, *Macromol. Symp.*, 2001, **175**, 357 – 366.

[79] Y. Gao, F. R. Kogler, and U. Schubert, *J. Polym. Sci. Part A: Polym. Chem.*, 2005, **43**, 6586 – 6591.

[80] S. Puchegger, H. Rennhofer, F. R. Kogler, D. Loidl, S. Bernstoff, U. Schubert, and H. Peterlik, *Macromol. Rapid Commun.*, 2007, **28**, 2145 – 2150.

[81] T. Koch, F. R. Kogler, U. Schubert, and S. Seidler, *Chem. Month.*, 2007, **138**, 293 – 299.

[82] G. Dominguez-Espinoza, T. Halamus, P. Wojciechowski, M. Skurska, and M. Zaborski, *J. Noncryst. Solids*, 2009, **355**, 496 – 500.

[83] U. Schubert, Y. Gao, and F. R. Kogler, *Prog. Solid State Chem.*, 2007, **35**, 161 – 170.

[84] S. Gross, V. D. Noto, and U. Schubert, *J. Noncryst. Solids*, 2003, **322**, 154 – 159.

[85] S. Gross, G. Trimmel, U. Schubert, and V. D. Noto, *Polym. Adv. Technol.*, 2002, **13**, 254 – 259.

[86] F. Palacio, P. Oliete, U. Schubert, I. Mijatovic, N. Hüsing, and H. Peterlik, *J. Mater. Chem.*, 2004, **14**, 1873 − 1878.

[87] G. Trimmel, P. Fratzl, and U. Schubert, *Chem. Mater.*, 2000, **12**, 602 − 604.

[88] F. Girardi, F. Graziola, P. Aldighieri, L. Fedrizzi, S. Gross, and R. D. Maggio, *Prog. Org. Coat.*, 2008, **62**, 376 − 381.

[89] Y. Gao, F. R. Kogler, H. Peterlik, and U. Schubert, *J. Mater. Chem.*, 2006, **16**, 3268 − 3276.

[90] N. Miele-Pajot, L. G. Hubert-Pfalzgraf, R. Papiernik, J. Vaissermann, and R. Collier, *J. Mater. Chem.*, 1999, **9**, 3027 − 3033.

[91] R. D. Maggio, S. Dire, E. Callone, F. Girardi, and G. Kickelbick, *J. Sol-Gel Sci Technol.*, 2008, **48**, 168 − 171.

[92] L. Armelao, H. Bertagniolli, S. Gross, V. Krishnan, U. Lavrencic-Stangar, K. Müller, B. Orel, G. Srinivasan, E. Tondello, and A. Zattin, *J. Mater. Chem.*, 2005, **20**, 1954 − 1965.

[93] L. Armelao, S. Gross, K. Müller, G. Pace, E. Tondello, O. Tsetsgee, and A. Zattin, *Chem. Mater.*, 2006, **18**, 6019 − 6030.

[94] V. W. Day, T. A. Eberspacher, W. G. Klemperer, and C. W. Park, *J. Am. Chem. Soc.*, 1993, **115**, 8469 − 8470.

[95] Y. W. Chen, W. G. Klemperer, and C. W. Park, *Mater. Res. Soc. Symp. Proc.*, 1992, **271**, 57.

[96] H. E. Katz, M. L. Schilling, S. M. Stein, F. M. Houlihan, R. S. Hutton, and G. N. Tylor, *Chem. Mater.*, 1995, **7**, 1534 − 1538.

[97] S. Bocchini, G. Fornasieri, L. Rozes, S. Trabelsi, J. Galy, N. E. Zafeiropoulos, M. Stamm, J.-F. Gerard, and C. Sanchez, *Chem. Comm.*, 2005, **16**, 2600 − 2602.

[98] F. Ribot and C. Sanchez, *Comments Inorg. Chem.*, 1999, **20**, 327 − 371.

[99] G. J. A. A. Soler-Illia, E. Scolan, A. Louis, P.-A. Albouy, and C. Sanchez, *New J. Chem.*, 2001, **25**, 156 − 165.

[100] G. J. d. A. A. Soler-Illia, L. Rozes, M. K. Boggiano, C. Sanchez, C.-O. Turrin, A.-M. Caminade, and J.-P. Majoral, *Angew. Chem. Int. Ed.*, 2000, **39**, 4249 − 4254.

[101] M. Heinz, M. Puchberger, M. Bendova, S. O. Baumann, and U. Schubert, *Dalton Trans.*, 2010, **39**, 7640 − 7644.

[102] C. A. Ohlin, E. M. Villa, J. R. Rustad, and W. H. Casey, *Nat. Mater.*, 2010, **9**, 11 −19.

[103] J. Wang, J. R. Rustad, and W. H. Casey, *Inorg. Chem.*, 2007, **46**, 2962 −2964.

[104] V. Guillerm, F. Ragon, M. Hardi-Dan, T. Devic, M. Vishnuvarthan, B. Campo, A. Vimont, G. Clet, Q. Yang, G. Maurin, G. Ferey, A. Vittadini, S. Gross, and C. Serre, *Angew. Chem. Int. Ed.*, 2012, **51**, 9267 − 9271.

[105] R. Steudel and Y. Steudel, *J. Phys. Chem. A*, 2006, **110**, 8912 − 8924.

[106] X.-F. Sheng, G.-F. Zhao, and L.-L. Zhi, *J. Phys. Chem. C*, 2008, **112**, 17828 − 17834.

[107] P. Gonzalez-Navarrete, M. Calatayud, J. Andres, F. Ruiperez, and D. Roca-Sanjuan, *J. Phys. Chem. A*, 2013, **117**, 5354 − 5364.

[108] S. Li, J. M. Hennigan, and D. A. Dixon, *J. Phys. Chem. A*, 2009, **113**, 7861 − 7877.

[109] G. W. T. M. J. Frisch, H. B. Schlegl, G. E. Scuseria, M. A. Robb, J. R. Cheeseman, G. Scalmani, V. Barone, B. Mennuci, G. A. Petersson, H. Nakatsuji, M. Caricato, X. Li, H. P. Hratchian, A. F. Izmaylov, J. Bloino, G. Zheng, J. L. Sonnenberg, M. Hada, M. Ehara, K. Toyota, R. Fukuda, J. Hasegawa, M. Ishida, T. Nakajima, Y. Honda, O. Kitao, H. Nakai, T. Vreven, J. A. Montgomery, J. E. J. Peralta, F. Ogliaro, M. Bearpark, J. J. Heyd, E. Brothers, K. N. Kudin, V. N. Staroverov, R. Kobayashi, K. Normand, J. Raghavachari, A. Rendell, J. C. Burant, S. S. Iyengar, J. Tomasi, M. Cossi, N. Rega, J. M. Millam, M. Klene, J. E. Knox, J. B. Cross, V. Bakken, C. Adamo, J. Jaramillo, R. Gomperts, R. E. Stratmann, O. Yazyev, A. J. Austin, R. Cammi, C. Pomelli, J. W. Ochterski, R. L. Martin, K. Morokuma, V. G. Zakrzewski, G. A. Voth, P. Salvador, J. Dannenberg, S. Dapprich, A. D. Daniels, ö. Farkas, J. B. Foresman, J. V. Oritz, J. Cioslowski, and D. J. Fox, Gaussian 09 Revision A.02, 2009.

[110] V. A. Nasluzov and N. Rösch, *Chem. Phys.*, 1996, **210**, 413 − 425.

[111] O. D. Häberln, C.-S. Chung, M. Stener, and N. Rösch, *J. Chem. Phys.*, 1997, **106**, 5189 − 5201.

[112] C. M. Aikens, *J. Phys. Chem. A*, 2009, **113**, 10811 − 10817.

[113] P. Hohenberg and W. Kohn, *Phys. Rev.*, 1964, **136**, B864 − B871.

[114] W. Kohn and L. J. Sham, *Phys. Rev.*, 1965, **140**, A1133 − A1138.

[115] J. C. Slater, *The Self-Consistent Field for Molecular and Solids, Quantum Theory of Molecular Solids*, McGraw-Hill, New York, 4th ed., 1974.

[116] S. H. Vosko, L. Wilk, and M. Nusair, *Can. J. Phys.*, 1980, **58**, 1200 − 1211.

[117] N. C. Handy and A. J. Cohen, *Mol. Phys.*, 2001, **99**, 403 − 412.

[118] W.-M. Hoe, A. J. Cohen, and N. C. Handy, *Chem. Phys. Lett.*, 2001, **341**, 319 − 328.

[119] C. Lee, W. Yang, and R. G. Parr, *Phys. Rev. B*, 1988, **37**, 785 − 789.

[120] B. Miechlich, A. Savin, H. Stoll, and H. Preuss, *Chem. Phys. Lett.*, 1989, **157**, 200 − 206.

[121] J. P. Perdew, K. Burke, and M. Ernzerhof, *Phys. Rev. Lett.*, 1996, **77**, 3865 − 3868.

[122] J. P. Perdew, K. Burke, and M. Ernzerhof, *Phys. Rev. Lett.*, 1997, **78**, 1396.

[123] C. Adamo and V. Barone, *J. Chem. Phys.*, 1999, **110**, 6158 − 6170.

[124] C. Adamo and V. Barone, *J. Chem. Phys.*, 1998, **108**, 664 − 675.

[125] A. D. Becke, *J. Chem. Phys.*, 1993, **98**, 5648 − 5652.

[126] J. M. Tao, J. P. Perdew, V. N. Staroverov, and G. E. Scuseria, *Phys. Rev. Lett.*, 2003, **91**, 146401/1 − 146401/4.

[127] C. J. Cramer and D. G. Truhlar, *Phys. Chem. Chem. Phys.*, 2009, **11**, 10757 − 10816.

[128] T. Yanai, D. Tew, and N. Handy, *Chem. Phys. Lett.*, 2004, **393**, 51 − 57.

[129] P. J. Hay and W. R. Wadt, *J. Chem. Phys.*, 1985, **82**, 270 − 283.

[130] W. R. Wadt and P. J. Hay, *J. Chem. Phys.*, 1985, **82**, 284 − 298.

[131] P. J. Hay and W. R. Wadt, *J. Chem. Phys.*, 1985, **82**, 299 − 310.

[132] T. H. J. Duning and P. J. Hay, *Modern theoretical Chemistry*, Plenum, New York, 3rd ed., 1997.

[133] W. Weigend and R. Ahlrichs, *Phys. Chem. Chem. Phys.*, 2005, **7**, 3297 − 3305.

[134] D. Andrae, U. Häussermann, M. Dolg, and H. Stoll, *Theor. Chim. Acta*, 1990, **77**, 123 − 141.

[135] A. Bergner, M. Dolg, W. Kuechele, H. Stoll, and H. Preuss, *Mol. Phys.*, 1993, **80**, 1431 − 1441.

[136] M. Kaupp, P. v. R. Schleyer, H. Stoll, and H. Preuss, *J. Chem. Phys.*, 1991, **94**, 1360 – 1366.

[137] M. Dolg, H. Stoll, H. Preuss, and R. M. Pitzer, *J. Phys. Chem.*, 1993, **97**, 5852 – 5859.

[138] A. Schaefer, C. Huber, and R. Ahlrichs, *J. Chem. Phys.*, 1994, **100**, 5829 – 5835.

[139] L. E. Roy, P. J. Hay, and R. L. Martin, *J. Chem. Theory Comput.*, 2008, **4**, 1029 – 1031.

[140] S. F. Boys and F. Bernardi, *Mol. Phys.*, 1970, **19**, 553 – 566.

[141] S. Simon, M. Duran, and J. J. Dannenberg, *J. Chem. Phys.*, 1996, **105**, 11024 – 11031.

[142] V. V. Albert, S. A. Ivanov, S. Tretiak, and S. V. Kilina, *J. Phys. Chem. C*, 2011, **115**, 15793 – 15800.

[143] S. A. Ivanov, I. Arachchige, and C. M. Aikens, *J. Phys. Chem. A*, 2011, **115**, 8017 – 8031.

[144] P. Yang, S. Tretiak, A. E. Masunov, and S. Ivanov, *J. Chem. Phys.*, 2008, **129**, 1 –12.

[145] S. Tretiak, K. Igumenschev, and V. Chernyak, *Phys. Rev. B*, 2005, **71**, 33201/1 – 33201/4.

[146] J. D. Sokolow, E. Trzop, Y. Chen, J. Tang, L. J. Allen, R. H. Crabtree, J. B. Benedict, and P. Coppens, *J. Am. Chem. Soc.*, 2012, **134**, 11695 – 11700.

[147] G. Fornasieri, L. Rozes, S. Le Calve, B. Alonso, D. Massiot, M. N. Rager, M. Evain, K. Boubekeur, and C. Sanchez, *J. Am. Chem. Soc.*, 2005, **127**, 4869 – 4874.

[148] S. Trabelsi, A. Janke, R. Hässler, N. E. Zafeiropoulos, G. Fornasieri, S. Bocchini, L. Rozes, M. Stamm, J.-F. Gerard, and C. Sanchez, *Macromolecules*, 2005, **38**, 6068 – 6078.

[149] L. Rozes, G. Fornasieri, S. Trabelsi, C. Creton, N. E. Zafeiropoulos, M. Stamm, and C. Sanchez, *Prog. Solid State Chem.*, 2005, **33**, 127 – 135.

[150] F. Perineau, S. Pensec, C. Sanchez, C. Creton, L. Rozes, and L. Bouteiller, *Polym. Chem.*, 2011, **2**, 2785 – 2788.

[151] L. A. Kushch, V. D. Sasnovskaya, A. I. Dimitrev, E. B. Yagubskii, O. V. Koplak, L. V. Zorina, and D. W. Boukhvalov, *Dalton Trans.*, 2012, **41**, 13747 – 13754.

[152] A. Caragheorgheopol and V. Chechik, *Phys. Chem. Chem. Phys.*, 2008, **10**, 5029 – 5041.

[153] G. M. Sheldrick, Program for crystal structure determination, 1997.

[154] H. Zou, S. Wu, and J. Shen, *Chem. Rev.*, 2008, **108**, 3893 – 3957.

[155] S. H. Kim, S. H. Ahn, and T. Hirai, *Polymer*, 2003, **44**, 5625 − 5634.

[156] S. Jain, H. Goossens, M. v. Duin, and P. Lemstra, *Polymer*, 2005, **46**, 88055 − 8818.

[157] W. Z. Wang, G. Wang, P. Liu, and M. Qi, *Polym. Eng. Sci.*, 2012, **52**, 1047 − 1057.

[158] V. Ramesh, B. P. Panda, S. Mohanty, and S. K. Nayak, *Polym. Compos.*, 2012, **33**, 2177 − 2187.

[159] D. N. Bikiaris, G. Z. Papageorgiou, E. Pavlidou, N. Vouroutzis, P. Paletzoglou, and G. P. Karayannidis, *J. Appl. Polym. Sci.*, 2006, **100**, 2684 − 2696.

[160] X.-Y. Shang, Z.-K. Zhu, J. Yin, and X.-D. Ma, *Chem. Mater.*, 2002, **14**, 71 − 77.

[161] K. S. Huang, Y. H. Nien, J. S. Chen, T. R. Shieh, and J. W. Chen, *Polym. Comp.*, 2006, **27**, 195 − 200.

[162] M. Ö. . Bora, O. Coban, E. Avcu, S. Fidan, and T. Sinmazcelik, *Polym. Comp.*, 2013, **34**, 1591 − 1599.

[163] M. Hashimoto, H. Takadama, M. Mizuno, and T. Kokubo, *J. Mater. Sci: Mater. Med.*, 2007, **18**, 661 − 668.

[164] M. Sajjad, B. Feichtenschlager, S. Pabisch, J. Svehla, T. Koch, S. Seidler, H. Peterlik, and G. Kickelbick, *Polym. Int.*, 2012, **61**, 274 − 285.

[165] Y.-L. Liu, C.-Y. Hsu, and K.-Y. Hsu, *Polymer*, 2005, **46**, 1851 − 1856.

[166] T. Kashiwagi, A. B. Morgan, J. M. Antonucci, M. R. VanLandingham, R. H. Harris, W. H. Awad, and J. R. Shields, *J. Appl. Polym. Sci.*, 2003, **89**, 2072 − 2078.

[167] Y. Sun, Z. Zhang, K.-S. Moon, and C. P. Wong, *J. Polym. Sci. B: Polym. Phys.*, 2004, **42**, 3849 − 3858.

[168] S. Kang, S. I. Hong, C. R. Choe, M. Park, S. Rim, and J. Kim, *Polymer*, 2001, **42**, 879 − 887.

[169] P. Y. Rosso, K. Friedrich, and S. Sprenger, *J. Appl. Polym. Sci.*, 2006, **100**, 1849 − 1855.

[170] Y. Sun, Z. Zhang, and C. P. Wong, *Polymer*, 2005, **46**, 2297 − 2305.

[171] Y.-L. Liu, C.-H. Hsu, W.-L. Wei, and R.-J. Jeng, *Polymer*, 2003, **44**, 5159 − 5167.

[172] T. C. Merkel, Z. He, I. Pinnau, B. D. Freeman, P. Meakin, and A. J. Hill, *Macromolecules*, 2003, **36**, 8406 − 8414.

[173] K. Ueberreiter and G. Kanig, *J. Phys. Chem.*, 1950, **18**, 399 – 406.

[174] T. G. Fox and S. Loshaek, *J. Polym. Sci.*, 1955, **15**, 371 – 390.

[175] L. E. Nielsen, *J. Macromol. Sci. Part C: Polym. Rev.*, 1969, **3**, 69 – 103.

[176] M. F. Drumm, C. W. H. Dodge, and L. E. Nielsen, *Ind. Eng. Chem.*, 1956, **48**, 76 – 81.

[177] M. E. D. Rosa, M. Mours, and H. H. Winter, *Polym. Gels Networks*, 1969, **5**, 69 – 94.

[178] H. H. Winter, *Polym. Eng. Sci.*, 1987, **27**, 1698 – 1702.

[179] A. Basch, S. Gross, N. R. Choudhury, and J. Matisons, *J. Sol. Gel. Sci. Techn.*, 2005, **33**, 39 – 45.

[180] U. Schubert, T. Völkel, and N. Moszner, *Chem. Mater.*, 2001, **13**, 3811 – 3812.

[181] S. A. Khan, I. M. Plitz, and R. A. Rantz, *Rheol. Acta*, 1992, **31**, 151 – 160.

[182] A. Botella, J. Duputy, A.-A. Roche, H. Sauterau, and V. Verney, *Macromol. Rap. Comm.*, 2004, **25**, 1155 – 1158.

[183] O. Okay and W. Opermann, *Macromolecules*, 2007, **40**, 3378 – 3387.

[184] E. Andrzejewska, A. Marcinkowska, and K. Wegner, *Polymer*, 2011, **56**, 63 – 66.

[185] D.-J. Cho, H.-T. Ju, and J.-W. Hong, *J. Polym. Sci. A: Polym. Chem.*, 2005, **43**, 658 – 670.

[186] D. J. Kinning and E. L. Thomas, *Macromolecules*, 1984, **17**, 1712 – 1718.

[187] G. Beaucage, *J. Appl. Cryst.*, 1995, **28**, 717 – 728.

[188] G. Trimmel, S. Gross, G. Kickelbick, and U. Schubert, *Appl. Organomet. Chem.*, 2001, **15**, 401 – 406.

[189] B. Moraru, N. Hüsing, G. Kickelbick, U. Schubert, P. Fratzl, and H. Peterlik, *Chem. Mater.*, 2004, **14**, 1873 – 1878.

[190] F. R. Kogler and U. Schubert, *Polymer*, 2007, **48**, 4990 – 4995.

[191] G. F. Levchik, K. Si, S. V. Levchik, G. Camino, and C. A. Wilkie, *Polym. Degr. Stab.*, 1999, **65**, 395 – 403.

[192] S. Pabisch, B. Feichtenschlager, G. Kickelbick, and H. Peterlik, *Chem. Phys. Lett.*, 2012, **521**, 91 – 97.

[193] X.-H. Qin, P. Gruber, M. Markovic, B. Plochberger, E. Klotzsch, J. Stampfl, A. Ovsianikov, and R. Liska, *Polym. Chem.*, 2014, **5**, 6523 – 6533.

[194] B. Cardineau, R. Del Re, H. Al-Mashat, M. Marnell, M. Vockenhuber, Y. Ekinci, C. Sarma, M. Neisser, D. A. Freedman, and R. L. Brainard, *Adv. Patt. Mater. Proc*, 2014, **9051**, 90511B – 90511B12.

[195] A. Ovsianikov, V. Mironov, J. Stampfl, and R. Liska, *Expert. Rev. Med. Dev.*, 2012, **9**, 613 – 633.

[196] R. Schnitty, M. Kadic, T. Bückmann, and M. Wegener, *Science*, 2014, **345**, 427 – 429.

[197] B. Harke, P. Bianchini, F. Brandi, and A. Diaspro, *Chem. Phys. Chem.*, 2012, **13**, 1429 – 1434.

[198] R. Wollhofen, J. Katzmann, C. Hrelescu, J. Jacak, and T. A. Klar, *Opt. Expr.*, 2013, **21**, 10831 – 10840.

[199] M. Kaupp, A. S. Quick, C. Rodriguez-Emmenegger, A. Welle, V. Trouillet, O. Pop-Georgievski, M. Wegener, and C. Barner-Kowollik, *Adv. Funct. Mater.*, 2014, **24**, 5649 – 5661.

[200] A. S. Quick, H. Rothfuss, A. Welle, B. Richter, J. Fischer, M. Wegener, and C. Barner-Kowollik, *Adv. Funct. Mater.*, 2014, **24**, 3571 – 3580.

[201] B. Richter, T. Pauloehrl, J. Kaschke, D. Fichtner, J. Fischer, A. M. Greiner, D. Wedlich, M. Wegener, G. Delaittre, C. Barner-Kowollik, and M. Bastmeyer, *Adv. Mater.*, 2013, **42**, 6117 – 6122.

[202] S. Selimovic, J. Oh, H. Bae, M. Dokmeci, and A. Khademhosseini, *Polymers*, 2012, **4**, 1554 – 1579.

[203] A. S. Quick, J. Fischer, B. Richter, T. Pauloehrl, V. Trouillet, M. Wegener, and C. Barner-Kowollik, *Macromol. Rapid Comm.*, 2013, **34**, 335 – 340.

[204] J. H. Park, T. Y. Lim, O. O. Park, J. K. Kim, J.-W. Yu, and Y. C. Kim, *Macromol. Rapid Comm.*, 2013, **34**, 335 – 340.

[205] F. de Loos, C. Reynhout, J. J. L. M. Cornelissen, A. E. Rowan, and R. J. M. Nolte, *Chem. Comm.*, 2005, **1**, 60 – 62.

[206] M. Wiesbauer, R. Wollhofen, B. Vasic, K. Schilcher, J. Jacak, and T. A. Klar, *Nano Lett.*, 2013, **13**, 5672 − 5678.

[207] Y. Jun, P. Nagpal, and D. J. Norris, *Adv. Mater.*, 2008, **20**, 606 − 608.

[208] J. H. Moon, J. S. Seo, Y. Xu, and S. Yang, *J. Mater. Chem.*, 2009, **19**, 4687 − 4691.

[209] J. Fischer, T. Ergin, and M. Wegener, *Opt. Expr.*, 2011, **36**, 2059 − 2061.

Appendix A

Appendix

Table A.1: MAE values (Å) for the bond lengths calculated at Def2SVP|D95V level.

Functional	Zr–μO	Zr–O_c	Zr–O_b
Xα	0.02	0.04	0.03
SVWN5	0.01	0.03	0.04
OLYP	0.05	0.07	0.03
PBE	0.04	0.05	0.02
TPSS	0.04	0.05	0.01
mPW1PW91	0.03	0.04	0.01
PBE0	0.03	0.03	0.01
B3LYP	0.04	0.05	0.01
CAM-B3LYP	0.03	0.03	0.01

Table A.2: MAE values (Å) for the bond lengths calculated at LANL2DZ|D95V level.

Functional	Zr–μO	Zr–O_c	Zr–O_b
Xα	0.02	0.04	0.02
SVWN5	0.01	0.03	0.03
OLYP	0.05	0.09	0.04
PBE	0.04	0.07	0.02
TPSS	0.04	0.06	0.02
mPW1PW91	0.03	0.05	0.01
PBE0	0.03	0.05	0.01
B3LYP	0.04	0.07	0.02
CAM-B3LYP	0.03	0.05	0.02

Table A.3: MAE values (Å) for the bond lengths calculated at SDD|D95V level.

Functional	Zr–μO	Zr–O_c	Zr–O_b
Xα	0.02	0.03	0.02
SVWN5	0.02	0.03	0.03
OLYP	0.06	0.09	0.04
PBE	0.05	0.07	0.02
TPSS	0.04	0.06	0.02
mPW1PW91	0.03	0.05	0.01
PBE0	0.03	0.05	0.01
B3LYP	0.05	0.07	0.02
CAM-B3LYP	0.03	0.05	0.01

Table A.4: MAE values (Å) for the bond lengths calculated at Def2TZVP|TZVP level.

Functional	Zr–μO	Zr–O$_c$	Zr–O$_b$
Xα	0.01	0.02	0.02
SVWN5	0.01	0.02	0.02
OLYP	0.03	0.04	0.04
PBE	0.02	0.03	0.02
TPSS	0.02	0.02	0.02
mPW1PW91	0.02	0.01	0.01
PBE0	0.01	0.02	0.01
B3LYP	0.02	0.02	0.02
CAM-B3LYP	0.02	0.02	0.01

Table A.5: MAE values (Å) for the bond lengths calculated at LANL2TZ|TZVP level.

Functional	Zr–μO	Zr–O$_c$	Zr–O$_b$
Xα	0.04	0.02	0.02
SVWN5	0.01	0.02	0.02
OLYP	0.04	0.06	0.06
PBE	0.03	0.04	0.05
TPSS	0.03	0.04	0.03
mPW1PW91	0.02	0.02	0.02
PBE0	0.01	0.02	0.02
B3LYP	0.03	0.04	0.04
CAM-B3LYP	0.02	0.02	0.02

Table A.6: MAE values (Å) for the bond lengths calculated at LANL2TZ|TZVP level.

Functional	Zr–μO	Zr–O_c	Zr–O_b
Xα	0.01	0.02	0.01
SVWN5	0.01	0.02	0.02
OLYP	0.04	0.05	0.05
PBE	0.03	0.04	0.04
TPSS	0.03	0.03	0.03
mPW1PW91	0.02	0.04	0.02
PBE0	0.01	0.04	0.02
B3LYP	0.03	0.04	0.04
CAM-B3LYP	0.02	0.04	0.02

Table A.7: RMS values (Å) for the bond lengths.

Functional	Def2SVP|D95V	Def2TZ|TZVP	LANL2DZ|D95V	LANL2TZ|TZVP	SDD|D95V	SDD|TZVP
Xα	0.04	0.02	0.03	0.03	0.03	0.01
SVWN5	0.04	0.03	0.04	0.02	0.03	0.02
OLYP	0.05	0.04	0.05	0.06	0.06	0.05
PBE	0.03	0.03	0.04	0.05	0.04	0.04
TPSS	0.03	0.02	0.04	0.03	0.04	0.04
mPW1PW91	0.03	0.01	0.03	0.02	0.03	0.03
PBE0	0.03	0.01	0.03	0.02	0.03	0.03
B3LYP	0.03	0.03	0.04	0.04	0.04	0.04
CAM-B3LYP	0.03	0.01	0.03	0.02	0.03	0.03

Table A.8: Experimental bond length (Å) for **Zr4**.

Bond	Bond length (Å)	Bond	Bond length (Å)
Zr(1)-O(1)	2.065	Zr(2)-O(7)	2.175
Zr(2)-O(1)	2.112	Zr(1)-O(8)	2.218
Zr(2')-O(1)	2.052	Zr(2)-O(9)	2.166
Zr(1)-O(2)	2.268	Zr(1)-O(10)	2.201
Zr(1)-O(3)	2.248	Zr(2')-O(11)	2.161
Zr(1)-O(4)	2.224	Zr(1)-(O12)	2.216
Zr(2)-O(5)	2.174	Zr(2')-O(13)	2.171
Zr(1)-O(6)	2.177		

Table A.9: MAE values (cm⁻¹) for the vibrational modes.

Functional	Def2TZVP|TZVP	LANL2TZ|TZVP	SDD|TZVP
Xα	27	25	24
SVWN5	41	35	34
OLYP	23	27	29
PBE	18	21	21
TPSS	26	26	27
mPW1PW91	84	70	74
PBE0	84	70	74
B3LYP	94	71	75
CAM-B3LYP	94	71	75

Table A.10: HOMO–LUMO splitting energies (eV).

Functional	Def2SVP|D95V	Def2TZVP|TZVP	LANL2DZ|D95V	LANL2TZ|TZVP	SDD|D95V	SDD|TZVP
Xα	3.28	3.06	3.02	3.25	3.02	3.25
SVWN5	3.25	3.06	2.99	3.21	2.99	3.22
OLYP	3.62	3.31	3.20	3.54	3.20	3.57
PBE	3.49	3.20	3.17	3.44	3.17	3.46
TPSS	3.69	3.34	3.33	3.66	3.33	3.66
mPW1PW91	5.66	5.42	5.31	5.57	5.31	5.58
PBE0	5.61	5.39	5.27	5.52	5.27	5.53
B3LYP	5.17	4.94	4.83	5.08	4.83	5.10
CAM-B3LYP	8.01	7.75	7.61	7.91	7.61	7.93

Table A.11: Ligand binding energies (BE) in dependence on the functionals and counterpoise (CP) corrected binding energies.

Functional	Def2TZVP|TZVP		LANL2TZ|TZVP		SDD|TZVP	
	BE [kcal/mol]	CP corr. [kcal/mol]	BE [kcal/mol]	CP corr. [kcal/mol]	BE [kcal/mol]	CP corr. [kcal/mol]
Xα	-164.96	-160.70	-164.19	-159.41	-164.41	-159.61
SVWN5	-168.70	-164.85	-167.97	-163.59	-168.07	-163.70
OLYP	-146.76	-141.88	-146.02	-140.60	-146.46	-140.58
PBE	-155.92	-151.52	-154.75	-150.32	-155.12	-150.52
TPSS	-155.35	-151.66	-154.56	-150.28	-154.77	-150.27
mPW1PW91	-161.06	-157.71	-160.40	-156.36	-160.63	-156.47
PBE0	-162.76	-159.44	-162.07	-158.07	-162.27	-158.17
B3LYP	-158.32	-154.92	-157.60	-153.61	-158.09	-153.89
CAM-B3LYP	-165.45	-161.94	-164.77	-160.61	-165.16	-160.81

Table A.12: Percentage of exchanged ligands depending on steric effects.

Zr4					ZrPiv			Ti4Zr4				
eq. IL [1]	HOAc	HOProp	HOIsob	HOPiv	HOAc	HOProp	HOIsob	eq. IL [1]	HOAc	HOProp	HOIsob	HOPiv
4	6	10	20	21	11	19	32	8	8	15	22	16
12	10	21	33	54	20	26	49	16	14	28	35	53
48	26	52	74	79	40	39	67	32	17	35	50	68
96	30	62	80	84	46	48	78	64	25	50	68	80
300	47	80	95	93	64	73	90	300	40	66	90	84
1000	70	80	95	97	80	79	95	1000	62	70	91	100

[1] eq. refers to equivalent incoming ligand (IL) with respect to the cluster concentration.

Table A.13: Ligand binding energies (BE) in dependence on the coordination site and type of ligand. Calculated on TPSS Def2TZVP|TZVP level.

Ligand	Position	coordination type	BE [kcal/mol]
Acetate	1	chelating	-165.67
Acetate	2	bridging	-168.11
Acetate	3	bridging	-163.28
Acetate	4	bridging	-160.62
Acetate	5	bridging	-175.37
Acetate	6	bridging	-161.48
Methacrylate	1	chelating	-155.35
Acetylacetonate	1	chelating	-177.06
CH_2FCOO^-	3	bridging	-152.21
CHF_2COO^-	3	bridging	-143.29
CF_3COO^-	3	bridging	-136.25
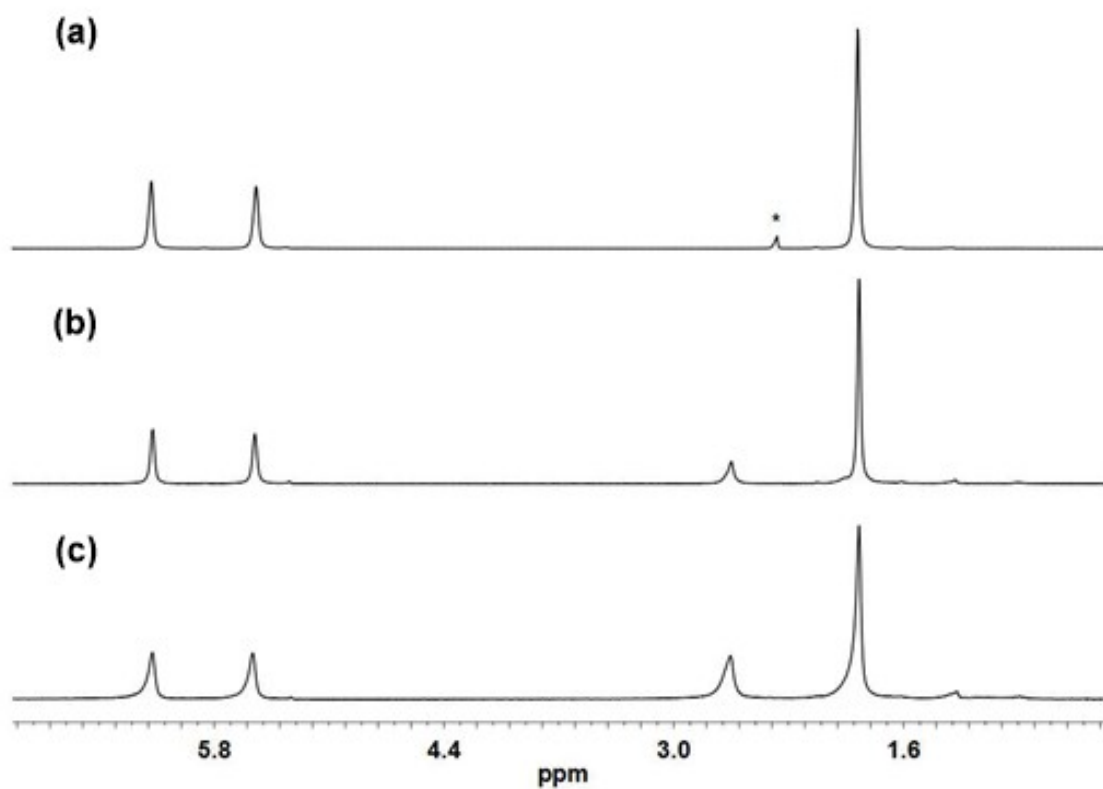
Figure A.1: ^{1}H NMR spectra (CD$_2$Cl$_2$, 250 MHz, 25 ℃)of **Zr4** (a), **Zr4_SH1** (b) and **Zr4 _SH2** (c). Residual toluene which stems from the washing process is marked with an asterix.
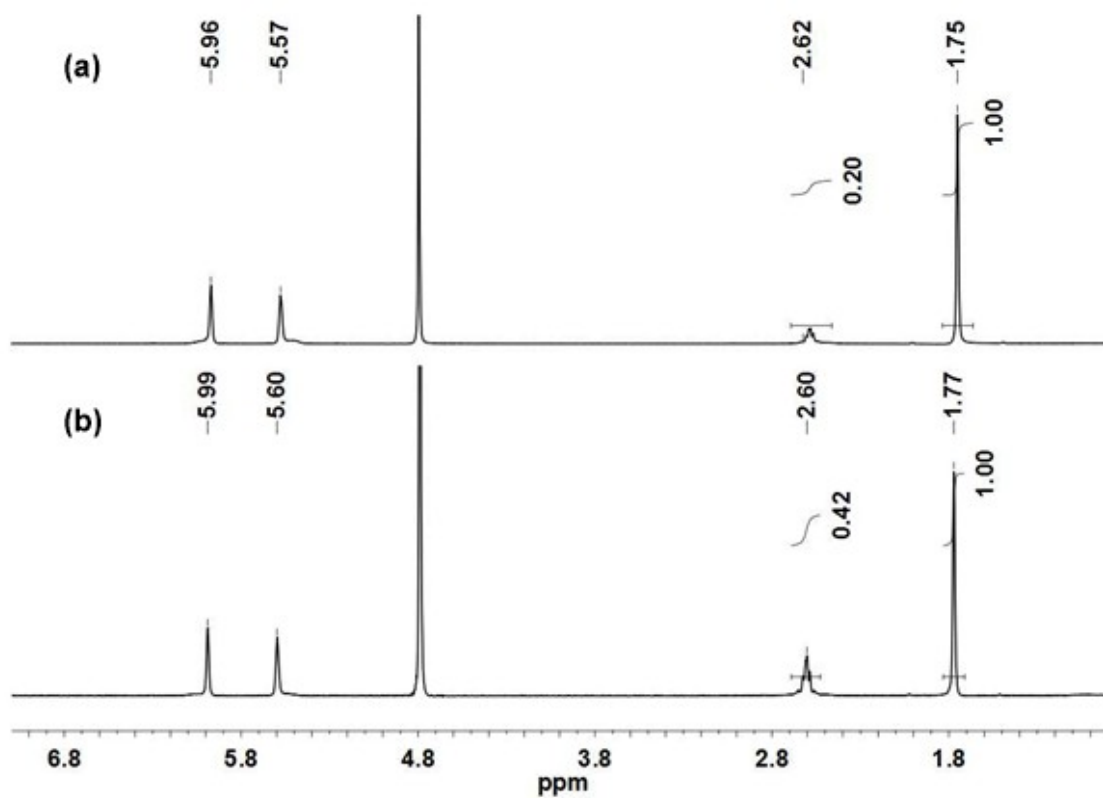
Figure A.2: ^{1}H NMR spectra (D$_2$O, 250 MHz, 25 ℃) of the destroyed cluster **Zr4_SH1** (a) and **Zr4_SH2** (b) in D$_2$O/DCl solution.
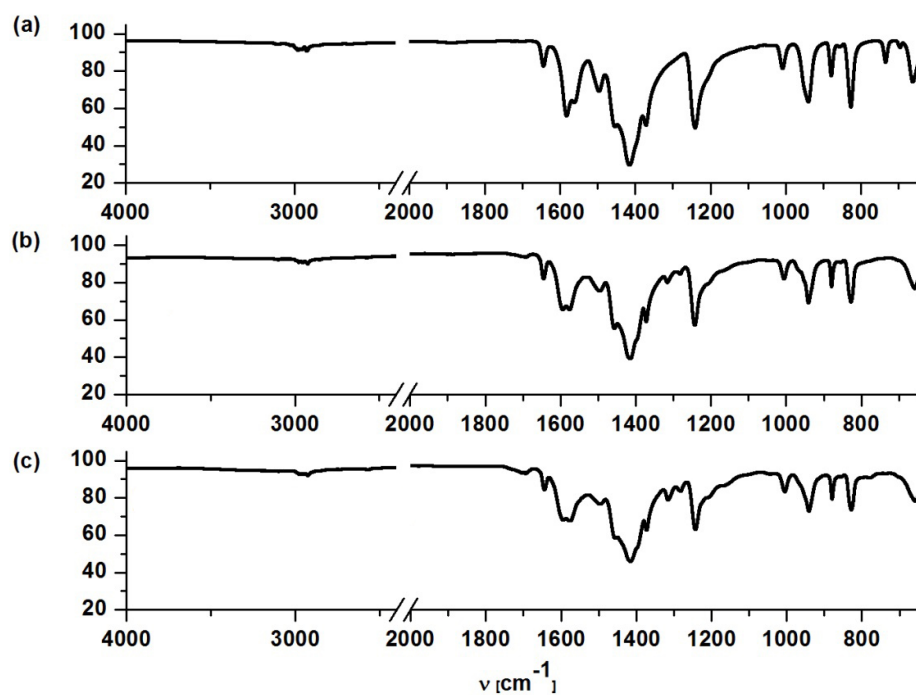
Figure A.3: MIR spectra of **Zr4** (a), **Zr4_SH1** (b) and **Zr4_SH2** (c).
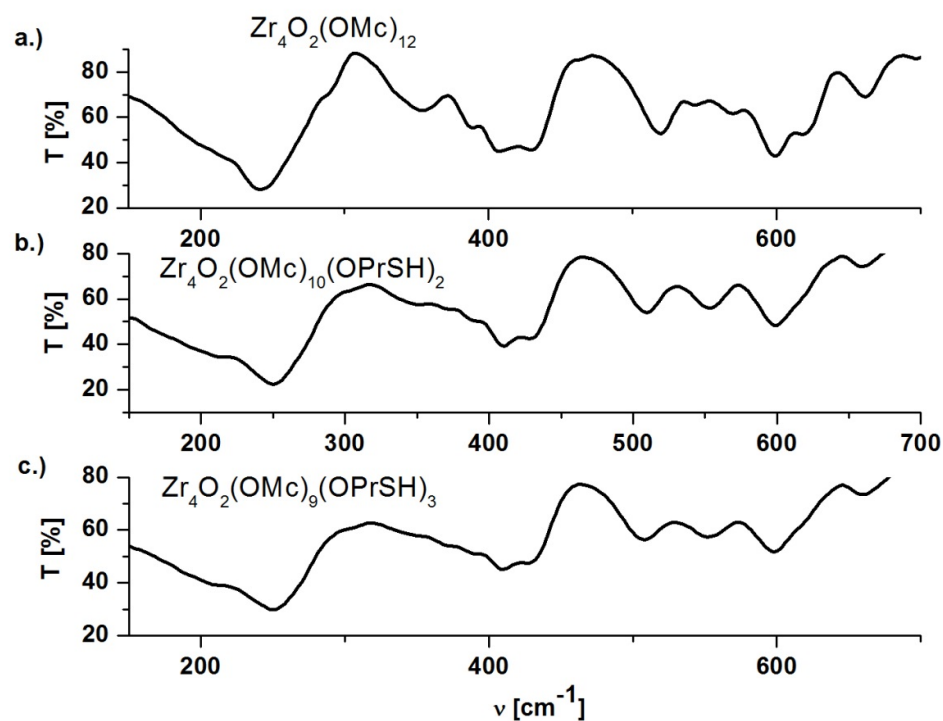
Figure A.4: FIR spectra of **Zr4** (a), **Zr4_SH1** (b) and **Zr4_SH2** (c).

List of Figures

List of Tables